FEEDBACK CONTROL OF FLOW SEPARATION USING SYNTHETIC JETS

A Dissertation

by

KIHWAN KIM

Submitted to the Office of Graduate Studies of
Texas A&M University
in partial fulfillment of the requirements for the degree of

DOCTOR OF PHILOSOPHY

December 2005

Major Subject: Mechanical Engineering

FEEDBACK CONTROL OF FLOW SEPARATION USING SYNTHETIC JETS

A Dissertation

by

KIHWAN KIM

Submitted to the Office of Graduate Studies of
Texas A&M University
in partial fulfillment of the requirements for the degree of

DOCTOR OF PHILOSOPHY

Approved by:

Chair of Committee,	Suhada Jayasuriya
Committee Members,	Ali Beskok
	Alexander Parlos
	Othon K. Rediniotis
Head of Department,	Dennis L. O'Neal

December 2005

Major Subject: Mechanical Engineering

ABSTRACT

Feedback Control of Flow Separation Using Synthetic Jets. (December 2005)

Kihwan Kim, B.S., Seoul National University;

M.S., Seoul National University

Chair of Advisory Committee: Dr. Suhada Jayasuriya

The primary goal of this research is to assess the effect of synthetic jets on flow separation and provide a feedback control strategy for flow separation using synthetic jets. The feedback control synthesis is conducted based upon CFD simulation for a rounded backward-facing step. The results of the synthetic jet experiments on an airfoil showed that synthetic jets have the potential for controlling the degree of flow separation beyond delaying the onset of flow separation. In the simulation, while the jet is ejected slightly upstream from the separation point, the feedback pressure signal is acquired at a downstream wall point where the vortex is fully developed. Due to the uniqueness of synthetic jets, i.e. “zero-net-mass flux”, the profile of synthetic jet velocity cannot be arbitrarily generated. The possible control variables are the magnitude or frequency of the oscillating jet velocity. Consequently, the fluidic system in simulation consists of the actuator model and the NARMAX (Nonlinear Auto Regressive Moving Average with eXogenous inputs) flow model. This system shows a strong nonlinear pressure response to the input jet frequency. Low-pass filtering of the pressure response, introduced for pressure recovery, facilitates a quasi-linear approximation of the system in the frequency domain using the describing function method. The low-pass filter effectively separates the pressure response into two frequency bands. The lower frequency band below the filter pass frequency includes the quasi-linear response targeted by the feedback control and the higher band above the filter stop frequency contains the attenuated higher harmonics, which are treated as nonlinear

disturbances. This quasi-linear approximation is utilized to design a PI controller for the fluidic system including the synthetic jet. To ensure one-to-one correspondence of the jet frequency and the filtered pressure response, the upper bound of the jet frequency is set at the frequency of the maximum pressure. The response of the resulting closed loop feedback control system, comprised of a PI controller, low-pass filter, SJA model and NARMAX model, is shown to track the desired pressure command with an improvement in the transient response over the open-loop system.

To my parents, Dongwook Kim and Sunja Shim

ACKNOWLEDGMENTS

There are many people that I must thank for their assistance with the investigations presented in this dissertation.

First of all, I would like to express the deepest appreciation to my advisor, Dr. Suhada Jayasuriya. He always provided me with invaluable guidance and insightful knowledge that led me to critical thinking to keep the research moving. As my mentor, his personal character with great spirit and enthusiasm is an example for the rest of my life.

I also would like to thank Dr. Ali Beskok and Dr. Othon Rediniotis for their insightful technical advice and warm-hearted relationship. Dr. Beskok deserves my sincere appreciation for his invaluable time spent in numerous discussions regarding the CFD simulation. Dr. Rediniotis provided me with the great support for the experimental work. I could not have completed the research without his valuable guidance on the experiments.

I am deeply indebted to Dr. Gyuhong Jeong, Dr. Lance Traub and Dr. Murray Kerr for all their directions. Whenever I had trouble with the research, I could overcome all the problems inspired by their experiences on fluid dynamics and control systems.

There are many friends and colleagues who have been extremely helpful. Thanks to all of them from the bottom of my heart.

I am extremely grateful for the love and support of my family. No words can express my deep appreciation to my parents for their love, encouragement and understanding during the many years I studied overseas.

TABLE OF CONTENTS

CHAPTER Page

CHAPTER Page

LIST OF TABLES

LIST OF FIGURES

FIGURE Page

FIGURE Page

FIGURE Page

FIGURE Page

FIGURE Page

CHAPTER I

INTRODUCTION

A. Basic Concepts and Applications of Synthetic Jets

Fluid flow significantly influences the performance of various systems such as transportation, industrial manufacturing, heating and cooling management. For example, ground vehicles consume 50% of their energy to overcome the aerodynamic drag force induced by air and both of aircraft and watercraft consume 90% of their energy to overcome the drag against air/water [1]. Flow control aims at improving the performance of a system involving fluid flow by means of inducing desirable changes to the flow. The common fluid-mechanical phenomena targeted by flow control are [2, 3]:

- Delaying or accelerating laminar-to-turbulence transition.
- Suppressing or enhancing turbulence.
- Preventing or causing flow separation.

Various benefits are expected from such flow manipulations: drag reduction, lift improvement, mixing enhancement and flow-induced noise attenuation [4].

The flow control methods are classified into two categories according to their energy expenditure. In active flow method, external energy is introduced into a fluidic system via actuators. In contrast, passive flow control does not utilize external power sources [4]. Recently, synthetic jets have attracted attention, since extensive numerical and experimental results have shown that they are a promising application among active flow control methods.

The journal model is *IEEE Transactions on Automatic Control.*

Typically, a **S**ynthetic **J**et **A**ctuator (SJA), a device to produce synthetic jets, consists of a closed cavity, an exit orifice on one side and an oscillating boundary on the other. The closed volume inside the actuator resonates with the oscillating boundary and thus the concentrated jets are ejected through the exit orifice. When the jets cross the orifice, viscous effects resulted in the vortical structures [5]. A series of vortices advancing to the external flow are referred to as “synthetic jets“.

The unique feature distinguishing synthetic jets from other methods is that synthetic jets are created from the periodic suction and blowing of a working fluid so that the energy can be transferred to the flow without adding extra mass. In that sense, synthetic jets are widely known as “zero-net-mass flux flow”. Therefore, a SJA can operate in a stand-alone manner without any extra piping or fluidic packages and thus can be simply fabricated and easily integrated into fluidic systems [6].

The parameters that characterize synthetic jets have been broadly investigated. First, two parameters are defined to identify the feature of the vortices created by the jets [7]. The first parameter is a dimensionless stroke length, $L_0/d = \frac{1}{d}\int_0^{\tau} u_0(t)dt$, where $u_0(t)$ is the velocity at the jet exit slot, τ is half of an oscillating period and d the characteristic length scale of an jet exit slot. The second is the Reynolds number based on the impulse, $\mathrm{Re}_{I_0} = I_0/\mu d \left(I_0 = \rho d \int_0^{\tau} u_0^2(t)dt\right)$, where ρ is fluid density and μ is viscosity.

Particularly, in case that synthetic jets are involved for flow separation control, the amplitude and frequency of the oscillating jets are regarded as key parameters. This is due to the fact that a basic mechanism of synthetic jets is the amplification of shear layer instability by periodic excitation. The reduced jet actuation frequency, F^+, is defined as

$$F^+ = \frac{f_j L}{U_\infty}, \tag{1.1}$$

where f_j is the actuation frequency (Hz), L the characteristic length of the separated region and U_∞ the free stream velocity. Physically, the inverse of this dimensionless property

stands for the ratio of one period of jet actuation to the time of flight of free stream over the controlled surface [8]. Previous research has established that $2 \sim 4$ vortices should stay constantly on the controlled surface for the effective separation control and that the jet frequency operating within the range of $0.5 \leq F^{+} \leq 1.5$ creates those number of vortices regardless of the Reynolds number [9]. Moreover, the jet amplitude is associated with a jet momentum coefficient

$$C_{\mu} = J/\frac{1}{2}\rho L U_{\infty}^{2}, \ \left(J = \frac{1}{\tau}\rho d \int_{0}^{\tau} u_{0}^{2}(t)dt \right), \tag{1.2}$$

which represents the momentum ratio between jets and free stream velocity [10]. This coefficient can be rewritten in terms of the jet amplitude, A, as follows.

$$C_{\mu} = \frac{(\rho dA)_{jet}}{(\rho L U)_{\infty}}. \tag{1.3}$$

The application of synthetic jets can be largely categorized as flow separation delay, aerodynamic performance enhancement, virtual aeroshaping, jet vectoring and mixing enhancement. The synthetic jets affect a boundary layer so that lift and drag on a cylinder are significantly modified [11]. Experiments on a symmetric airfoil model also verifies the control authority of synthetic jet actuators on the flow separation delay [10]. This work demonstrated that under Reynolds number of $3.1 \sim 7.25 \times 10^{5}$, the flow separates beyond 5° of **A**ngle **O**f **A**ttack (AOA), whereas it is completely attached up to 17.5° of AOA with the introduction of synthetic jets into a location slightly upstream from the separation point. Numerous simulations for synthetic jets have been conducted on a turbulent boundary layer, showing the numerical results are in good agreement with the experiments [12–15]. The virtual aeroshaping effect of synthetic jets has also drawn the attention of researchers. The virtual aeroshaping is achieved by a stationary recirculation bubble as a result of the interaction between the synthetic jets and the cross flow. This recirculation zone displaces the streamlines in the boundary layer enough to modify the surface pressure gradient and

the extent of separation [16, 17]. Furthermore, jet vectoring has emerges as an application to take advantage of synthetic jets. The parameters of synthetic jets, such as actuation frequency, location and velocity amplitude, have been examined to understand the mechanism of controlling a primary jet by adjacent synthetic jets [18, 19]. Recently, the application of synthetic jets has rapidly expanded. Synthetic jets have now been shown to be effective for the fuel-air mixing in a turbine engine combustor and the thermal management of electronic circuits [20–23].

B. Flow Separation Control Using Synthetic Jets

This research focuses on the ability of synthetic jets to delay flow synthetic jets and thus enhance aerodynamic performance. This is motivated by the promising potential of synthetic jets for controlling the extent of flow separation by varying jet frequency or magnitude.

To date, a large amount of research literature has been published on flow separation control for lifting surfaces using synthetic jets. Available research covers the dynamic stall problem as well as static stall. The various factors that characterize the performance of synthetic jets have been extensively examined [12, 24–30].

The mechanism by which synthetic jets suppress the separation of a wing can be explained as follows. Synthetic jets generate and promote vortex structures into a boundary layer. These vortices transfer the high momentum of free stream from the outer edge of the boundary layer to the inside of the boundary layer such that the reverse pressure gradient is overcome and the flow separation delayed in situations such as high AOA. The delay of flow separation leads to an increase in velocity and a decrease in pressure on the suction side. Consequently, the pressure difference between the top and bottom surfaces becomes larger and the lift force is improved [31].

Experiments on an airfoil using a reconfigurable synthetic jet actuator show that syn-

thetic jets not only delay stall by simply suppressing the flow separation but can also manipulate the degree of the separation by varying the actuation frequency [32, 33]. For these experiments, the control and data monitoring system was developed to manage the AOA and the synthetic jet frequency and to acquire the pressure distribution [34]. The system, however, did not contain a feedback loop to relate the output aerodynamics to the input command to SJA. Rather, the experiments were conducted in open-loop or with a man in the loop.

Implementation of a feedback loop is essential for flow separation control using synthetic jets. Supposing that a synthetic jet actuator is applied on an aircraft in flight, it should cope with large uncertainties connected with the flow around a wing. In addition, the available power to operate the actuator would be limited during flight. Therefore, robustness and efficiency of the controller are necessary to ensure acceptable performance of the actuator.

As alluded to earlier, the fundamental feature of synthetic jets, i.e. zero-net-mass flux, facilitates the fabrication and installation of the jet actuator while it causes considerable challenges from a control standpoint. As the actuator should maintain the periodic oscillation at all times, it cannot generate an arbitrary profile for jet velocity. Therefore, the controller has a limited degree of freedom for its output. The possible variables for control are the magnitude and frequency of the oscillating jet velocity.

Two kinds of control methods have been proposed to overcome these difficulties. The first approach suggested that the synthetic jet actuator should be operated at the frequency $F^+ \simeq 0(10)$ that are at least an order of magnitude higher than $F^+ \simeq 1$. In this range of the actuation frequency, the interaction of the jets with the cross flow is invariant on the global time scale of the flow and thus the changes of the aerodynamic forces become independent of the actuation frequency [6]. In contrast, the second approach is to maintain $F^+ \simeq 1$ constantly and control the jet momentum coefficient, C_μ. In this case, the mean value of the downstream pressure was suggested as a feedback input [35]. These two approaches

differ in terms of the operating frequency of the actuator. However, both of them share the common concept that the rate of change of the pressure or aerodynamic coefficients, which are the objectives of flow separation control, should be decoupled from the jet actuation frequency. Considering the efficiency of energy consumption, the latter approach would be preferable to the former, but more difficult in view of controller design due to the closeness of the frequency ranges for control and actuation.

The strategy of jet excitation at $F^+ \simeq 1$ was demonstrated via experiments on a hump model that simulated the upper surface of Glauert Glass II airfoil in a cryogenic pressurized wind tunnel at Mach number of 0.25 [36]. The pressure gradient, the difference between the upstream and downstream pressure with respect to the jet exit slot, was used to characterize the degree of flow reattachment and referred to as the pressure recovery parameter. For actuator dynamics, the RMS (root mean squares) cavity pressure fluctuation in the actuator, which is known to be directly related to the jet momentum coefficient, was coupled to the pressure command by second-order linear differential equations. The flow dynamics, representing the response of the pressure recovery parameter to the cavity pressure fluctuations, was also assumed to be a second-order linear system. The parameters of the differential equations were fitted from the experimental results of the steady state and open-loop step response. The jet oscillation operated constantly at 385 Hz. All the pressure data sampled at a rate of 100 Hz were averaged over a period of 0.5 seconds. The averaged signal was sent to the PC at a rate of 1 Hz.

The experimental results show that the actuator dynamics were much slower than the flow dynamics so that the changes in the magnitude of the oscillatory excitation were performed in a quasi-static state from the flow physics point of view. Consequently, the linear discrete controller using only an integral gain was sufficiently effective to track the desired pressure gradient and improve the transient response by minimizing the overshoot, since the resultant open-loop dynamics was dominated by the actuator dynamics and the effects

of the flow dynamics were negligible. Regarding the system performance, several issues remain to be addressed, being:

- If the actuator dynamics becomes faster to improve the overall system performance, the flow dynamics cannot be negligible any more and its nonlinear modeling is necessary.
- Averaging has such a large time constant that it affects the system performance negatively. Furthermore, it is not suitable to reject a noticeable magnitude of disturbances coming from the jet actuation frequency and higher harmonic frequency band.
- A certain type of synthetic jet actuator is incapable of varying the jet magnitude. For example, a piston-type SJA, which is implemented in this research, cannot adjust the stroke freely. In that case, the jet frequency should be controlled instead of the jet magnitude.

The lessons of this work serve as a useful starting point for our research.

C. Literature Review of Related Research

In this section, the previous work for modeling and feedback control of fluidic systems is reviewed and important knowledge is collected. In particular, research relevant to synthetic jets is highlighted.

For turbulent flow, feedback control of its fluctuation, particularly in a boundary layer, has been extensively investigated [4]. Feedback control schemes for turbulence can be categorized by examining the extent to which they are based on the governing flow equations as follows [37]: adaptive schemes, schemes based on physical arguments, schemes based on dynamical systems approach and optimal control schemes applied directly to the Navier-Stokes equations.

In this review, early research is classified according to the modeling methodology implemented for flow control. The importance of flow modeling has been highly emphasized for a long time, since it is fundamental to establish a successful closed-loop control methodology on fluidic systems. From a control standpoint, the model should be of sufficiently low order to be applicable in realistic control applications, while capturing the key dynamics of the original physical system. However, it is challenging to develop an efficient flow model to facilitate the synthesis of control algorithms that can guarantee the required performance. The difficulties in modeling are mainly due to the strong nonlinearity and infinite dimensionality of a fluid flow system.

First, analytical modeling regarding a synthetic jet actuator itself has been widely explored. Given a membrane type actuator, the elastic solution for the membrane and the compressible fluid model inside of the actuator were combined into a set of coupled nonlinear differential equations by Rathnasingham and Breuer [5]. Similarly, Lockerby and Carpenter proposed a jet model through the exit orifice using unsteady pipe-flow theory [38]. The approximate model was a partial differential equation which was solved by means of a finite difference scheme. As a different approach, a lumped element model of a piezoelectric-type actuator was presented by Q. Gallas et al [39]. The individual components of synthetic jets were modeled as elements of an equivalent electrical circuit. For a piston-type jet actuator, the dynamics for mechanical parts, i.e. crank shaft-connecting rod mechanism, was modeled in detail [40]. These studies contributed to improve insights into the dependence of synthetic jets on geometry and material of the device. However, these cannot account for the interaction of synthetic jets with external flow.

Research focusing on modeling and feedback control of external flow systems has assumed an oscillating velocity condition for synthetic jets. Mathematical models, such as ordinary differential equations, have been developed as relatively simple approaches [27, 36, 41, 42]. The model structures are assumed based upon physical knowledge about

aerodynamics and the model coefficients were estimated from numerical or experimental results. Based upon the developed models, corresponding feedback controllers were proposed. To delay dynamic stall, a controller was developed to determine the on-off switch of oscillatory blowing using a model based stall observer [41].Furthermore, a linear controller consisting of a bandpass filter and time delay was introduced to stabilize an oscillating cavity flow albeit valid only for limited conditions [42].

Recently, reduced order modeling using **P**roper **O**rthogonal **D**ecomposition (POD) has drawn attention, since the POD is known as an effective method to derive a low-dimensional models of various fluidic systems [43]. The experimental or numerical solutions of the physical system at prespecified time instances are called snapshots. After a singular value decomposition of the snapshots, the leading generalized eigenvectors are chosen as a POD basis. The Navier-Stokes equation can be projected onto this basis via Galerkin projection to derive a set of ordinary differential equations for the time-varying magnitude [44]. Based on POD, Rediniotis et al. [45] derived a reduced order Navier-Stokes model suitable for synthetic jet actuation. They also presented a stable state feedback control laws for the derived model. However, the realizability of the proposed control strategy remained as unresolved issues. Moreover, in order to control the resonance of subsonic cavity flow, the linear quadratic optimal state feedback controller and observer were synthesized based upon the linearized POD model and verified through CFD simulations [46].

As discussed so far, a general strategy for the modeling and control of fluid flow systems has remained elusive, since the effective control approaches are all different depending on the control objectives, flow conditions and geometries.

In this research, nonlinear modeling of the flow dynamics including the synthetic jets and its frequency domain analysis are inspired by Glass and Franchek [47, 48]. They performed the identification of a NARMAX model that captured the nonlinear dynamics relating the by-pass idle air valve and engine speed in an internal combustion engine. This

model was converted into a describing function representation to which a robust feedback controller design was applied. The NARMAX is an nonlinear extension of an ARMAX system identification method. It is capable of approximating a wide variety of nonlinear functions. For example, non-linear models such as Hammerstein, Wiener, bilinear and Volterra models can be interpreted as subclasses of NARMAX systems [49]. In particular, the parameters of the polynomial NARMAX are linear so that existing parameter estimation techniques such as least squares can be readily used [50]. Applications of NARMAX method rages over a wide area such as gas turbine, combustion engine, heat exchanger and dam health monitoring [51–54].

D. Objectives of the Research

The primary goal of this research is to assess the effect of synthetic jets on flow separation and provide a feedback control strategy of flow separation using synthetic jets. The research aims to achieve this goal by meeting the objectives given below:

- Investigate the effects of synthetic jets on flow separation using synthetic jet experiments on an airfoil and CFD-based synthetic jet simulations.
- Identify the dynamic model of a fluidic system with synthetic jets by applying system identification theory to CFD simulation results.
- Design a feedback control system to overcome the nonlinearity of a fluidic system and guarantee system performance requirements.

The modeling and control work in this research were performed using CFD simulation. A rounded backward facing step was chosen as a simulation domain and the flow was assumed to be two-dimensional, incompressible and laminar. The employed synthetic jets will oscillate slightly upstream from the flow separation point and the wall pressure on a

downstream point from the jet slot is to be used as a feedback signal. An averaged value of the feedback pressure represents the extent of flow separation on the slope. The controller aims to achieve the maximum pressure recovery by controlling the synthetic jet frequency with a constant jet magnitude.

E. Contributions of the Research

The contributions of this research are (i) determination of the properties of synthetic jets by experiments and simulations, (ii) nonlinear modeling of synthetic jet interaction with fluidic system and (iii) controller design for a fluidic system using synthetic jets. The contributions can be stated as follows:

- The synthetic jet experiments were performed under static and dynamic conditions. An integrated electronic system was developed for (i) controlling several motors in the experimental system and (ii) collecting real-time sensor data. From the experiments the maximum lift coefficient and stall angle were demonstrated to improve monotonically as the jet frequency increased. This suggests that synthetic jets have the potential to control the extent of flow separation by varying jet frequency.

- CFD simulations of synthetic jet actuation were conducted for a flat plate and a rounded backward-facing step respectively. Based upon the simulation results, a NARMAX model coupling the synthetic jet velocity and the pressure fluctuation was identified. In particular, given three different free stream velocities, the corresponding NARMAX models were identified for flat plate simulations. These models showed that the effects of varying free stream velocity can be accommodated into the model coefficients with an invariant model structure.

- A feedback control system for flow separation control was designed for the rounded

backward-facing step. A low-pass filter was proposed instead of averaging to estimate the pressure recovery. The low-pass filter separated the frequency components of the pressure output into two different frequency bands: the lower frequency band caused by the bias term of the synthetic jet frequency and the rate of change of the jet frequency, and the higher frequency band caused by the jet frequency. The lower frequency components showed a quasi-linear behavior that facilitated a linear control synthesis. The reduced higher frequency components could be treated as nonlinear disturbances.

- The response of the resulting closed loop feedback control system comprised of PI controller, low-pass filter, SJA model and NARMAX model was shown to track the desired pressure command with an improvement in the transient response over the open-loop system.

F. Organization of the Dissertation

This dissertation consist of three main parts: motivational experiments, CFD simulations for synthetic jet modeling and frequency response analysis and feedback control synthesis.

Immediately following this chapter, the results of the synthetic jet experiments on a NACA 0015 airfoil are presented. The hardware and software of the data monitoring and acquisition system for this experiment are explained. The experimental results are discussed with an emphasis on the relationship between synthetic jet frequency and aerodynamic coefficients.

In Chapter III, the NARMAX identification method is introduced. The procedures of parameter estimation and structure selection for the polynomial NARMAX are discussed. In the following chapters, this identification method is implemented to construct the nonlinear flow model that has the synthetic jet velocity as an input and the downstream pressure

as an output.

In Chapter IV, the results for CFD simulations of synthetic jet actuation on a flat plate are presented. The chapter consists of three parts: the boundary conditions for boundary layer simulation, the velocity condition for synthetic jet actuation and the NARMAX modeling of synthetic jets.

In Chapter V, synthetic jet actuation on a rounded backward-facing step is simulated. The chapter presents the effects of the synthetic jet frequency on flow separation in terms of mean pressure and shear stress distribution. Moreover, the effects of the free stream velocity on the characteristic plot, which relates the jet frequency to the mean pressure, are discussed.

In Chapter VI, given the CFD simulation for the rounded backward-facing step, a methodology to synthesize a feedback controller for flow separation is presented. The role of a low-pass filter in the feedback loop is thoroughly discussed using the describing function analysis. Consequently, a PI controller is simulated for the identified NARMAX model.

CHAPTER II

SYNTHETIC JET EXPERIMENTS

A. Overview

Synthetic jet experiments are performed under static and dynamic conditions. A piston-type synthetic jet actuator is embedded into a NACA 0015 airfoil and the pressure distribution around the airfoil is measured to calculate aerodynamic coefficients. The angle of attack can be controlled to keep constant or to oscillate periodically. To investigate the various parameters of synthetic jet actuation, an integrated electronic system is developed for (i) controlling the several motors in the experimental system and (ii) collecting real-time sensor data. The experimental results show that the maximum lift coefficient and stall angle improve monotonically as the jet frequency increases. It suggests that synthetic jets may have the authority to control the extent of flow separation by varying the jet frequency.

B. Nomenclature

c Chord length of an airfoil

C_P Pressure coefficient

C_L Lift coefficient

C_M Moment coefficient

f Synthetic jet frequency (Hz)

F^+ Reduced synthetic jet frequency

Re Reynolds number based upon the chord length

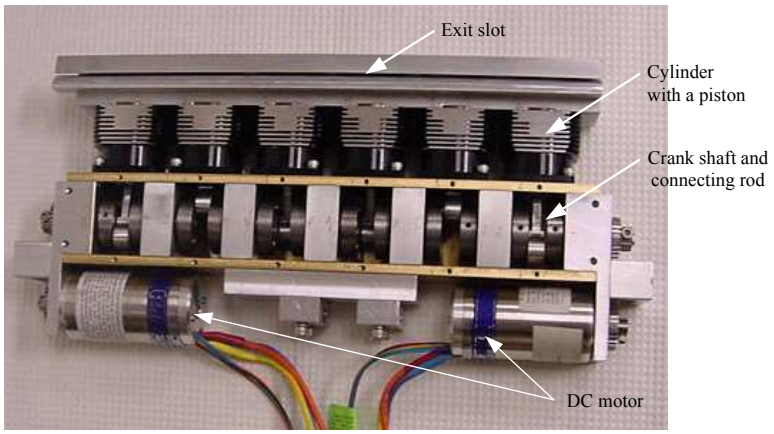

Fig. 1. Piston type synthetic jet actuator.

U_∞ Free stream velocity

α Angle of attack (AOA) (deg.)

ρ Density of air (kg/m^3)

C. Synthetic Jet Actuator

Figure 1 shows a recently developed synthetic jet actuator [32, 33]. 2 DC motors are connected to 6 pistons by a crank mechanism such that rotating motion of the motors can be converted into linear motion of the pistons, which create synthetic jets. In addition, the actuator is capable of varying the width of an exit slot from 0 to 1.22 mm using a stepper motor.

As shown in Fig. 2, this actuator is embedded in a NACA 0015 airfoil, which has a chord length of 420 mm and a span of 430 mm. On the surface of the airfoil model, 32 pressure taps are placed to capture pressure data via a pressure scanner as shown in Fig. 3. The pressure tap at the leading edge is numbered as the first pressure tap. The jets exit slot is located at 12.5 % of the chord between the fourth and fifth tap. Through the slot, the jet exits tangentially on the top surface of the wing to take advantage of the Coanda effect [9].

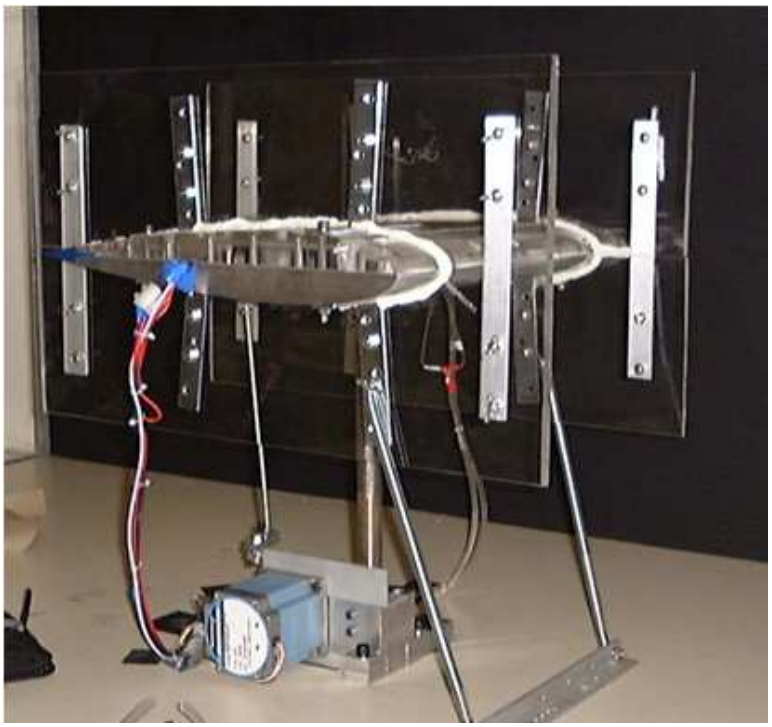

(a) NACA 0015 airfoil model embedding the synthetic jet actuator.

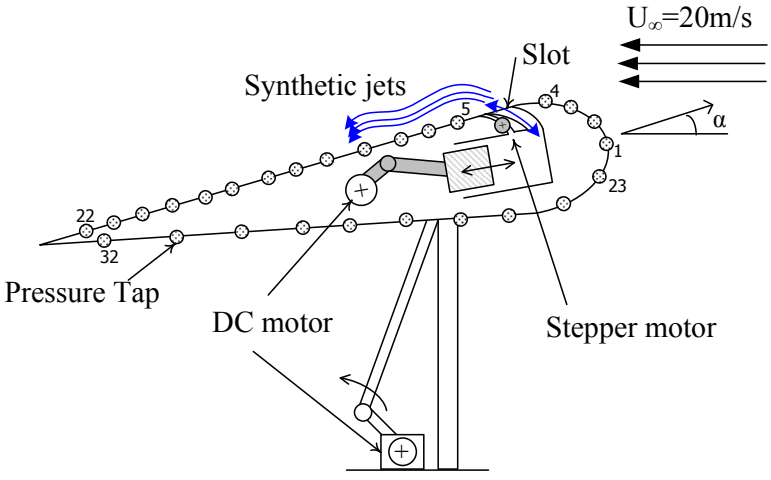

(b) Schematic diagram for the synthetic jet experiments.

Fig. 2. Airfoil model and schematic diagram for the experiments.

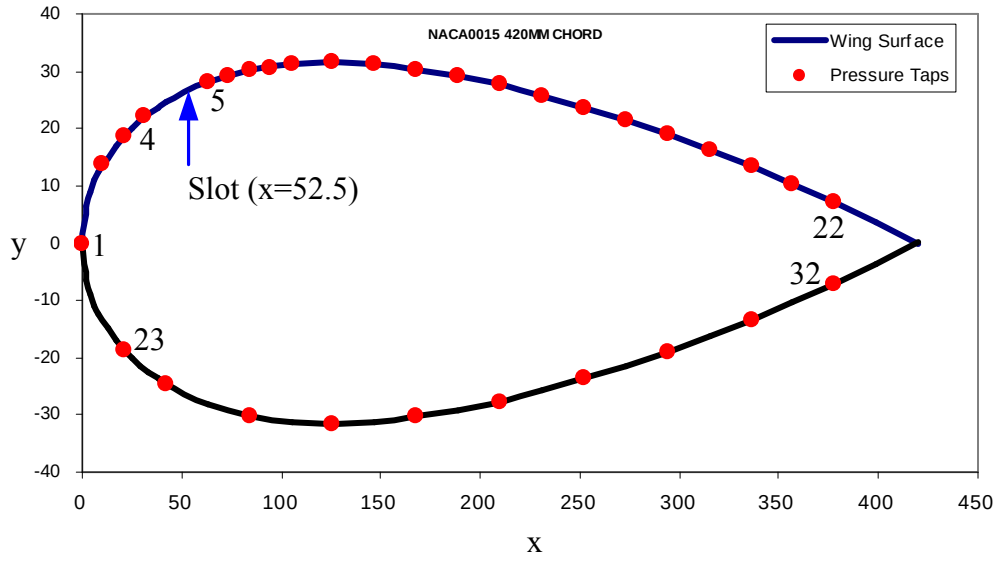

Fig. 3. Placement of the pressure taps on the NACA 0015 airfoil

This airfoil model is supported by a vertical strut and linkage arrangement which allow the angle of attack to be changed. The side plates are attached to both sides of the wing to ensure a quasi-two-dimensional behavior of the flow on the wing. The detailed structure and fabrication of the actuator can be found in the previous works [32, 33].

Experiments were conducted in a slow-speed wind tunnel under the free stream velocity 20 m/s, which corresponds to the Reynolds number 5.7×10^5 with respect to the chord length of the airfoil.

D. Monitoring and Data Acquisition System

A large number of parameters need to be changed freely to examine the effects of synthetic jet actuator on a flow field. First, the slot width and the driving motor speed in the actuator should be precisely controlled, since those are the important variables which represent the performance of the jets. Secondly, the system should be capable of either maintaining a certain angle of attack (AOA) or maneuvering it dynamically, since the experiments are to

be performed under static or dynamic conditions [34]. The objectives of the control and data acquisition system can be summarized as follows.

1. Control system function
    - SJA frequency control - DC motor speed control
    - Exit slot width control - stepper motor control
    - AOA control - DC motor angular position control
2. Data acquisition system function
    - Acquisition of pressure measurement data
    - ESP pressure scanner - 32 channel pressure transducer(sequential interface)
    - Acquisition of AOA control performance data

Therefore, in this research, an integrated electronic system was developed for (1) controlling several motors in the experimental system and (2) collecting real time sensor data. The entire control and data acquisition system is composed of an electronic hardware system and a Graphical User Interface (GUI) software with monitoring function. The hardware in Fig. 4 consists of two main micro-controller boards and peripheral circuits.

The main core of the system is a Digital Signal Processor (DSP), TMS320C31, which is responsible for AOA motor control, ESP data acquisition and TCP/IP communication with the user interface. In cooperation with the DSP, the 8-bit micro-controller, PIC16F877, manages the motor speed control for the SJA frequency and the stepper motor control for the slot width.

These two are connected via RS232C serial communication. As shown in Fig. 5, a GUI program is developed using JAVA programming language for data monitoring and logging, parameter input from a user. This is installed separately on a laptop computer

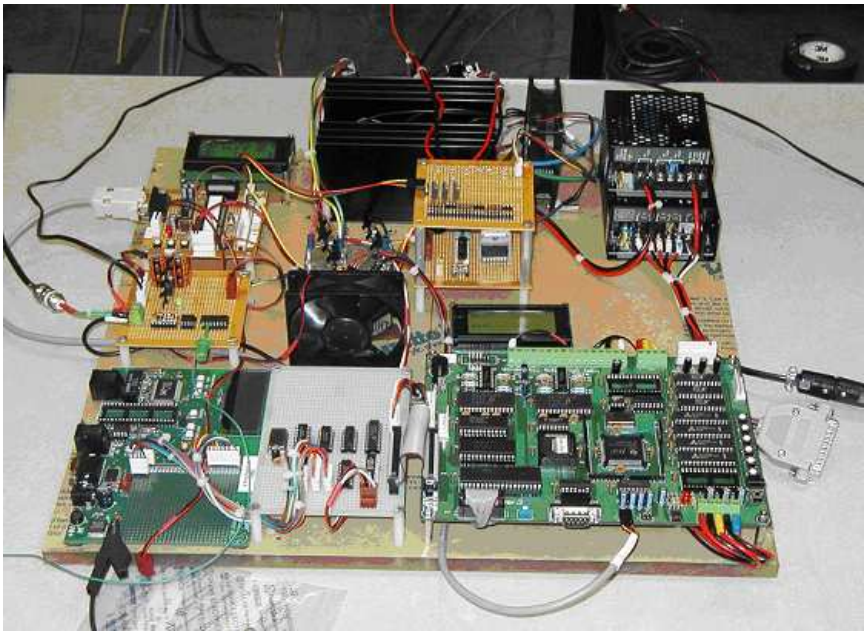

Fig. 4. Control and data acquisition hardware.

and TCP/IP protocol is implemented for data communication between the DSP and the software.

Figure 6 shows schematically the structure of the entire system setup.

1. Hardware for AOA Control

TMS320C31 32-bit DSP in Fig. 7 plays a key role in the system. It operates at 40 MHz clock speed and shows a performance of 50ns for floating point multiplication. This DSP board contains the peripheral interfaces such as 32 kword RAM, 8251 USART - RS232C, 8254 programmable interval timer, 8255 programmable peripheral interface, two AD7874 12-bit A/D converter (8 CH) and three AD7247 12 bit D/A converter (6 CH). The objective of TMS320C31 is to control the AOA by managing the DC motor-encoder assembly. A PI feedback algorithm is programmed for the position control of the AOA motor at 500 Hz frequency.

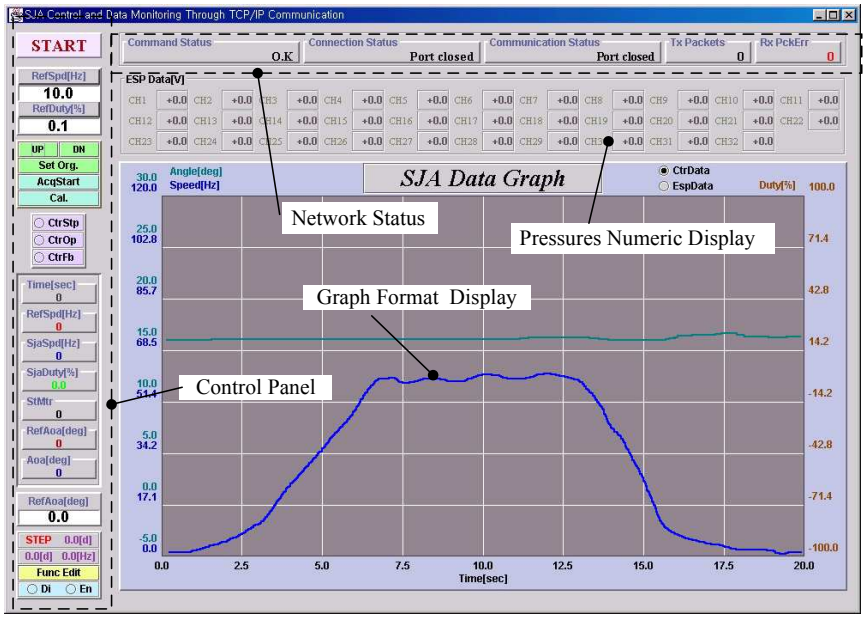

Fig. 5. GUI software.

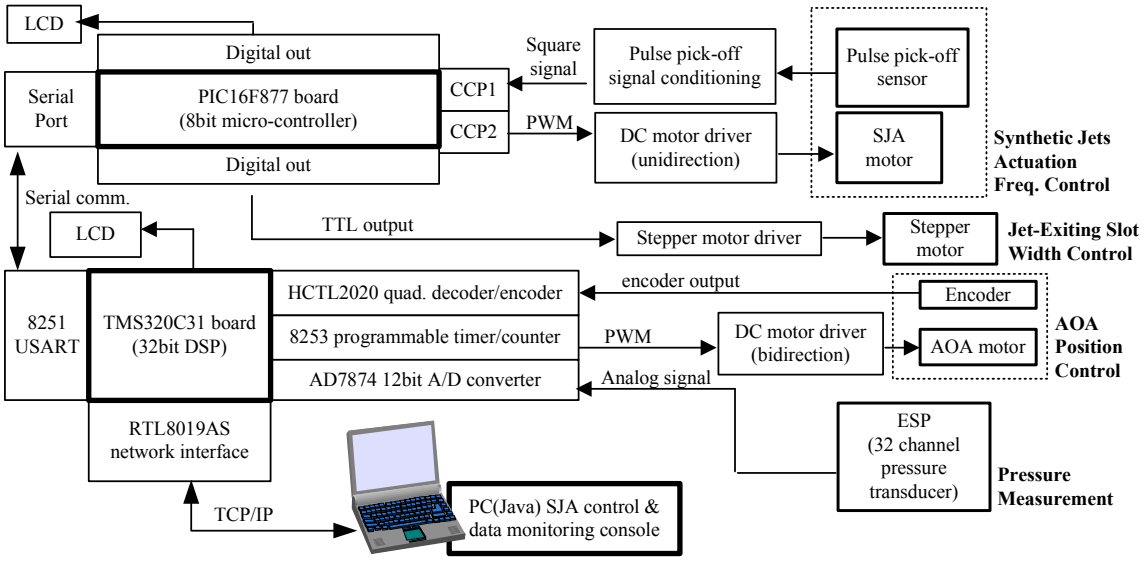

Fig. 6. Schematic diagram of a control and data acquisition system for the synthetic jet experiments.

Fig. 7. TMS320C31 DSP board.

The assembly of 9 0W geared DC motor with 42.871 : 1 gear reduction ratio and 500 PPR (Pulses Per Revolution) encoder was installed at the bottom end of the linkage structure in Fig. 8. The motor is driven by the 600 Hz PWM carrier frequency with 0.025 % duty resolution. The feedback revolution signal can be captured through the quadrature decoder counter, HCTL 2020 chip.

As the relationship between the encoder counts and AOA is nonlinear due to the characteristics of the linkage mechanism, the calibration is required before the experiments. The third order polynomial is implemented for this relationship as

$$\alpha = c_3 p^3 + c_2 p^2 + c_1 p, \tag{2.1}$$

where α is the angle of attack and p the encoder counts. The calibration result is shown in Fig. 9.

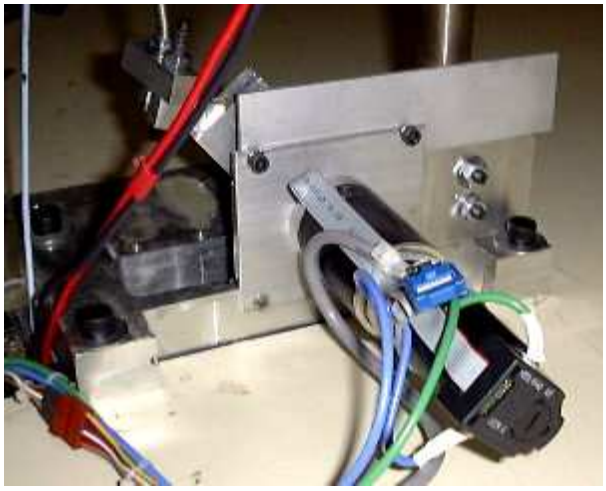

Fig. 8. DC Motor-linkage assembly for AOA control.

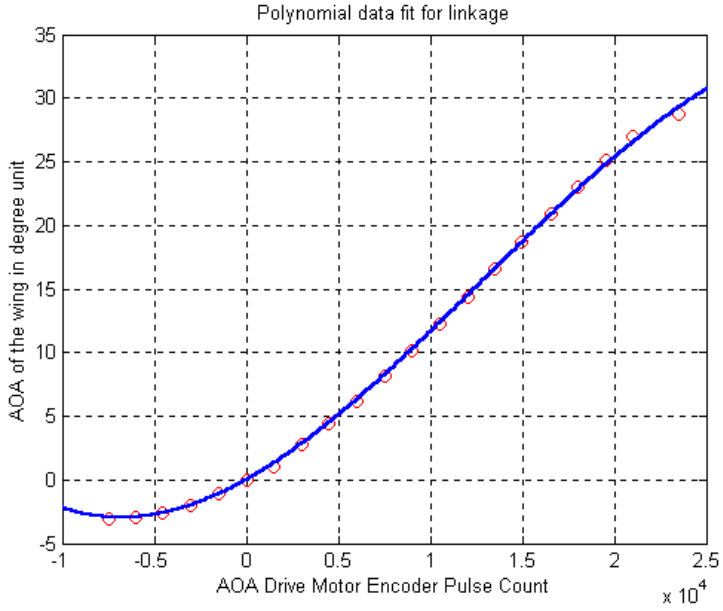

Fig. 9. Calibrated relationship of the linkage for AOA.

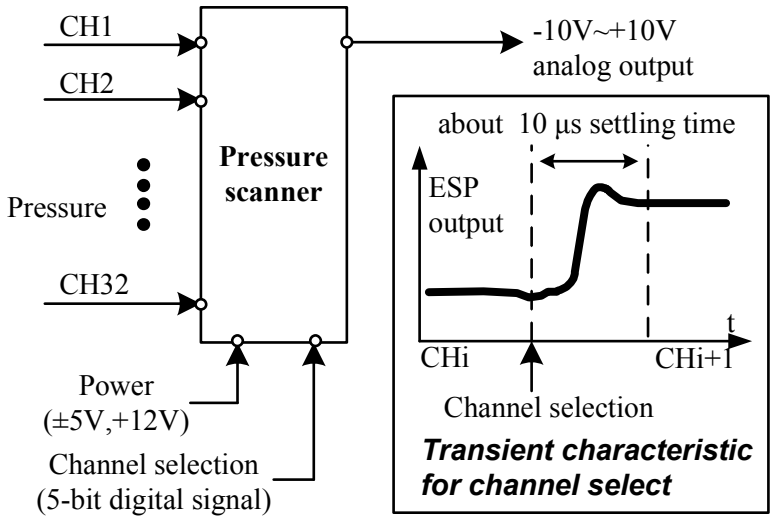

Fig. 10. Pressure data acquisition from the ESP scanner.

2. Hardware for Pressure Acquisition

The pressure data for the entire 32 channels are sampled every 10 ms. Figure 10 shows that the ESP pressure scanner activates the 32 pressure ports consecutively and collects the pressure data for each channel at every sampling time. It takes 1.76 ms to collect data from all channels, since the channel select signal applied from the main DSP has a transition characteristic of 20 μs delay before each 35 μs of A/D conversion.

3. Hardware for SJA Motor Control

As shown in Fig. 11, the PI feedback algorithm is implemented in PIC 16F877 micro-controller system for the velocity control of the SJA motor such that the jet actuation frequency can track the reference command precisely. The pulse signals, which are generated for every revolution of the motor, are conditioned via a low pass filter to be used as feedback signals. The minimum detectable motor speed is 10.6 Hz. The feedback control instructions are carried out every 10 ms, with 2 ms execution time.

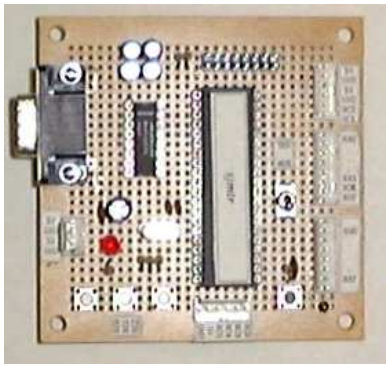

Fig. 11. SJA control system.

4. GUI software and Data Communication

The GUI software consists of two main functions: a system control interface and data logging as shown in Fig. 12. The control interface enables a user to command parameters related to SJA actuation frequency, angle of attack and slot width, and to carry out the calibration of the pressure sensors.

The user can monitor changes of parameters and data through a graphic-format and numeric-format display simultaneously. The monitored data by the DSP are refreshed on the display every 0.2 seconds.

Most of all, the key function of the software is to store the acquired pressure and AOA data transferred from the DSP. The data acquisition and logging is performed offline to prevent the time delay which might be caused by data communication, whereas the monitoring is executed online. The offline data logging scheme is as follows. Once a data acquisition command is issued from PC to DSP, the DSP acquires and stores 70 bytes of data in its RAM at 100 Hz sampling rate for 5 seconds such that the total size of the stored data leads to 35 kilobyte. 700 bytes in the stored data are transferred every 0. 2 seconds through TCP/IP such that it takes 10 seconds for the acquired data to be stored in a file by the GUI software. Figure 13 shows the contents and methods of data communication in

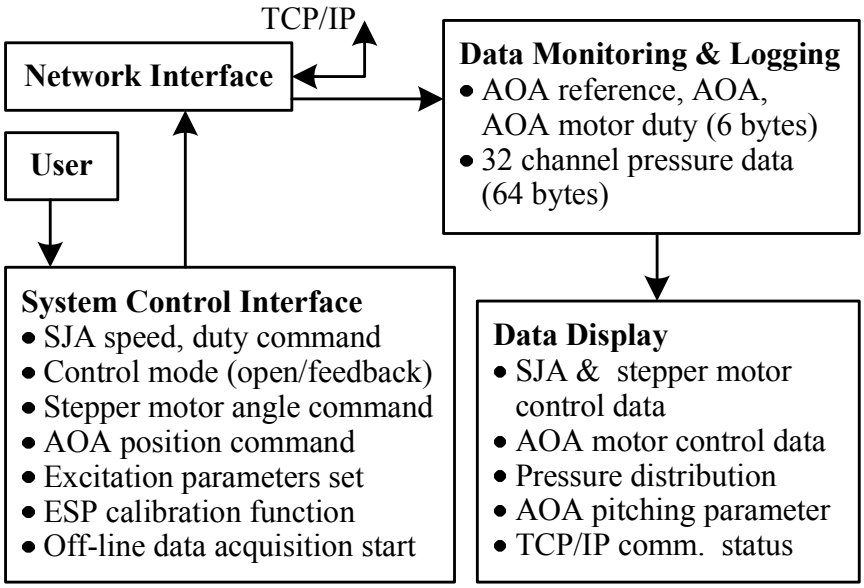

Fig. 12. Block diagram of the GUI software.

detail.

E. Results

Figure 14 shows the complete setup for the synthetic jet experiments. The NACA 0015 airfoil model with the synthetic jet actuator was placed within the slow-speed wind tunnel. The experiments were managed from the monitoring software installed in a laptop computer. One set data is acquired for 5 seconds with a 100 Hz sampling rate.

Two types of experiments were carried out. First the effects of synthetic jets were investigated under the static conditions. With the wing set at a certain AOA, the SJA frequency and the slot width were varied. The control parameters for the static experiments are as follows:

- AOA (°): 0, 1.5, 3, 5, 10, 15, 16.5, 18, 19.5, 21, 22.5, 24
- SJA frequency (Hz): 35, 45, 55, 65

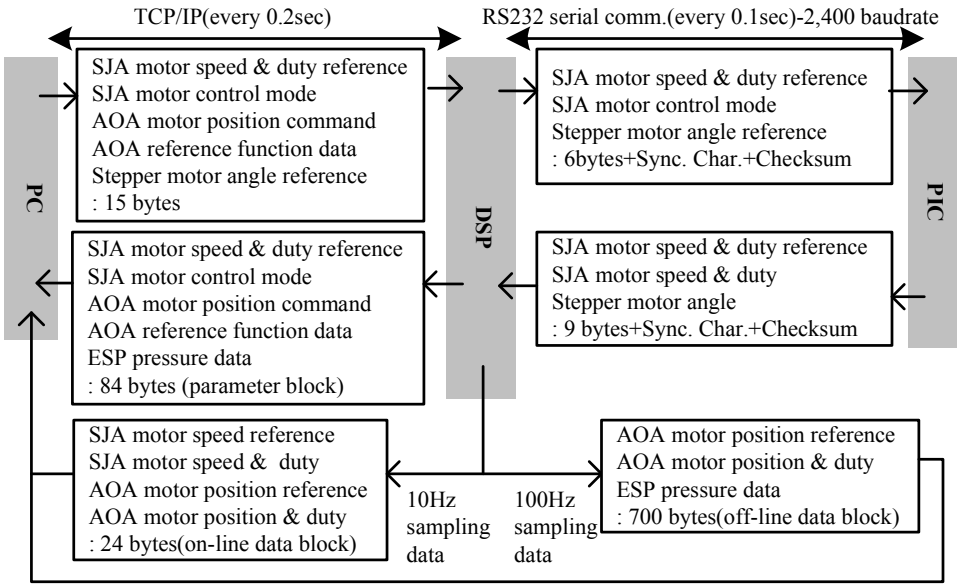

Fig. 13. Block diagram of data communication.

- Slot width (mm): 0.47, 0.72, 0.97, 1.22
- Dynamic Pressure (Pa): 260

Secondly, experiments were performed under dynamic wing pitching motion. The PI controller implemented in the DSP made the wing follow the AOA reference command such that the wing was driven in a range 0° to 25° for AOA, in a sinusoidal and triangular pitching motion. The AOA pitching motion frequencies were varied from 0.2 Hz to 2 Hz in increments of 0.2 Hz. The control parameters for the dynamic experiments are as follows:

- Range of pitching motion ($^\circ$): $0^\circ \sim 25^\circ$
- Frequencies of the pitching motion (Hz): 0.2, 0.4, 0.6, 0.8, 1.0, 1.2, 1.4, 1.6, 1.8, 2.0
- SJA frequency (Hz): 60
- Slot width (mm): 1.22
- Dynamic Pressure (Pa): 260 (corresponding to $U_\infty = 20.9 m/s$)

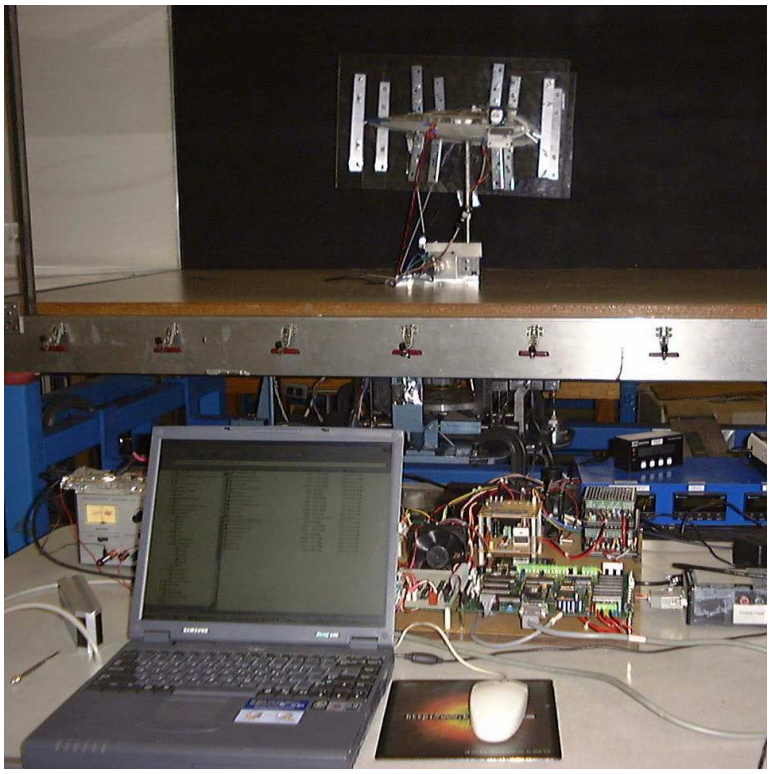

Fig. 14. Experimental setup in the wind tunnel dedicated to the synthetic jet experiments.

The reduced frequencies, F^+ in (1.1), corresponding to the jet frequencies used in the experiments were 0.61 (35 Hz), 0.80 (45 Hz), 0.97 (55 Hz), 1.15 (65 Hz). F^+ was computed with respect to the distance from the jet exit to the trailing edge or the flow-reattached point. All of them are within the range of $0.5 \leq F^+ \leq 1.5$ where the maximum efficiency of synthetic jet actuation is achieved.

The measured pressures around the wing was integrated to obtain sectional lift force and moment coefficients in (2.3) and (2.4), where the width of wing was disregarded due to the quasi-two-dimensional assumption about the airfoil model. The moment coefficient was calculated with respect to a quarter of the chord from the leading edge.

$$C_P = \frac{\text{Pressure}}{0.5\rho U_\infty^2}, \tag{2.2}$$

$$C_L = \frac{\text{Sectional Lift}}{0.5\rho U_\infty^2 c}, \tag{2.3}$$

$$C_M = \frac{\text{Sectional Moment}}{0.5\rho U_\infty^2 c^2}, \tag{2.4}$$

where C_P is a pressure coefficient, C_L a sectional lift coefficient and C_M a sectional moment coefficient. The c and U_∞ stands for the chord length and free stream velocity respectively.

1. Static Tests

Figure 15 shows examples of the acquired pressure data. These time-series data were collected at the fourth pressure tap from the leading edge on the upper part of the airfoil, varying SJA frequency and AOA. At $\alpha = 21^\circ$, the 65Hz synthetic jet actuation recovers the pressure and suppresses its fluctuation, compared with the case of no actuation. This plot verifies that the developed monitoring and data acquisition system can capture the effects of synthetic jets on flow separation effectively.

The captured pressure data for every pressure taps are averaged to yield the mean

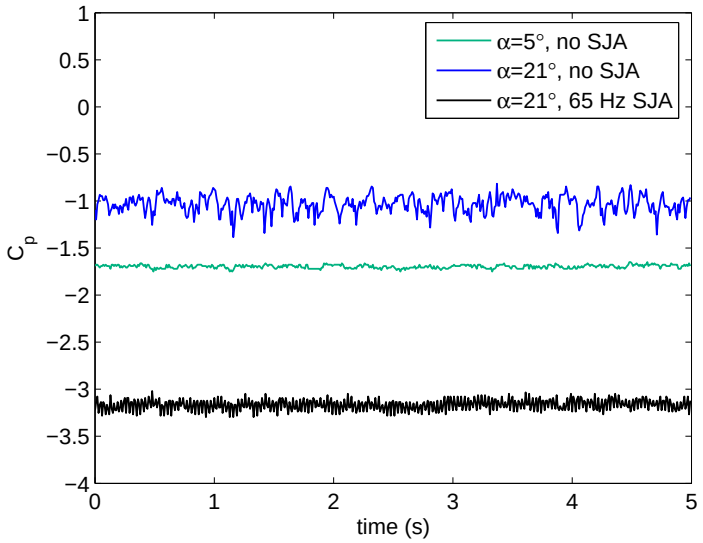

Fig. 15. Pressure coefficients acquired at the fourth pressure tap from the leading edge.

pressure distribution around the wing. Figure 16 shows the effects of the SJA frequency on the mean pressure distribution, with the angle of attack varied from 0° to 24°. As shown in Figs. 16(a)-(g), the synthetic jets have little effect on the pressure profile at low angles of attack, even though the SJA frequency increases. However, as the angle of attack increases higher shown in Figs. 16(h)-(l), the synthetic jets improve the reverse pressure gradient (or pressure recovery) on the upper surface. in the absence of jet actuation, the reverse pressure gradient on the upper surface begins to decrease from $\alpha = 18^\circ$ and it becomes nearly flat except small area close to the leading edge. The flatness of the overall pressure gradient indicates the flow separation on the airfoil. With actuation, the rapid pressure recovery occurs for $0 < x/c < 0.2$ and thereafter the pressure varies gradually towards the trailing edge. Consequently, the pressure difference between the upper and bottom surfaces increases and the resulting lift force on the wing is improved as well.

The plots in Figs. 16(i)-(l) present the effects of the SJA frequency. All the pressure profiles for the jet frequencies $f = 35 \sim 65$ Hz are similar at $\alpha = 19.5^\circ$. The reverse

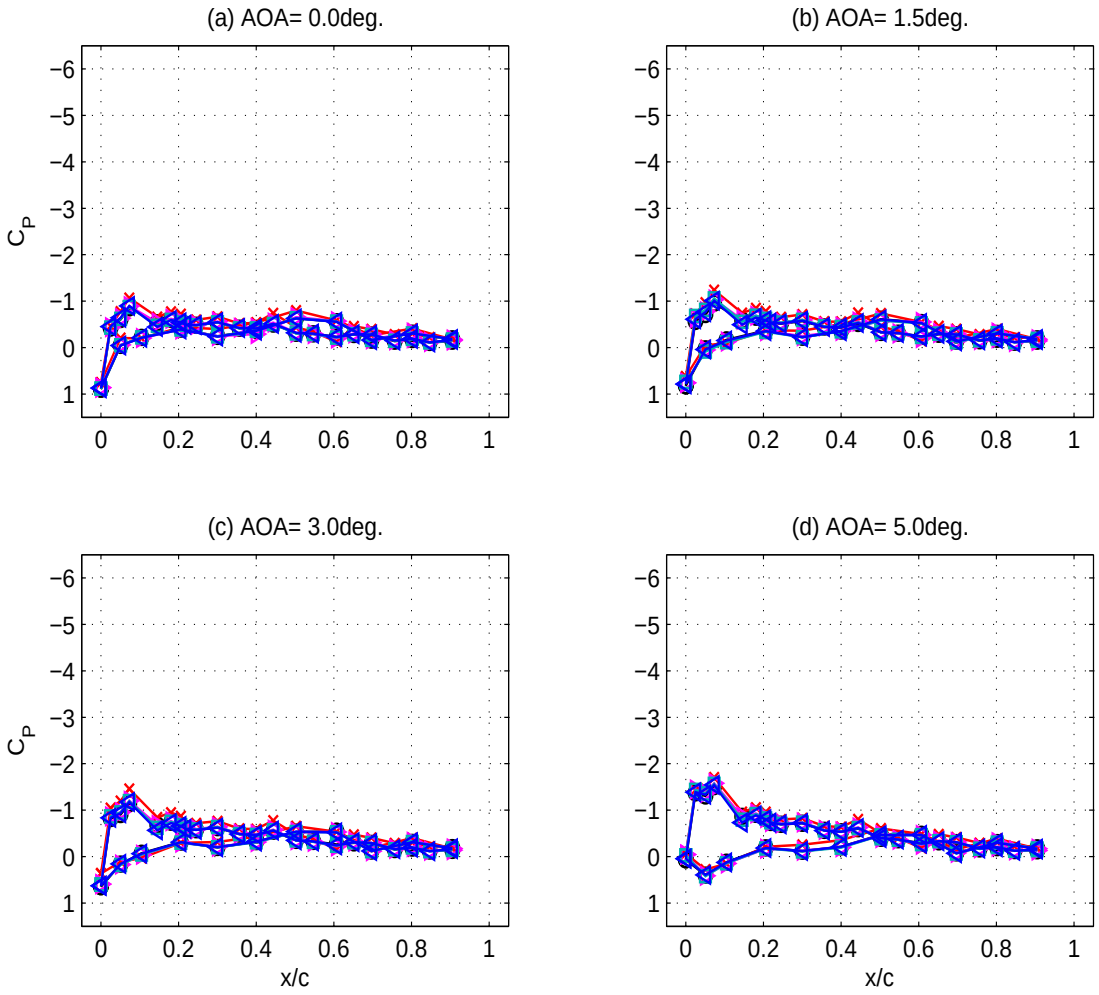

Fig. 16. Pressure coefficient distribution around the airfoil.

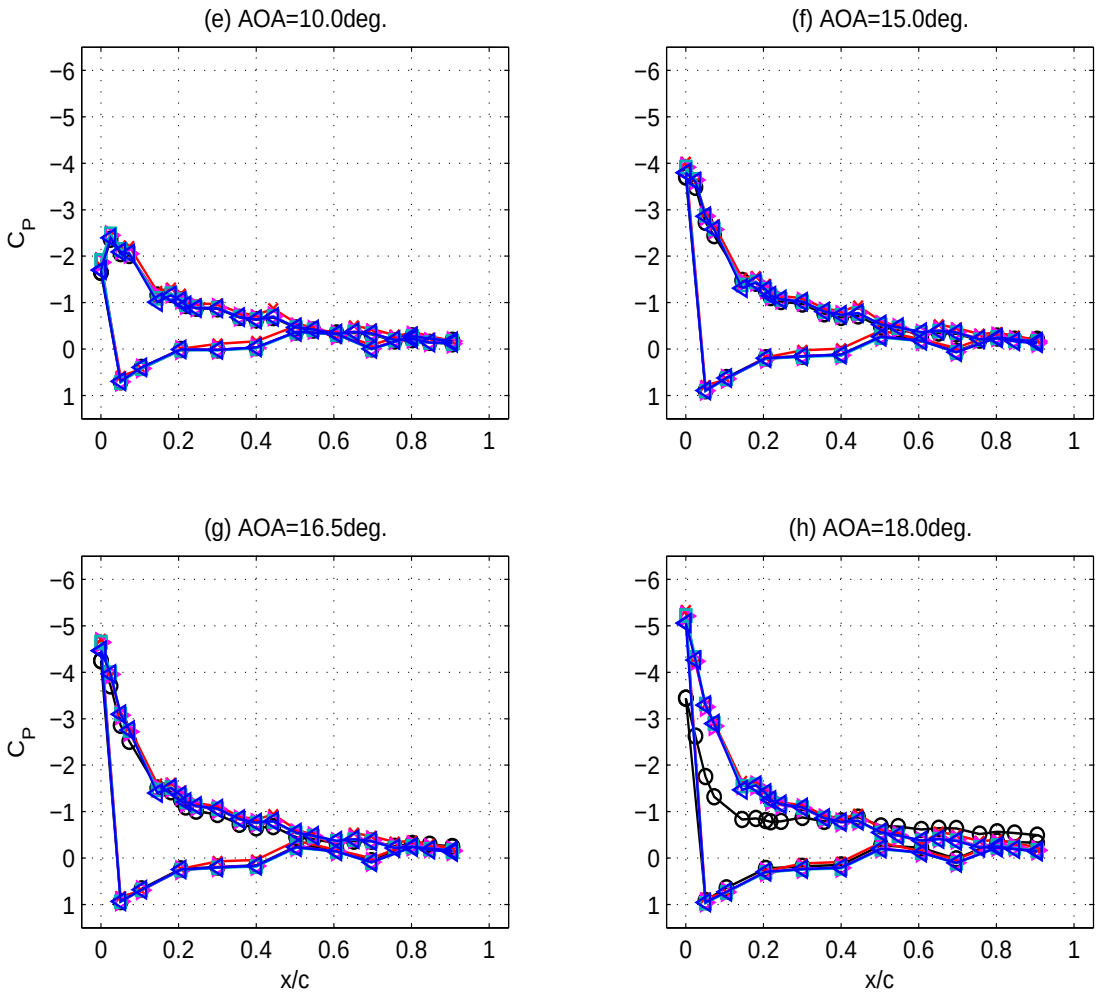

Fig. 16. Continued.

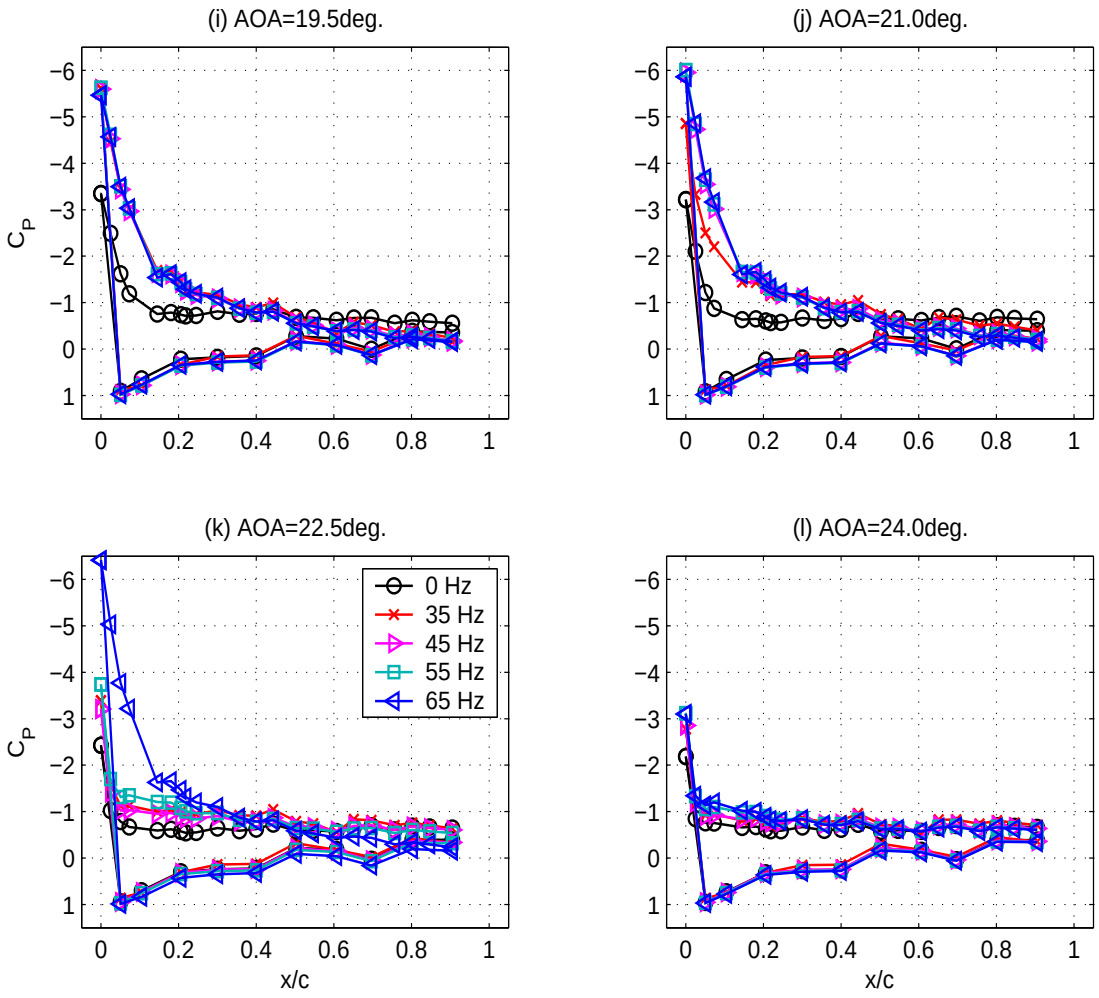

Fig. 16. Continued.

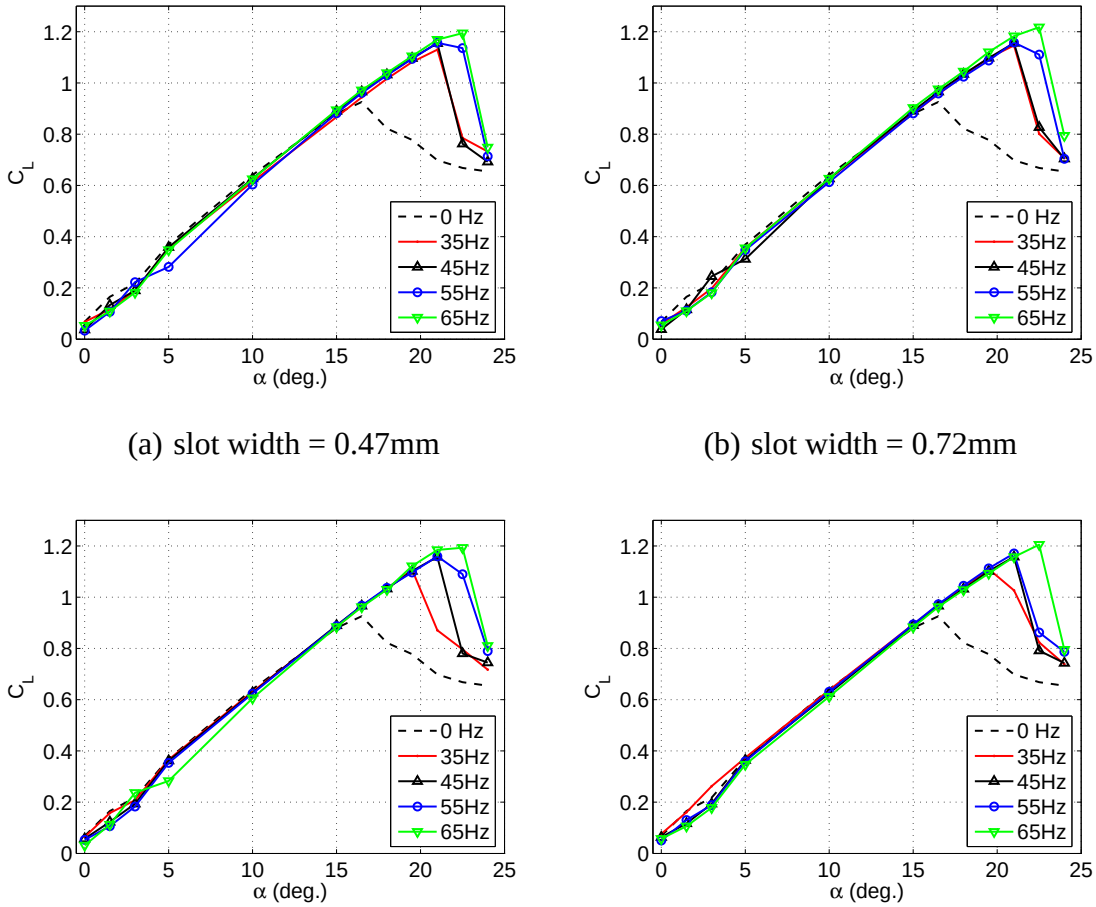

(a) slot width = 0.47mm

(b) slot width = 0.72mm

(c) slot width = 0.97mm

(d) slot width = 1.22mm

Fig. 17. Lift coefficients for varying angle of attack, slow width and synthetic jet frequency.

pressure gradient for $f = 35$ Hz begins to decrease at $\alpha = 21.0°$, while those for higher frequencies $f = 45 \sim 65Hz$ are maintained. However, at $\alpha = 22.5°$, only the 65Hz actuation is effective for the pressure recovery. Finally, the flow on the airfoil is completely separated at $\alpha = 24°$ regardless of the jet frequency. This relationship between the pressure and SJA frequency implies that the degree of flow separation can be controlled in terms of the pressure by controlling the synthetic jet frequency.

Figures 17 and 18 present the effects of synthetic jets on the lift and moment coefficients. Given the various jet frequencies and slot widths, the coefficients are examined

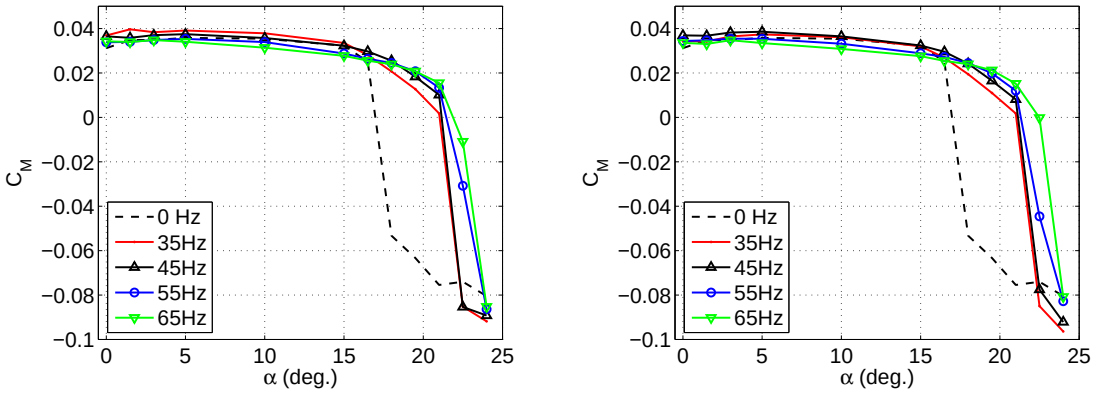

(a) slot width = 0.47mm

(b) slot width = 0.72mm

(c) slot width = 0.97mm

(d) slot width = 1.22mm

Fig. 18. Moment coefficients for varying angle of attack, slow width and synthetic jet frequency.

with respect to $\alpha = 0^\circ \sim 24.0^\circ$. The synthetic jets elevate the maximum lift coefficient and extend the stall angle effectively. For example, compared with the baseline case (no actuation), the 65 Hz actuation with 1.22 mm slot width improves the maximum lift by 25% and extend the stall angle by 6° as shown in Fig. 17(d). Moreover, the lift coefficient above the post-stall angle ($> 16^\circ$) can be controlled continuously by varying SJA frequency. Figure 18 also shows the ability of the SJA frequency to manipulate the pitching moment of the wing.

This control authority of synthetic jet on aerodynamic coefficients is in accordance with its effects on the pressure distribution as discussed earlier, since the coefficients are computed directly from the pressure distributions shown in Fig. 16. On the other hand, the results show the limitation. Synthetic jets are effective only in the post-stall angle region. It means that synthetic jets have little effect in case the flow is attached on the wing [32].

2. Dynamic Tests

Figure 19 presents the performance of the AOA controller and the captured pressure under 0.4 Hz sinusoidal pitching motion of the wing, as an example of the dynamic experiments. The results in the absence of jet actuation are shown in Fig. 19(a) and those with the jets shown in Fig. 19(b). The good match of the measured AOA to the command for a sinusoidal pitching motion in Fig. 19 verifies that the PI controller is successfully implemented for the AOA control. The severe disturbances and abrupt transition of the pressures in Fig. 19(a) indicate the flow separation for $t = 1.4 \sim 2.1$, $3.9 \sim 4.6$, where the AOA of the wing is approximately above $\alpha = 20^\circ$. In contrast, as shown in Fig. 19(b), the synthetic jet actuation affects the pressure response such that the duration and range of AOA of flow separation are reduced significantly compared with Fig. 19(a). Furthermore, the high frequency components are observed in the pressure data of the 5th$\sim$7th taps, which are located downstream of the exit slot, while the those data of fourth tap, which are upstream of the

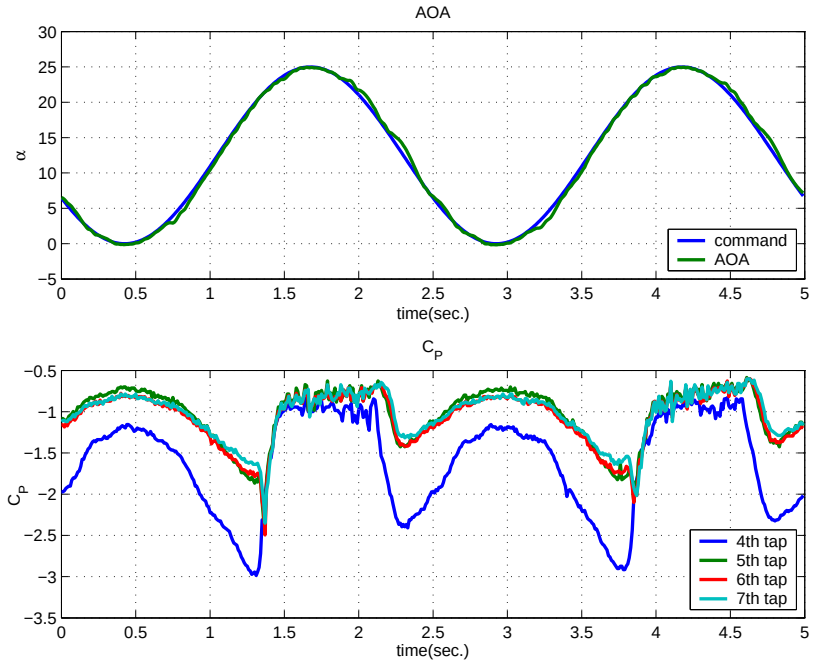

(a) No actuation.

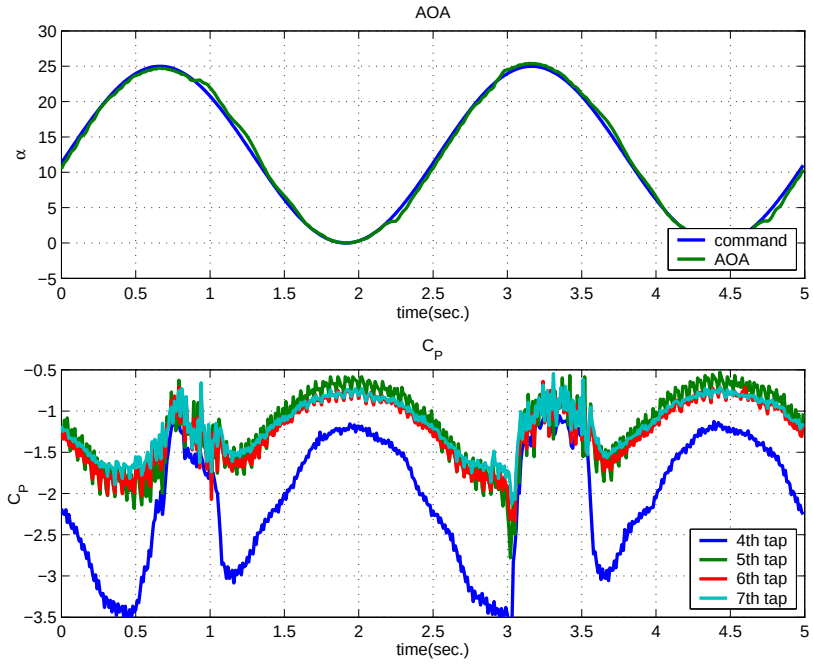

(b) 60 Hz synthetic jet actuation.

Fig. 19. Time-history data for the 0.4 Hz sinusoidal pitching motion.

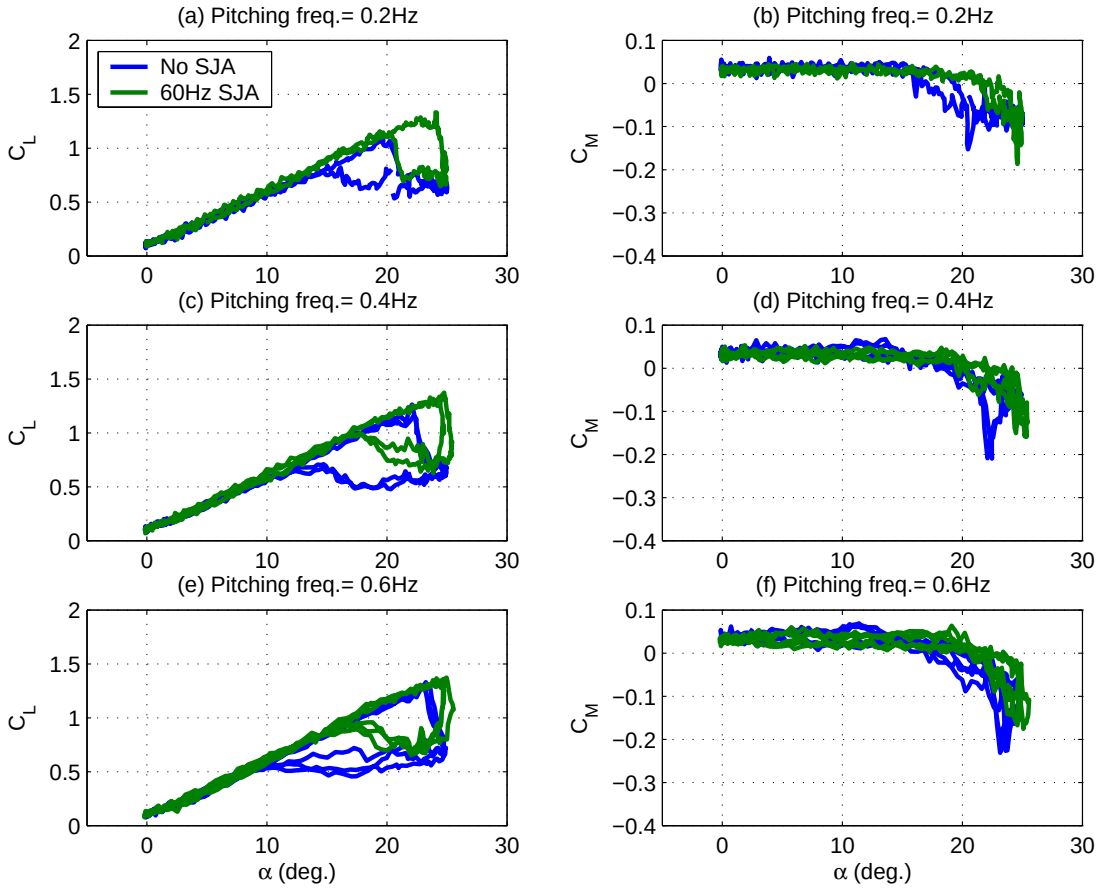

Fig. 20. Lift and moment coefficients for sinusoidal pitching motions of the wing.

slot, does not. These harmonic components are resulted from synthetic jets, since the jet frequency is much higher than the pitching frequency.

Figure 20 shows the lift and moment coefficients with various pitching frequencies. As alluded to earlier, the synthetic jets are activated at 60 Hz. Compared with the baseline condition (no actuation), the effects of synthetic jets on the lift coefficient C_L are twofold: the maximum value of C_L increases and the size of hysteresis is reduced. In particular, the hysteresis loop is eliminated at 2 Hz pitching frequency.

Below the 1 Hz pitching rate in Figs. 20(a)-(j), where a dynamic stall vortex does not occur, the baseline plots without SJA show that as the pitching frequency increases, the

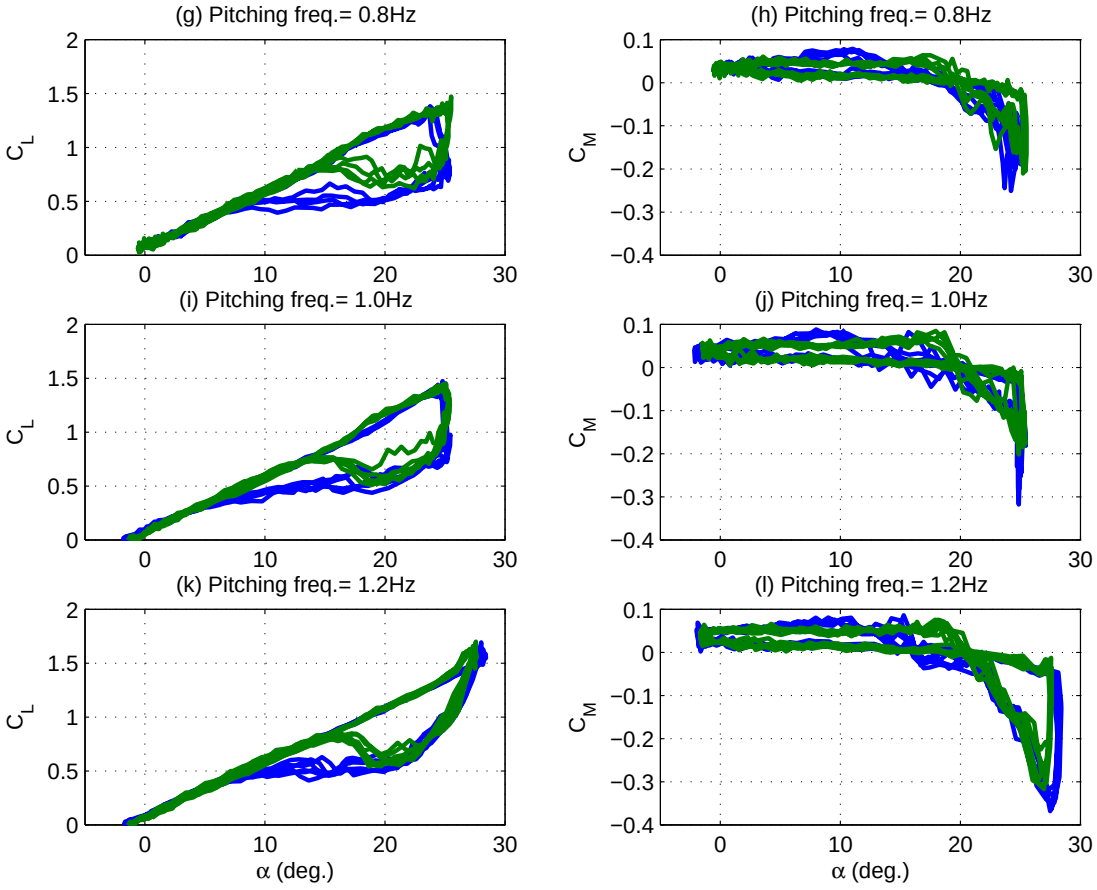

Fig. 20. Continued.

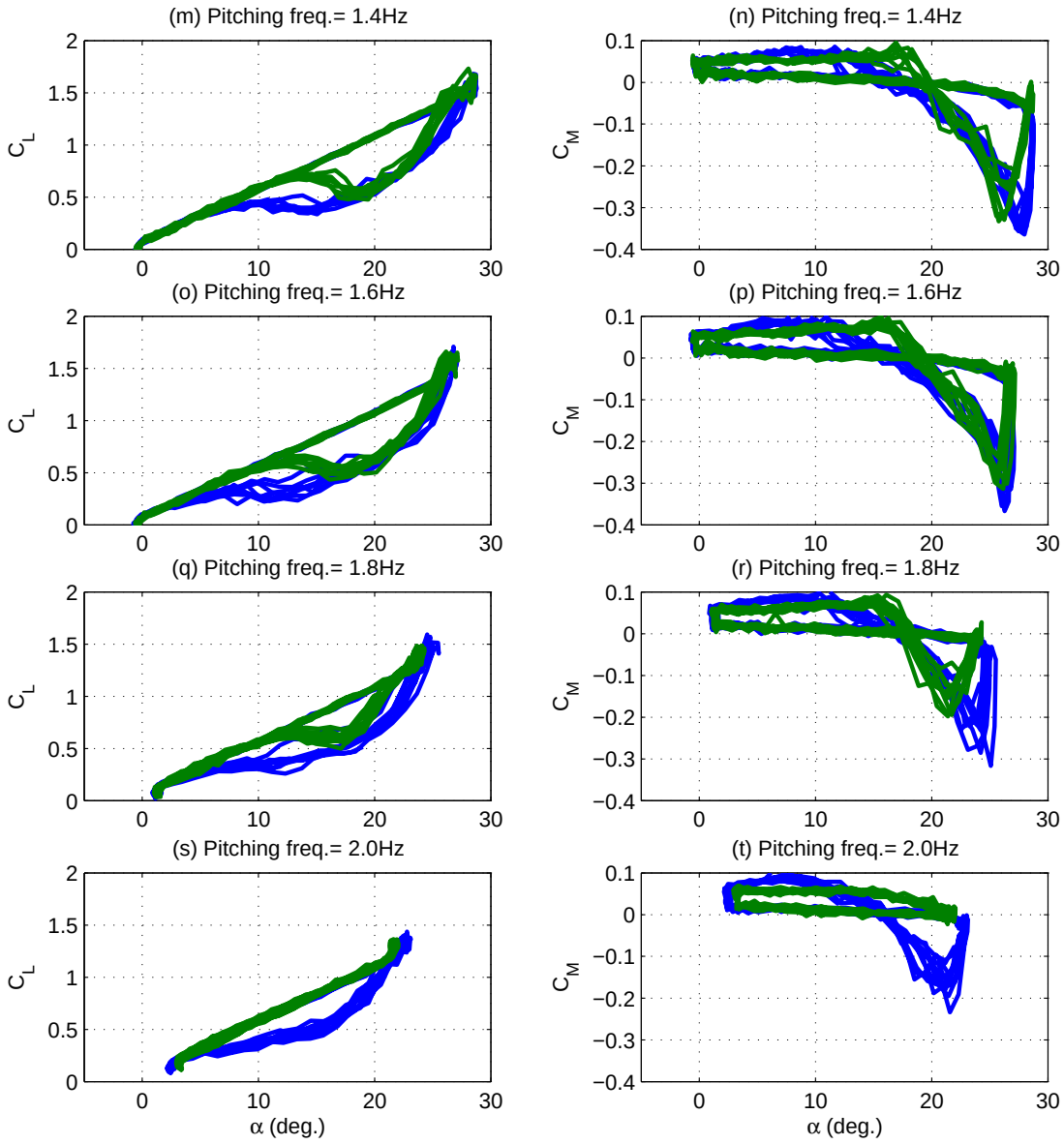

Fig. 20. Continued.

onset of the stall is more delayed up to the maximum pitching angle (25°) and the size of the hysteresis loop becomes larger due to the delay of the flow reattachment. In contrast, the plots with the jet actuation show the different characteristics. Regardless of the pitching frequency, the flow keeps attached up to 25° for pitch-up cycle and the sizes of hysteresis loop decrease considerably. It indicates that the synthetic jets force the flow to attach on the wing during the pitching movement. Above the pitching frequency 1.0 Hz, typical dynamic stall effects are observed in Figs. 20(j)-(t). The dynamic stall vortices (DSV) caused by the fast pitching motion delay the onset of the stall up to the maximum pitching angle even without the jet actuation [33]. However, synthetic jets still strengthen the reattachment mechanism such that the hysteresis loops are diminished during the pitch-down movement. In addition, the jets barely influence the C_L at low AOA during the pitch-up cycle, since the flow is attached during this cycle, even for the baseline condition [32]. These results verify again that synthetic jets are effective only to the condition of flow separation, as discussed in the previous static test.

CHAPTER III

NONLINEAR SYSTEM IDENTIFICATION

A. Overview

As synthetic jets are a series of large unsteady vortical structures, physical modeling based on Navier-Stokes equations is significantly demanding. Furthermore, the flow model in this research is to have a synthetic jet velocity as an input and a pressure as an output. Therefore, it is suitable to build a SISO dynamic model directly via parameter estimation of input-output data relationships. For this purpose, a NARMAX identification method is introduced. The NARMAX method is a nonlinear extension of an ARMAX identification method and has a wide area of application, from real system identification to the analysis of nonlinear differential equations with strong nonlinearities. A NARMAX equation is

$$y(k) = F\begin{bmatrix} y(k-1),\ldots,y(k-n_y),x(k-1),\ldots,x(k-n_x), \\ \varepsilon(k-1),\ldots,\varepsilon(k-n_\varepsilon) \end{bmatrix} + \xi(k),$$

where $F[\cdot]$ denotes a nonlinear function, x and y are discrete-time input and output signals. ε and ξ stand for possible noise and residual error. The nonlinear function F can be a polynomial, rational function, radial basis functions, or any other function subject to some mild constraints [51].

In this chapter, particularly, a polynomial NARX (NARMAX with the noise terms excluded) is implemented, neglecting the noise terms. The advantage of the polynomial NARX model is that the model is linear with respect to model parameters. Hence, the well-defined least squares method can be applied to estimate the parameters. In what follows, the procedures combining the structure selection and parameter estimation for the polynomial NARX are discussed.

B. Polynomial NARMAX

The general formulation for a polynomial NARX system identification can be written as

$$y(k) = \sum_{i=1}^{m} \theta_i x_i(k) + \xi(k) \quad \text{for } k = 1, 2, \ldots, n, \tag{3.1}$$

where y is the measured output, x_i the regressor terms, θ_i the model coefficients and ξ the residual error. m and n denote the number of regressors and data for the identification respectively. A vector form of (3.1) is

$$Y = X\Theta + \Xi, \tag{3.2}$$

where $Y, \Xi \in R^{n\times 1}$, $\Theta \in R^{m\times 1}$ and $X \in R^{n\times m}$.

The polynomial structure leads to a formulation for the regressor term as follows [54].

$$\begin{aligned} & x_i(k) = \prod_{j=1}^{p} y\left(k - n_{yj}\right) \prod_{k=1}^{q} u\left(k - n_{uk}\right), \\ & x_1(k) = 1, \\ & i = 2 \ldots n,\ p, q \geq 0,\ 1 \leq p + q \leq L, \\ & 1 \leq n_{yj} \leq n_y,\ 1 \leq n_{uk} \leq n_u, \end{aligned} \tag{3.3}$$

where u denotes the input data. For example, a full set of NARMAX equation for the first-order dynamics $n_y = n_u = 1$ with a second-order nonlinearity $L = 2$ is

$$\begin{aligned} \hat{y}(k) = {} & \theta_1 + \theta_2 y(k-1) + \theta_3 u(k-1) \\ & + \theta_4 y(k-1)^2 + \theta_5 y(k-1)\, u(k-1) + \theta_6 u(k-1)^2. \end{aligned} \tag{3.4}$$

As shown in (3.3), the permutations of input and output pairings generate a large number of possible regressor terms. The number of regressors in (3.4) is 6, while the case for $n_y = n_u = 3$ and $L = 2$ increases the number of regressors up to 28.

If the system structure is predetermined before the identification and only those regressors terms are included in (3.2), the least squares problem is simply defined to find the parameter vector Θ to minimize $\|Y - X\Theta\|$. However, the system structure is mostly unknown at the initial stage of the identification. If all the possible regressors are considered in the model such as (3.4), the model contains the excessively redundant terms such that it becomes more complicated and its accuracy may deteriorate. Therefore, it is crucial to obtain the parsimonious model that has the best fit to the original system with a certain criterion.

Suppose that X is a full set including all the possible regressors and $X_s \subseteq X$. The problem combining the parameter estimation and structure selection can be stated as [50]

$$\text{Select } X_s \text{ from } X \text{ and find the corresponding } \Theta_s \text{ to minimize } \|Y - X_s\Theta_s\|.$$

It is very demanding to achieve the optimal solution for this problem, since all the possible subset X_s should be examined. Hence, the suboptimal approach to select the model structure is introduced in Section D.

In what follows, the orthogonal least squares method with forward selection algorithm [55] is implemented to identify the significant terms among all the possible terms and calculate the corresponding Θ_s simultaneously. Appendix C contains the MATLAB® source codes for the NARMAX identification discussed in this chapter.

C. Parameter Estimation

The analytical least squares solution of (3.2) is well known as

$$\Theta = (X^T X)^{-1} X^T Y. \tag{3.5}$$

However, the numerical computation of the pseudo-inverse matrix $(X^T X)^{-1}$ has severe drawbacks since this matrix is often ill-conditioned and inaccurate results are produced. Therefore, the orthogonal least squares (OLS) method first projects the regressor vectors X into the orthogonal subspace W. This is called orthogonalization. The projected form of X into W is

$$\begin{aligned} X &= W \cdot A, \\ &= [W_1 \dots W_m] \begin{bmatrix} 1 & \alpha_{12} & \alpha_{13} & \cdots & \alpha_{1m} \\ & 1 & \vdots & & \vdots \\ & & \ddots & & \vdots \\ & 0 & & \ddots & \alpha_{m-1m} \\ & & & & 1 \end{bmatrix}, \end{aligned} \tag{3.6}$$

where the regression matrix, $W \in R^{n \times m}$, consists of orthogonal column vectors $[W_1 \dots W_m]$ and $A \in R^{m \times m}$ is the upper triangular matrix. Due to the orthogonality, $W^T W = D$ where D is a positive diagonal matrix.

The auxiliary model of (3.2) can be written as

$$Y = \hat{Y} + \Xi = Wg + \Xi, \tag{3.7}$$

where $g = A\Theta$. Consequently, The least squares problem to minimize the norm $\|Y - X\Theta\|$ in (3.1) is converted into the same problem for $\|Y - Wg\|$ in (3.7), for which the least squares solution is

$$g = \left(W^T W\right)^{-1} W^T Y = D^{-1} W^T Y, \tag{3.8}$$

where D^{-1} has better numerical properties than $(X^T X)^{-1}$ in (3.2) such that the accuracy of the solution can be improved.

Any orthogonalization method such as Gaussian elimination, Cholesky decomposition, classical Gram-Schmidt (CGS), modified Gram-Schmidt (MGS), Householder trans-

formation, Givens method and singular value decomposition are available to solve this problem. In this research, the MGS method is implemented due to its simplicity and easy computer programmability. In addition, the MGS is more stable and has less round-off errors than the CGS.

The MGS process calculates W and A in (3.6) recursively [50]. The MGS procedure at the kth iteration step is

$$\begin{cases} W_k = X_k^{(k-1)}, \\ \alpha_{ki} = \dfrac{\left\langle W_k, X_i^{(k-1)} \right\rangle}{\langle W_k, W_k \rangle}, \qquad \text{for } X_i^{(0)} = X_i,\ k = 1 \ldots m-1,\ i = k+1 \ldots m, \\ X_i^{(k)} = X_i^{(k-1)} - \alpha_{ki} W_k, \end{cases} \tag{3.9}$$

where the superscript $(\cdot)^{(k)}$ stands for the kth iteration step. At the last mth step, $W_m = X_m^{(m-1)}$. From the calculated W_k, the elements of g are computed by

$$\begin{cases} g_k = \dfrac{\left\langle W_k, X^{(k-1)} \right\rangle}{\langle W_k, W_k \rangle}, \text{for } Y^{(0)} = Y,\ k = 1 \ldots m. \\ Y^{(k)} = Y^{(k-1)} - g_k W_k, \end{cases} \tag{3.10}$$

After computing A and g, Θ can be readily calculated from $g = A\Theta$ by backward substitution as follows.

$$\begin{aligned} \theta_m &= g_m, \\ \theta_k &= g_k - \sum_{j=k+1}^{m} \alpha_{kj} \theta_j \quad \text{for } k = m-1, m-2, \ldots, 1. \end{aligned} \tag{3.11}$$

D. Structure Selection

If the structure of the nonlinear system is unknown, the most important point in the system identification is not to miss the significant regressor terms which should be included in the resulting model [50]. The most apparent approach to select m_s significant regressor

terms out of a set of m given regressors is to examine all the possible different models, the number of which is $2^m - 1$. This requires the demanding computation and is not possible in practical application except very simple systems.

As an efficient strategy for selecting the suboptimal subset, three approaches are widely known: forward selection, backward selection and stepwise selection [56]. In this research, the forward selection method is implemented, combining with the orthogonal least squares method. The procedure of this algorithm [57] is.

1. At the first step, the basis vector, which best fit the data set with certain criterion, is selected from W.

2. Iteratively, the basis vector is selected from the remainder of W by a certain criterion and is combined to the previously selected set of basis vectors.

A measure of significance of a regressor, which will be used as the criterion for the forward selection, is derived as follows. Suppose that $W_s \in R^{n \times m_s}$ is the orthogonal set corresponding to the subset X_s. Assuming that the residual error, Ξ, is not correlated to the input and output, the mean square prediction error (MSPE) of the subset W_s can be derived as

$$\begin{aligned} MSPE &= \frac{1}{n}\left(Y - \sum_{i=1}^{m} W_i g_i\right)^T \left(Y - \sum_{i=1}^{m} W_i g_i\right), \\ &= \frac{Y^T Y - \sum_{i=1}^{m} W_i^T W_i g_i^2}{n}. \end{aligned} \tag{3.12}$$

,where the term $W_i^T W_i g_i^2$ stands for the contribution of the regressor vector W_i into the error. If this value is comparably large, it means that the MSPE will be reduced considerably by adding the regressor W_i into the model. As a result, the error reduction ratio (ERR) for the term W_i is defined as

$$ERR_i = \frac{W_i^T W_i g_i^2}{Y^T Y}. \tag{3.13}$$

After comparing the ERR values of the remaining regressor vectors $X_i^{(k-1)}$ for $i = k, \ldots, m$ at every iteration step of the MGS procedure in (3.9), the model structure at kth step is incremented with the regressor that has the highest value of ERR [53]. The procedure is stopped if ERR is less than a preset threshold [55].

CHAPTER IV

CFD SIMULATION AND NARMAX MODELING ON A FLAT PLATE

A. Overview

CFD simulations are performed to examine the effects of synthetic jets on a boundary layer established on a flat plate. Nektar, a Navier-Stokes equation solver using hp spectral method [58, 59], is used for the simulation. The flow is assumed to be 2-dimensional, incompressible and laminar.

Boundary conditions are carefully examined to guarantee the development of the accurate boundary layer. In addition, the feasibility of an approximate synthetic jet model is investigated by the simulation in a quiescent flow. The verified boundary and jet conditions will be applied to the flow separation simulations in Chapter V.

The boundary layer simulations are performed for three different free stream velocities: $U_\infty = 15m/s, 17.5m/s, 20m/s$. A NARMAX system identification method will be applied to the simulation results to examine the flow modeling, where the effects of varying free stream velocity are accommodated into the variation of model coefficients, with an invariant model structure.

B. Nomenclature

A Amplitude of synthetic jets

d Slot width

f Synthetic jet frequency

x Streamwise direction tangential to a surface

y Cross-stream direction normal to a surface

u Streamwise velocity

v Cross-stream velocity

v_j Synthetic jet velocity

U_∞ Free stream velocity

δ Boundary layer thickness

ν Kinematic viscosity

$(\cdot)_o$ Characteristic variable for nondimensionalization

$(\cdot)^*$ Dimensionless variable

C. Synthetic Jet Model

The fundamental role of a synthetic jet actuator is to perturb a boundary layer flow by oscillatory motion. Therefore, the jet actuation can be approximated as a periodic suction/blowing velocity condition. In this research, synthetic jets are modeled as a wall-normal velocity condition with a spatial configuration $f(x)$ as follows.

$$\begin{cases} u(x, y=0, t) = 0 \\ v(x, y=0, t) = A \cdot f(x) \cdot \sin(2\pi f t) \end{cases}, \quad \text{for } 0 < x/d < 1, \tag{4.1}$$

where x denotes the streamwise direction tangential to a surface, y the cross-stream direction normal to a surface and u and v are the velocities for x and y directions respectively. d is a jet slot width. The temporal configuration $\sin(2\pi f t)$, which represents the periodic excitation of synthetic jets, guarantees a essential characteristic of the jets, i.e. the zero net mass flux, in the time-average sense.

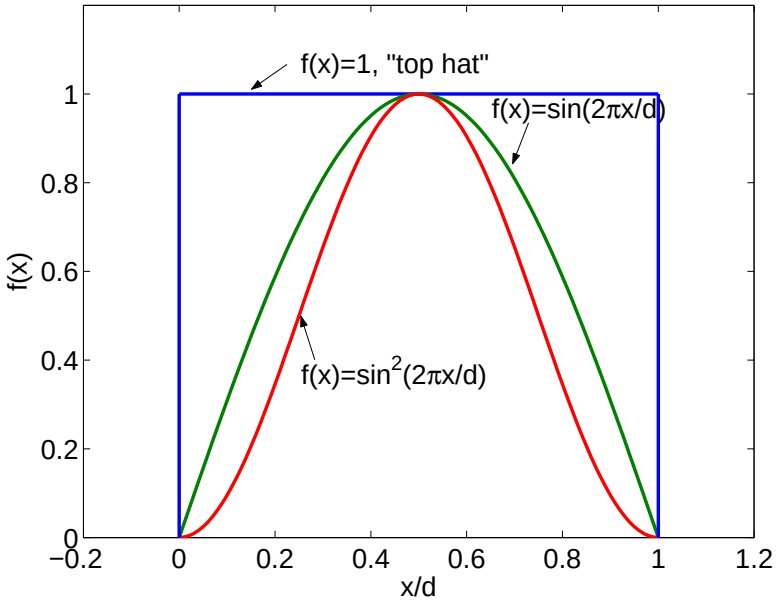

Fig. 21. Three different spatial configurations of the jets exiting the slot.

The previous experimental and numerical works [6, 12–15] present three possible analytical configurations for $f(x)$ as shown in Fig. 21. Among them, the "top hat" configuration matches most closely the experimental results, while its shape varies depending on the characteristics of slot, cavity and inner moving surface [14, 15, 60]. Although the profiles of three configurations are apparently different, all of them give similar flow solutions qualitatively [13, 60]. $\sin(2\pi ft)$ is employed for this research, since it is the simplest configuration among them and behaves numerically better than the "top hat" profile. The resultant wall-normal velocity component for synthetic jets is

$$v_j(x, y = 0, t) = A \cdot \sin(\frac{\pi x}{d}) \cdot \sin(2\pi ft), \quad \text{for} \quad 0 < x < d. \tag{4.2}$$

Table I. Physical properties for the numerical simulation.

kinematic viscosity (m^2/s)	1.51×10^{-5}
slot width (mm)	1.22
distance from a leading edge to a jet exit slot (mm)	62
boundary layer thickness at a slot position, δ_o (mm, for $U_\infty = 20m/s$)	1.1323

D. CFD Simulation

1. Nondimensionalization

As shown in Table I, physical properties for the simulation refer to the parameters of the previous wind tunnel experiments in Chapter II. The jet amplitude is assumed to be 4 m/s and the jet exit slot is placed at the origin of the simulation coordinates and the boundary layer thickness at the slot is calculated via the Blasius boundary layer equation [61].

The parameters are nondimensionalized by a boundary layer thickness at the slot, δ_o ($= 1.1312mm$), and a free stream velocity, U_∞ ($= 20m/s$). Therefore, the convective time scale, $t_c (= \delta_o/U_\infty)$, becomes 5.6615×10^{-5} seconds. The dimensionless variables are defined as follows.

- velocity: $u^* = u/U_\infty$, $v^* = v/U_\infty$
- coordinates: $x^* = x/\delta_o$, $y^* = y/\delta_o$
- time: $t^* = t/t_c$
- pressure: $p^* = p/\rho U_\infty^2$, where ρ is a density.
- frequency: $f^* = f \cdot t_c$

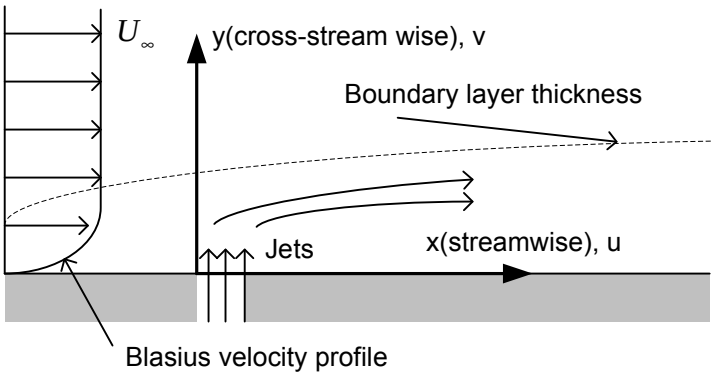

Fig. 22. Schematic diagram of CFD simulation conditions.

- Reynolds number: $\mathrm{Re} = U_\infty \delta_o / \nu$

In what follows, the asterisk representing a dimensionless variable is omitted for convenience. The dimensional values are highlighted in parentheses if necessary.

2. Boundary Conditions and Grid Distribution

The schematic diagram for the CFD simulations on a flat plate is shown in Fig. 22. Since the essential effects of synthetic jets stem from the interaction of the jets with the boundary layer, the boundary conditions for the simulation domain should be properly implemented to ensure the accurate establishment of a laminar boundary layer on the flat plate in the absence of jet actuation.

In what follows, the effects of boundary conditions are discussed with an emphasis on the inlet velocity condition that contributes mostly to the properties of the boundary layer. As shown in Fig. 23, suppose that the domain S_2, which corresponds to a rectangle **ABCD**, is the main domain where the synthetic jet will be ejected and a domain S_1, which corresponds to a rectangle **EFGH**, is the upstream domain overlapped with the main domain S_2.

Considering the domain S_2, the streamwise velocity u and cross-stream velocity v within the boundary layer thickness δ_2 at the inlet boundary **DA** is readily computed from

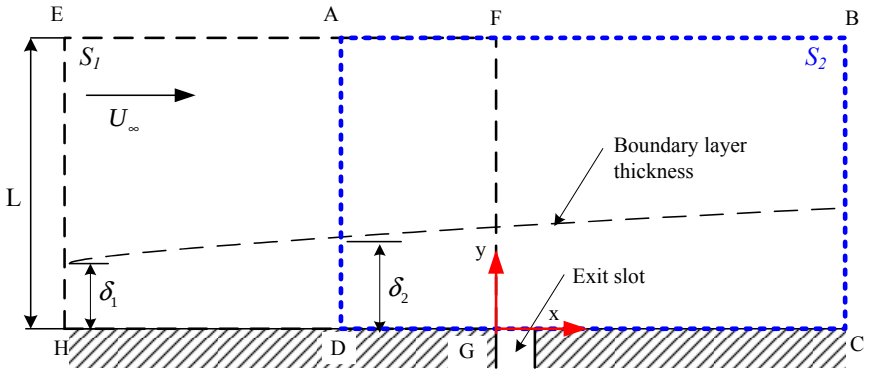

Fig. 23. Two overlapped domains to compute the v profile of inlet velocities at **DA**.

the Blasius equation [61]

$$f'''(\eta) + f f''(\eta) = 0, \quad \text{for} \quad \eta = y\sqrt{\frac{U_\infty}{2\nu x}}, \tag{4.3}$$

where the boundary conditions are

$$\begin{aligned} \eta = 0 &: f = 0, \quad f' = 0, \\ \eta \to \infty &: f' = 1. \end{aligned} \tag{4.4}$$

Using (4.3) and (4.4), the velocity components are obtained as

$$\begin{aligned} u/U_\infty &= f'(\eta), \\ v/U_\infty &= \sqrt{\frac{\nu}{2xU_\infty}}\left(\eta f' - f\right), \end{aligned} \tag{4.5}$$

where if $\eta \to \infty$, then

$$\begin{aligned} u/U_\infty &\to 1, \\ v/U_\infty &\to 0.8604\sqrt{\frac{\nu}{xU_\infty}}. \end{aligned} \tag{4.6}$$

In contrast, as $y \to \infty$, $u \to U_\infty$ and $v \to 0$ in real world. Therefore, the Blasius solution does not provide the v profile outside the boundary layer. The procedure to obtain the profile of v for $y > \delta$ is proposed as follows:

1. The simulation for the domain S_1 is performed, considering only the u component at

the inlet section **HE** such as

$$u/U_\infty = \begin{cases} u(y) & \text{for } 0 \le y \le \delta_1, \\ 1 & \text{for } \delta_1 < y \le L\ . \end{cases} \qquad (4.7)$$
$$v/U_\infty = 0 \quad \text{for } 0 \le y \le L,$$

where $u(y)$ and $v(y)$ are polynomial equations obtained by least-squares fitting (4.5).

2. From the simulation results of the domain S_1, the v data for $y > \delta_2$ at the section **DA** is obtained and the polynomial function for those velocity data is calculated by the least squares method.

3. Finally, the velocity conditions at the inlet section **DA** for the domain S_2 are given as

$$u/U_\infty = \begin{cases} u(y) & \text{for } 0 \le y \le \delta_2, \\ 1 & \text{for } \delta_2 < y \le L, \end{cases}$$
$$v/U_\infty = \begin{cases} v_1(y) & \text{for } 0 \le y \le \delta_2, \\ v_2(y) & \text{for } \delta_2 < y \le L, \end{cases} \qquad (4.8)$$

where $u(y)$ and $v_1(y)$ are polynomials obtained by least-squares fitting (4.5) and $v_2(y)$ is a polynomial obtained at the section **DA** of the domain S_1.

The proposed method is demonstrated in the exemplary domain of Fig. 24. The simulations are performed for three different boundary setups in Table II. The velocity profiles in the case 3 are obtained according to the aforementioned procedure. The outlet boundary condition for **BC** is fixed as an “out flow” condition that stands for the zero Neumann

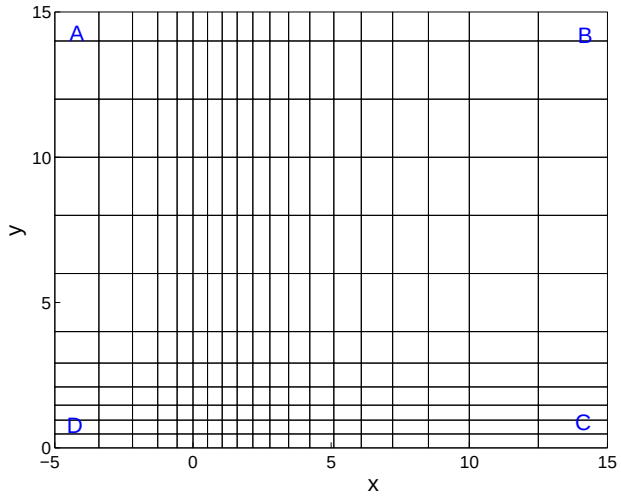

Fig. 24. Exemplary domain to examine the proposed approximation of inlet velocity condition.

Table II. Three different boundary setups for the domain shown in Fig. 24.

	inlet (**DA**)	top (**AB**)
case **1**	u=Blasius, v=0	u=1, v=0
case **2**	u=Blasius, v=0	out flow
case **3**	u=Blasius, v=approximated	out flow

boundary condition. The u profile for the cases 1, 2 and 3 is

$$u(y) = \begin{cases} a_6\left(\frac{y}{\delta}\right)^6 + a_5\left(\frac{y}{\delta}\right)^5 + a_4\left(\frac{y}{\delta}\right)^4 + a_1\left(\frac{y}{\delta}\right) & \text{for } 0 \le y \le \delta, \\ u(y) = 1 & \text{for } y > \delta, \end{cases} \tag{4.9}$$

The approximate v profile for the case 3 is

$$v(y) = \begin{cases} b_5\left(\frac{y}{\delta}\right)^5 + b_4\left(\frac{y}{\delta}\right)^4 + b_3\left(\frac{y}{\delta}\right)^3 + b_2\left(\frac{y}{\delta}\right)^2 + b_1\left(\frac{y}{\delta}\right) & \text{for } 0 \le y \le \delta, \\ c_3\left(\frac{y}{\delta}\right)^3 + c_2\left(\frac{y}{\delta}\right)^2 + c_1\left(\frac{y}{\delta}\right) + c_0 & \text{for } y > \delta, \end{cases} \tag{4.10}$$

where $\delta = 0.95324$. The coefficients of each polynomial are obtained by the least squares as

$$\begin{bmatrix} a_6 = -0.7811268 \\ a_5 = 3.1483253 \\ a_4 = -3.1798729 \\ a_1 = 1.8116373 \end{bmatrix}, \quad \begin{bmatrix} b_5 = 3.3072589 \\ b_4 = -5.4936840 \\ b_3 = -0.6395915 \\ b_2 = 3.8066682 \\ b_1 = 0.0192855 \end{bmatrix}, \quad \begin{bmatrix} c_3 = 3.1735311e-5 \\ c_2 = -2.7670147e-5 \\ c_1 = -0.0197532 \\ c_0 = 1.0230694 \end{bmatrix} \tag{4.11}$$

The simulation results for each case are compared with the Blasius solutions. Figure 25 presents the u and v velocity distributions normal to the surface. The u profiles for each case are almost identical to the Blasius solution, while the v profile of the case 3 shows the smallest error compared with those of the cases 1 and 2. Figure 26 presents the effects of each boundary setup on the wall pressure and shear stress distributions. It also confirms the case 3 is the best approximation to the Blasius solution. Therefore, the proposed method, which corresponds to the case 3, improves effectively the accuracy of boundary layer simulation.

For synthetic jet simulation, the grid distribution and boundary conditions of the flat plate for $U_\infty = 20m/s\,(\mathrm{Re} = 1608)$ is shown in Fig. 27. Regarding the inlet condition, the

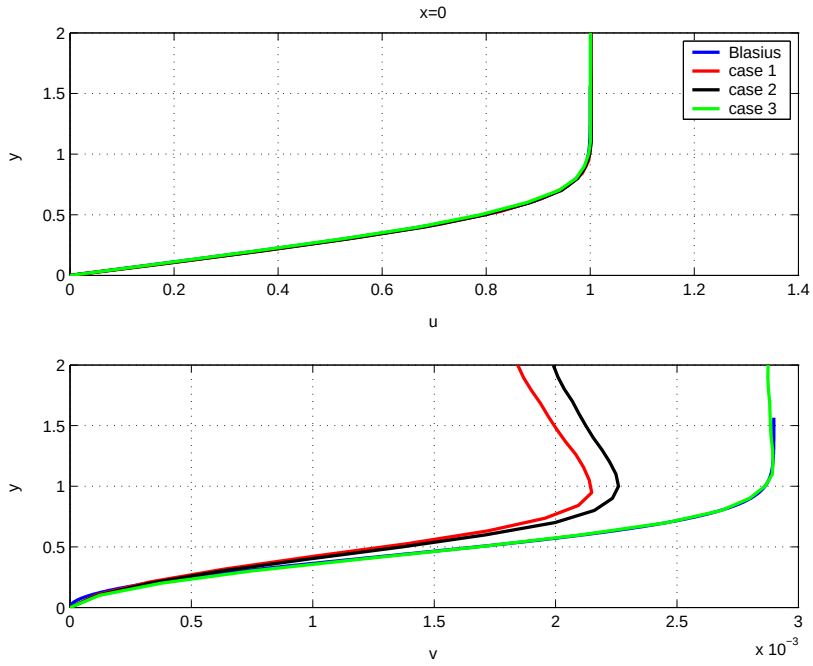

(a) u(top) and v(bottom) at $x = 0$.

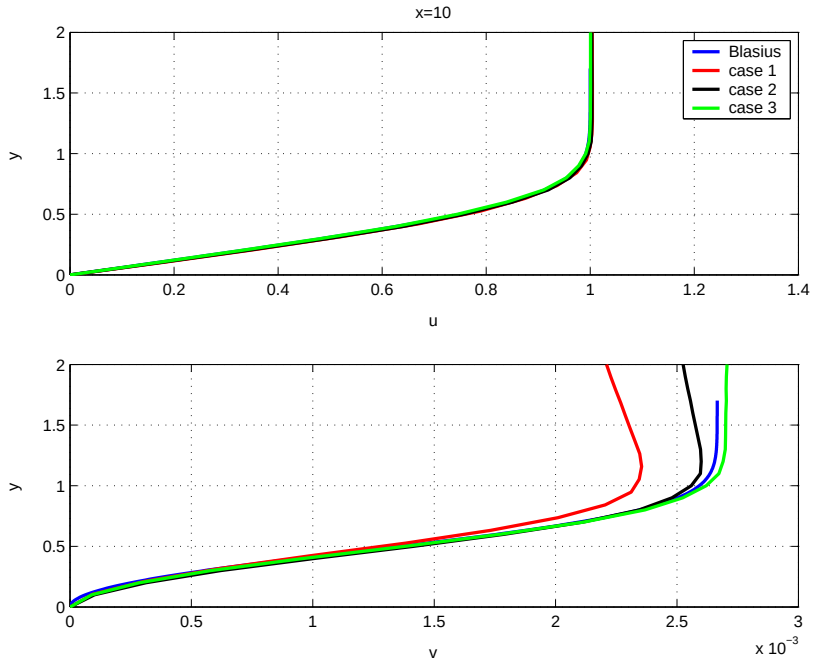

(b) u(top) and v(bottom) at $x = 10$.

Fig. 25. u and v profiles at different x coordinates.

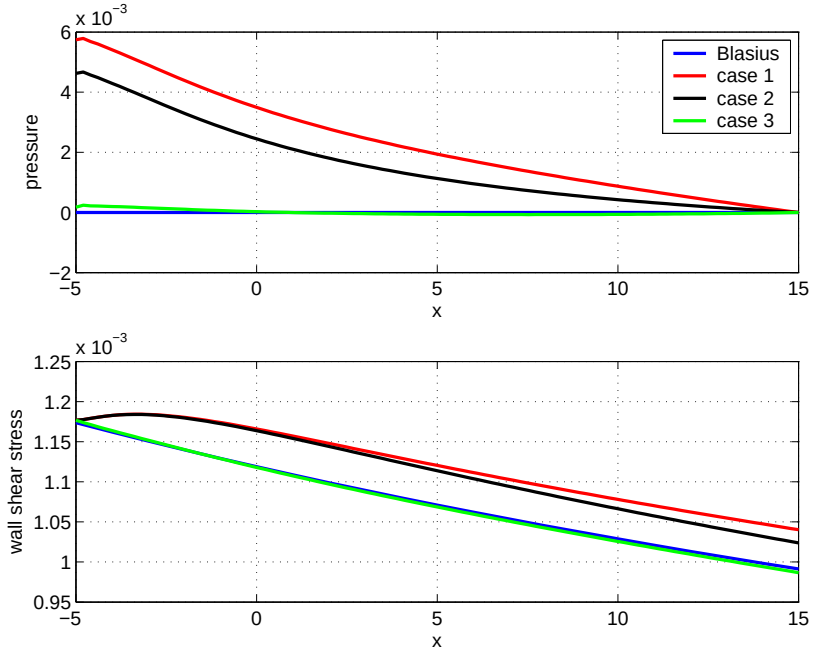

Fig. 26. Comparison of wall pressure (top) and shear stress (bottom) distributions for different cases of boundary conditions.

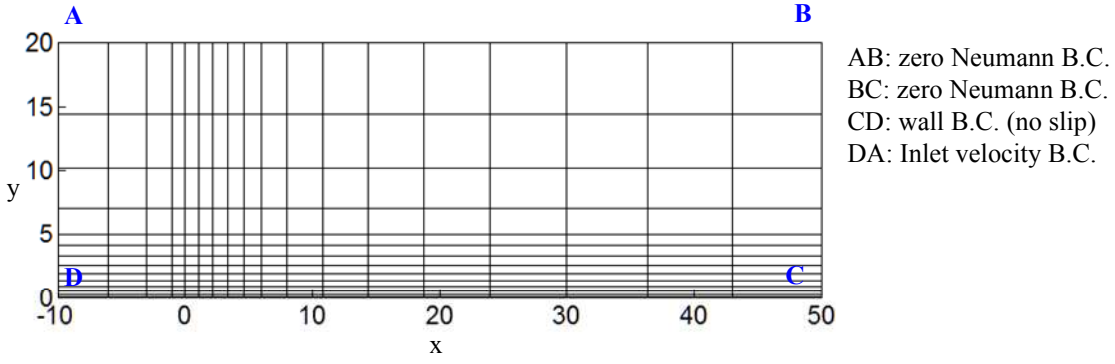

Fig. 27. Grid distribution and boundary conditions for Re = 1608.

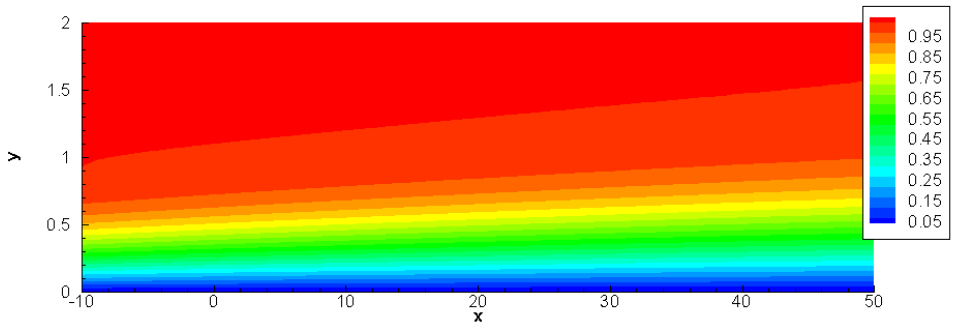

Fig. 28. Contour plot for u velocity in the absence of jet actuation.

u profile is the same with (4.9), where $\delta = 0.90408$. The v profile is given as

$$v(y) = \begin{cases} b_6\left(\frac{y}{\delta}\right)^6 + b_5\left(\frac{y}{\delta}\right)^5 + b_4\left(\frac{y}{\delta}\right)^4 + b_3\left(\frac{y}{\delta}\right)^3 + b_2\left(\frac{y}{\delta}\right)^2 + b_1\left(\frac{y}{\delta}\right) & \text{for } 0 \le y \le \delta, \\ c_4\left(\frac{y}{\delta}\right)^4 + c_3\left(\frac{y}{\delta}\right)^3 + c_2\left(\frac{y}{\delta}\right)^2 + c_1\left(\frac{y}{\delta}\right) + c_0 & \text{for } y > \delta, \end{cases} \tag{4.12}$$

where the coefficients are

$$\begin{bmatrix} b_6 = -2.9515234 \\ b_5 = 12.611868 \\ b_4 = -17.355315 \\ b_3 = 6.9570714 \\ b_2 = 1.6703334 \\ b_1 = 0.0690778 \end{bmatrix}, \quad \begin{bmatrix} c_4 = -8.3752616e-7 \\ c_3 = 5.5604674e-5 \\ c_2 = -5.3324697e-4 \\ c_1 = -2.2585047e-2 \\ c_0 = 1.0266406 \end{bmatrix}. \tag{4.13}$$

The number of total elements is 252 and the grids are clustered with respect to the jet slot at $0 \le x \le 1.06, y = 0$. The distance from the jet slot to the outlet boundary is 50, enough to prevent the convected vortices from reflecting at the outlet boundary. The polynomial order of the spectral method is 14 and the time step for the simulation is 0.002.

Figure 28 presents a u velocity contour plot in the absence of jet actuation, implementing the aforementioned boundary conditions. This snapshot in steady-state will serve as an initial condition for the following simulations of synthetic jet actuation.

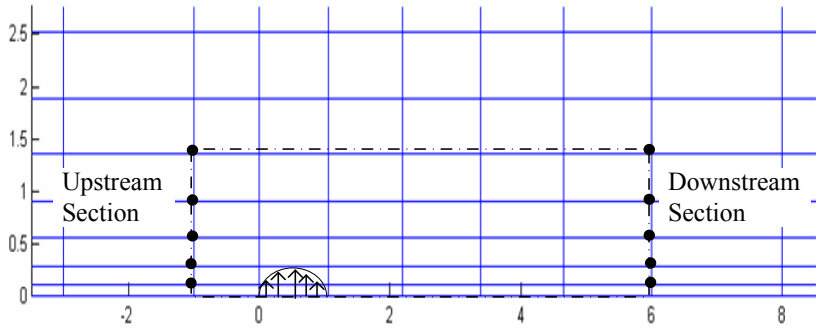

Fig. 29. Coordinates (dots) where time-series data are captured.

The magnitude of synthetic jet actuation is 4 m/s. Time-series data for velocity and pressure are captured at the coordinates in Fig. 29. The downstream data is collected farther from the jets than the upstream data, since vortices created by the jet are fully developed at 4 to 5 times the slot width away from the slot.

3. Synthetic Jets in Quiescent Flow

Before investigating the interaction of synthetic jets with cross flow, synthetic jet actuation is examined in a quiescent flow. It helps verifying the assumed jet model and assessing the formulation of synthetic jets.

Synthetic jets in a quiescent flow result from the interactions of a series of vortices that are created by periodically repeating suction and blowing of flow across the slot. During the blowing period, the exiting flow separates at both edges of the slot and rolls into a pair of vortices as shown in Fig. 30(a). During the suction period, the flow in the vicinity of the slot comes into the slot and the created pair of vortices depart from the slot with their own self-induced velocity as shown in Fig. 30(b) [6].

A series of the vortex pairs are symmetric with respect to the centerline of the jets and the flows in each vortex of the pair rotate to the counterclockwise and clockwise directions respectively. Typically, the moving mechanisms of synthetic jet actuators, e.g. acoustic

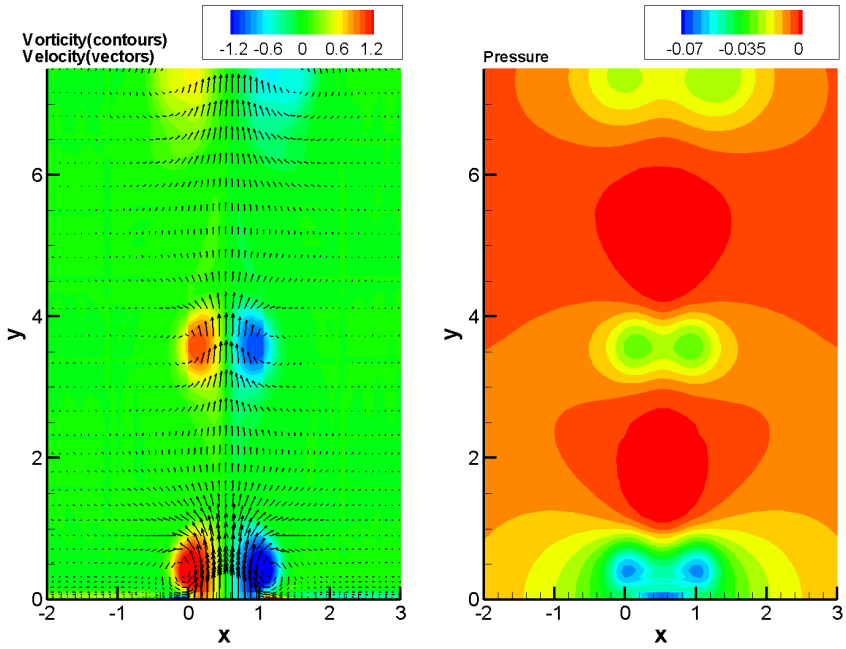

(a) At the peak blowing.

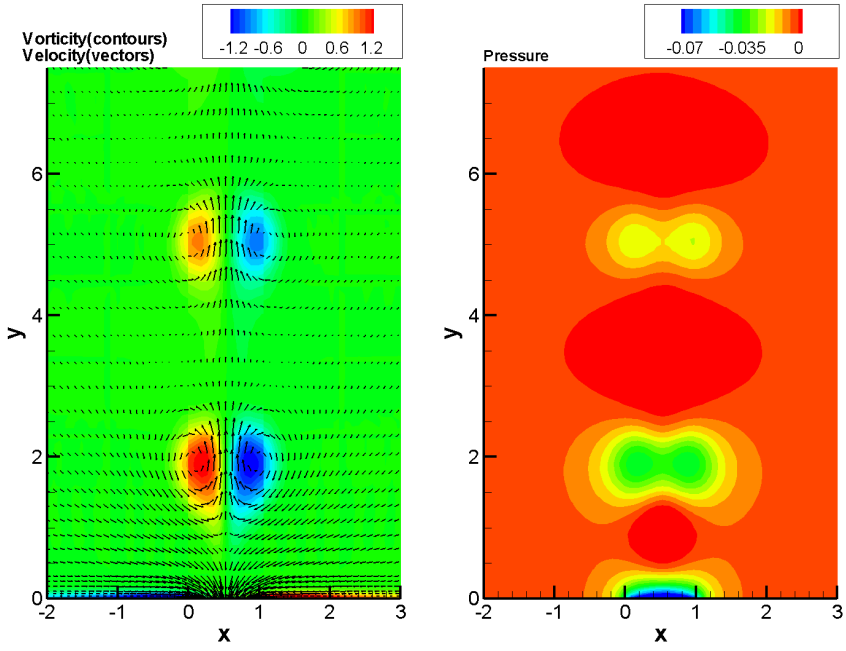

(b) At the peak suction.

Fig. 30. Vorticity (left) and pressure (right) contour plots for the synthetic jet actuation with $f = 0.0396$ (700 Hz). The arrows denote the velocity vectors.

waves or the motion of a diaphragm or a piston, induce the pressure drop which alternates periodically across the exit slot. Such pressure variations in the vicinity of the slot can be observed in Fig. 30.

Although the simulations in this research do not take into account the high-fidelity modeling for the synthetic jet actuation consisting of orifice, cavity and inner moving boundary, the results validate that the assumed velocity condition in (4.2) contains the essential characteristics of synthetic jets.

4. Interaction of Synthetic Jets with a Boundary Layer

With the Reynolds number Re $= 1608$ ($U = 20$ m/s), the effects of synthetic jet frequency are presented in Fig 31. The jet frequencies are given by f =0.0057 (100 Hz), 0.0226 (400 Hz).

Figures 31(b) and 31(c) present the interaction of the synthetic jets with the boundary layer by means of vorticity contours, compared with Fig. 31(a) in the absence of jet actuation, A pair of vortices are created during the blowing period, while those are asymmetric unlike the case for the quiescent flow. The approaching boundary layer flow, which has the clockwise vorticity, weakens the counterclockwise vortex and the separation bubble in the lee of the clockwise vortex is created. This bubble, confirmed in the previous experiments [62, 63], is presumably due to the blockage effect of the jet. Consequently, the streamlines of the crossing boundary layer flow are displaced. However, those vortices can not escape out of the boundary layer, since the jet magnitude is comparably less than the free stream velocity. During the following suction period, this vorticity moves away from the jet exit and travel downstream close to the wall, while maintaining its structure. This is a unique characteristic that cannot be observed in continuous suction or blowing and promotes the effective transference of high momentum of free stream into the boundary layer. As the jet frequency increases, the size of the separation bubble decreases and the distances

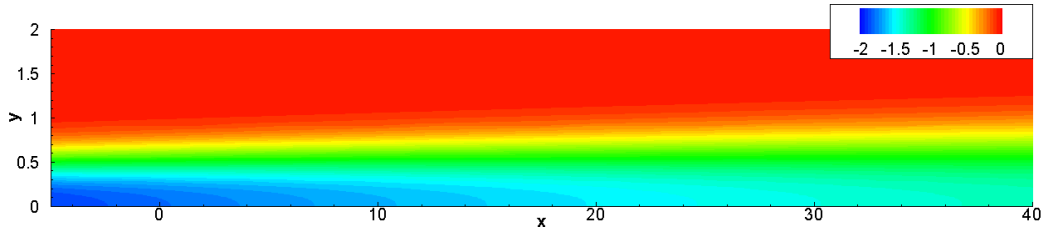

(a) In the absence of jet actuation.

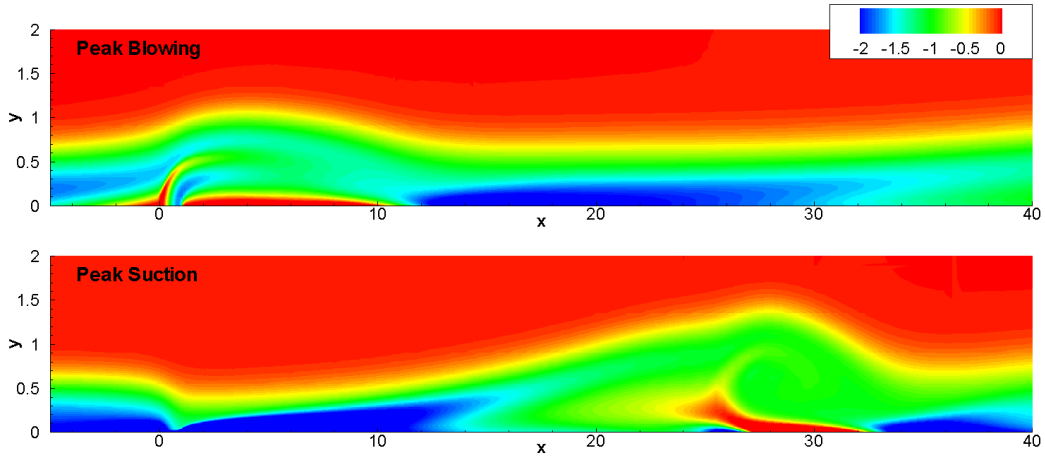

(b) For the synthetic jet frequency $f = 0.0057$ (100 Hz).

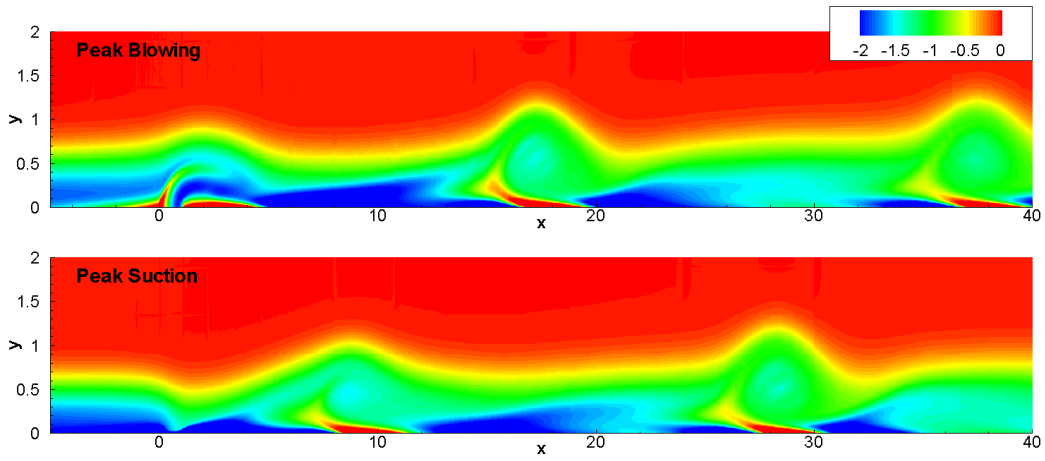

(c) For the synthetic jet frequency $f = 0.0226$ (400 Hz).

Fig. 31. Vorticity contour plots at the moment of peak blowing and suction of the synthetic jet actuation.

between each bubble become closer.

Examination of time-series data also confirms the mechanism of synthetic jet actuation. Figure 32 presents the time-series data at the upstream and downstream cross-section points described at Fig. 29. The coordinates of the measuring points are (-1.0, 0.1) on the upstream section and (6.0, 0.1) on the downstream section. Evidently, the plots for the upstream and downstream data show the considerable difference. The upstream velocities and pressure responses show the smooth curves similar to simple sinusoids, while the downstream data contain strong nonlinear characteristics which vary with depending on the jet frequency. This distinction is due to the fact that the vortices created by the actuation convect following the direction of the free stream so that those influence only the downstream flow. For the downstream data at x=6.0, the negative ranges of the u velocity indicate the reversed flow, during which the v velocity for $f = 0.0226$ shows abrupt transition, while the v velocity for $f = 0.0057$ displays slight fluctuation. The sharp peaks correspond to the moment at which the separation bubble crosses the measuring point. Therefore, a nonlinear system identification method is necessary to construct a dynamic model for the downstream flow response.

The mean velocity profiles at downstream are compared with the baseline profile of the laminar boundary layer flow in Fig. 33. The mean velocity distribution does not show any reverse flow. Interestingly, the velocities for $0 \leq y < 0.25$ at x =2.5, 5 exceed the baseline profile slightly. These overshoots can be detected similarly if steady jets blow tangentially along the wall [61]. Comparing the velocity profiles of $f = 0.0057$ (100 Hz) and $f = 0.0226$ (400 Hz), the velocity profile of $f = 0.0057$ (100 Hz) approaches to the profile of $f = 0.0226$ (400 Hz) as the distance from the slot increases and the profile of $f = 0.0226$ (400 Hz) vary little for the entire downstream distance. As the jet frequency increases, the velocity profile converges to a certain shape within a shorter distance.

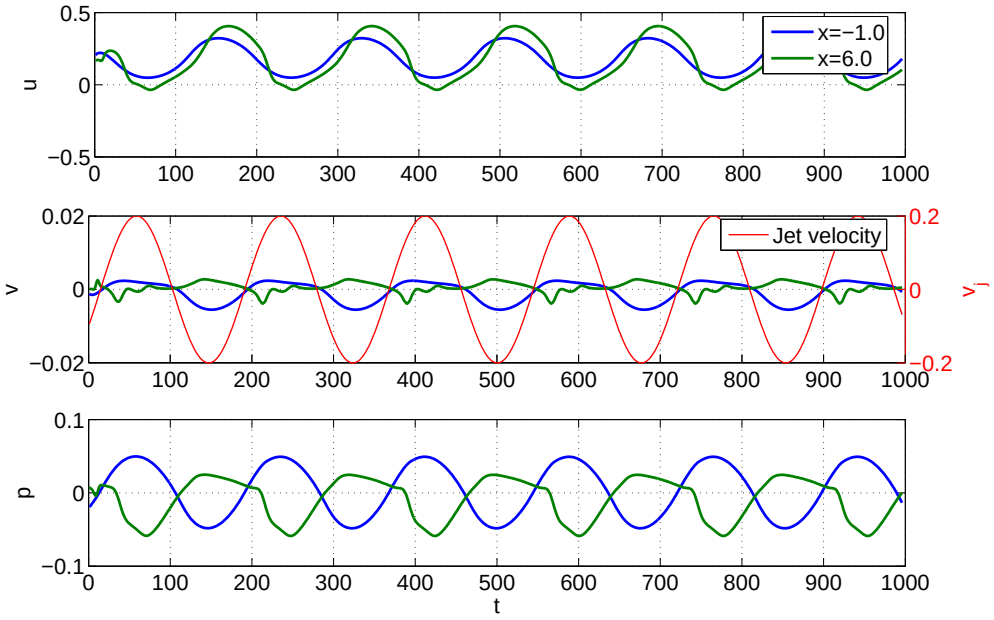

(a) for the synthetic jet actuation $f = 0.0057$ (100 Hz).

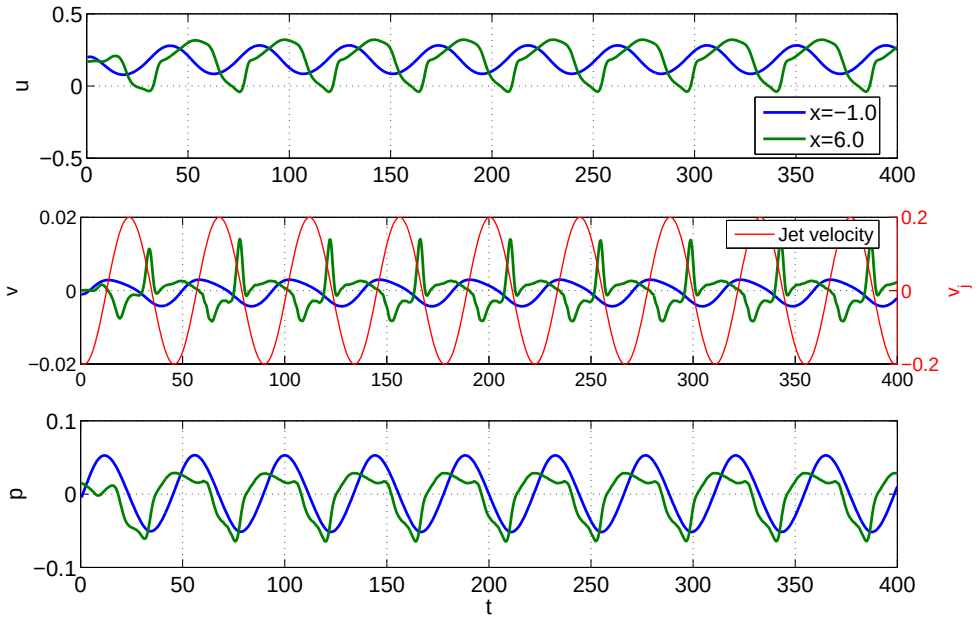

(b) for the synthetic jet actuation $f = 0.0226$ (400 Hz).

Fig. 32. Time-series data of *u* (top), *v* (middle) and *p* (bottom) at upstream (x=-1.0, y=0.1) and downstream (x=6.0, y=0.1) cross section points. The red lines stand for the jet velocity with respect to the right axis.

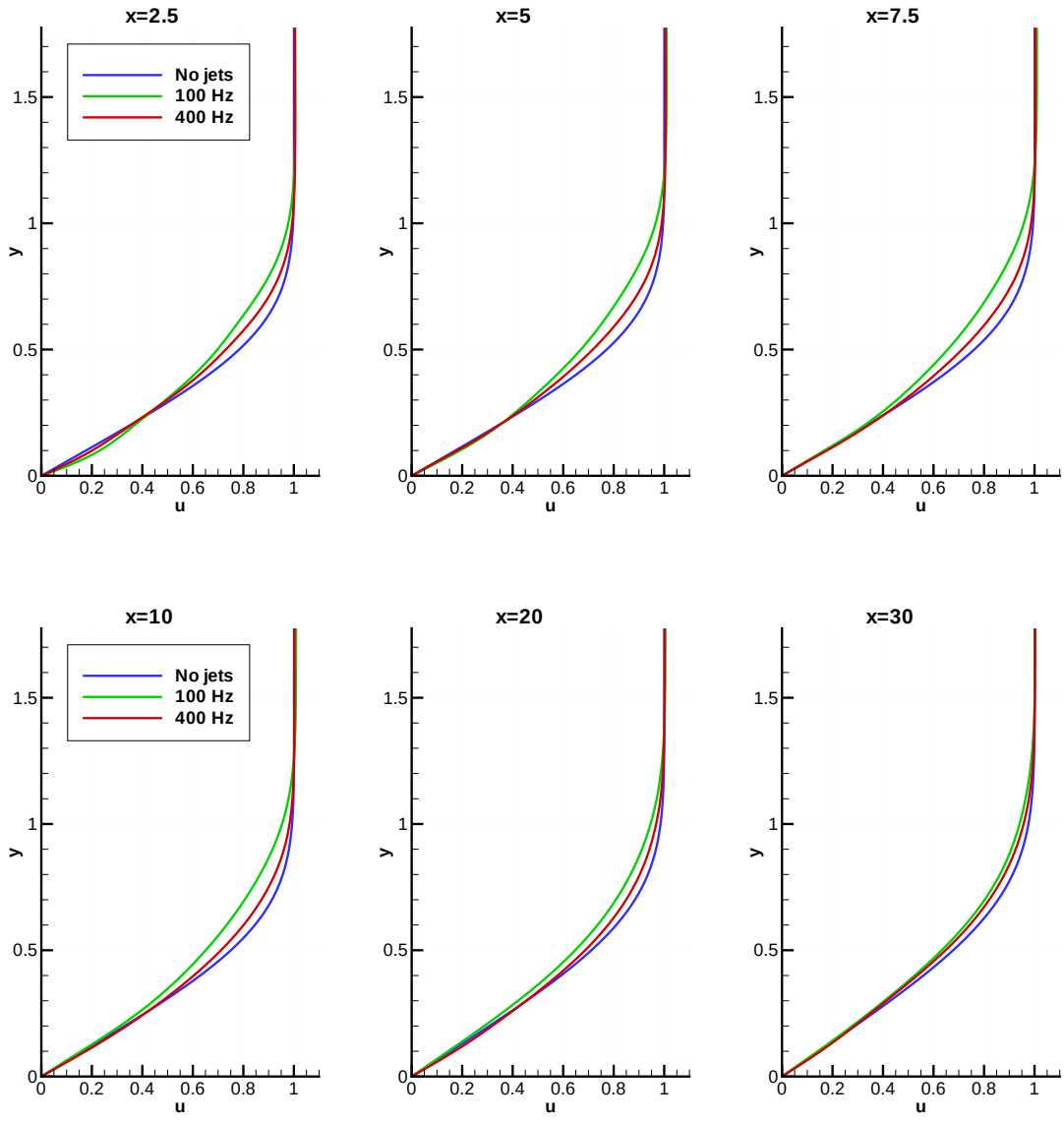

Fig. 33. Mean u profiles at the cross sections of $x = 2.5, 5, 7.5, 10, 20, 30$ for different synthetic jet frequencies.

E. Modeling of Synthetic Jets

An input signal for system identification should have sufficient frequency contents to cover the important frequency bandwidth of the system. Consequently, a chirp signal is chosen as an input for the identification, since it shows good control in the excited frequency band [64] and its sinusoidal characteristic matches the nature of synthetic jet actuation. The proposed chirp signal is

$$v_{jet} = Af(x)\sin\left\{2\pi\left(f_1 t + (f_2 - f_1)\frac{t^2}{2M}\right)\right\}, 0 \le t \le M, \tag{4.14}$$

where the instantaneous frequency increases linearly from f_1 to f_2 over a time period M.

The NARMAX identification in (3.1)) is performed on the downstream pressure response at (6.0, 0.1), with a chirp signal given as a synthetic jet velocity. The chirp signal sweeps the frequency band from 0.0028 (50Hz) to 0.0283 (500Hz) and the pressure response is acquired as shown in Fig. 34. As for the order of the model, a second-order dynamic system structure with second-order nonlinearities is chosen for the present study. Number of possible regressor terms are 15 including a constant term. The resultant NARMAX model is

$$\begin{aligned} p(k) =& 1.481378p(k-1) - 0.541882p(k-2) + 0.07506v(k-1) - 0.088163v(k-2) \\ &+ 1.462855p(k-2)^2 - 2.77682p(k-1)u(k-1) + 3.159657p(k-1)v(k-2), \end{aligned} \tag{4.15}$$

where p is the pressure output and v the input jet velocity. By applying the forward selection method in Chapter III, only 7 regressor terms are selected.

To validate the identified model given by (4.15), the CFD simulation and estimated results are compared for two different actuation frequencies in Figs. 35 and 36.

The time-domain responses show that the NARMAX model matches the CFD results successfully in steady-state. From the frequency spectrum analysis, the model matches

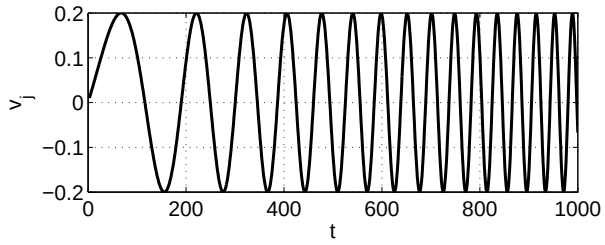

(a) Chirp signal for the jet actuation as an input.

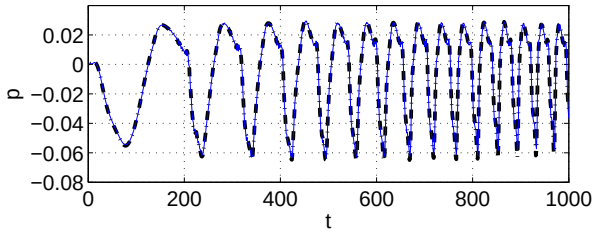

(b) Pressure outputs of the simulation (dashed) and the identified model (dotted) at (x=6,y=1).

Fig. 34. NARMAX System identification.

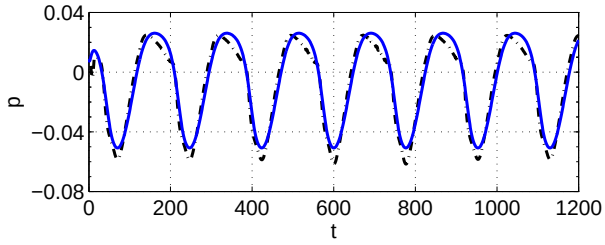

(a) Time domain response.

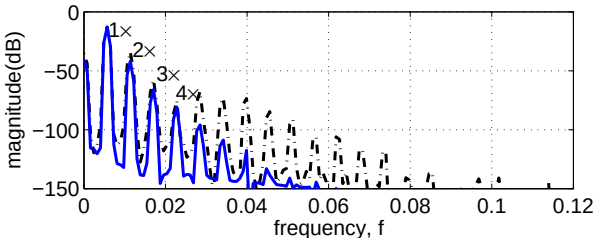

(b) Frequency spectrum.

Fig. 35. Comparison of the CFD results (dashed) and the NARMAX model response (solid) for $f = 0.0057$ (100Hz).

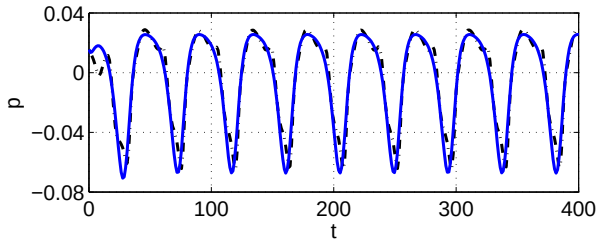

(a) Time domain response.

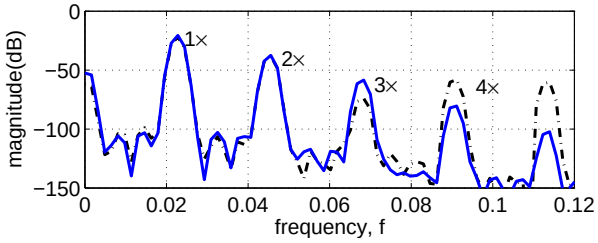

(b) Frequency spectrum.

Fig. 36. Comparison of the CFD results (dashed) and the NARMAX model response (solid) for $f = 0.0226$ (400Hz).

the two dominant harmonic-frequency components ($1\times$, $2\times$), but the errors at each peak increase for higher harmonic components. Increasing the maximum lags for input /output or adding the time delay will be helpful to improve the accuracy of the model. This issue will be discussed in Chapter V.

The same procedure is repeated for Re $= 1206\,(U_\infty = 15m/s)$, Re $= 1407\,(17.5m/s)$. The regressor terms are the same as those for Re $= 1608$ so as to examine how the variation of external flow conditions influences the model parameters and estimation error with the fixed model structure. Before the identification, the scale conversion is made on the simulation results for Re $= 1206, 1407$ to compare those with the data for Re $= 1608$ with respect to the same nondimensionalization scheme. The scaling formulae for the measured pressure output, y, and the jet velocity input, u, are given as follows.

$$p_c = p\left(U_\infty / U_{\infty,ref}\right)^2,\ v_c = v\left(U_\infty / U_{\infty,ref}\right), \tag{4.16}$$

Table III. Comparison of model coefficients for different free stream velocities.

Regressor(p_i)	$\hat{\theta}_i(\mathrm{Re}=1206)$	$\hat{\theta}_i(Re=1407)$	$\hat{\theta}_i(Re=1608)$
$p(k-1)$	1.695299	1.584948	1.481378
$p(k-2)$	-0.702646	-0.616763	-0.541882
$v(k-1)$	0.016703	0.044092	0.075060
$v(k-2)$	-0.019884	-0.051217	-0.088163
$p(k-2)^2$	2.376915	1.923612	1.462855
$p(k-1)v(k-1)$	-3.373990	-3.210335	-2.776820
$p(k-1)v(k-2)$	3.666473	3.551438	3.159657
NMSE	0.0803	0.0798	0.0706

where the subscript, $(\cdot)_c$, means converted variables and $U_{\infty,ref}$ is a reference velocity. In this study, $U_{\infty,ref} = 20m/s$ and $U_\infty = 15m/s, 17.5m/s$, respectively.

After conversion, the model parameters under different Reynolds numbers are presented in Table III. The error between the identified subset model and the numerical results is quantified with a normalized mean square error (NMSE) as

$$NMSE = \sqrt{\sum (\hat{y}(k) - y(k))^2 \Big/ \sum (y(k) - \bar{y}(k))^2}, \tag{4.17}$$

where $\hat{y}$ is a model output, y the estimation data and $\bar{y}$ the mean value of y. Each of the model coefficients changes monotonically as the free stream velocity increases, while the NMSE varies slightly. The physical behavior of the fluidic system is at least consistent within the range of given free stream velocities such that each parameter may be described as simple functions of free stream velocity.

The results show that if the external flow conditions such as free stream velocity are changed within a reasonably acceptable range, a model for synthetic jets can be described using NARMAX. The model has consistent regressor terms and a set of model parameters that represent the variation of external conditions.

CHAPTER V

CFD SIMULATION ON A ROUNDED BACKWARD FACING STEP

A. Overview

CFD simulation is performed at a rounded backward facing step, whose advantage is that it bears crucial geometric characteristics susceptible to flow separation in spite of its simple contour [61]. Therefore, the analysis performed for this geometry could be extended to other geometries associated with flow separation.

For this geometry, factors affecting the extent of flow separation are free stream velocity, viscosity and dimensions of the step. The geometric configuration will be fixed and the synthetic jet frequency is varied, taking into account the optimal range $0.5 \leq F^+ \leq 1.5$ of the reduced jet frequency in (1.1). Furthermore, with simulations under different free stream velocities, the effects of free stream velocity on flow separation and synthetic jet actuation are examined.

The results are implemented to build a flow model of synthetic jet actuation and design a feedback controller for flow separation in Chapter VI.

B. Boundary Conditions and Grid Distribution

Figure 37 presents the entire simulation domain including a rounded backward facing step. Based upon the nondimensionalization scheme in p. 51, the dimension of the step is given by 30×1.5, where the slope angle is 4.49° and a radius of curvature at the rounded edges is 139.015. The boundary conditions are set as shown in Table IV. The synthetic jet model

Table IV. Boundary conditions.

boundary	**AB**	**BC**	**CD**	**DA**
condition	zero Neumann	zero Neumann	wall (no slip)	Blasius velocity in (4.12)

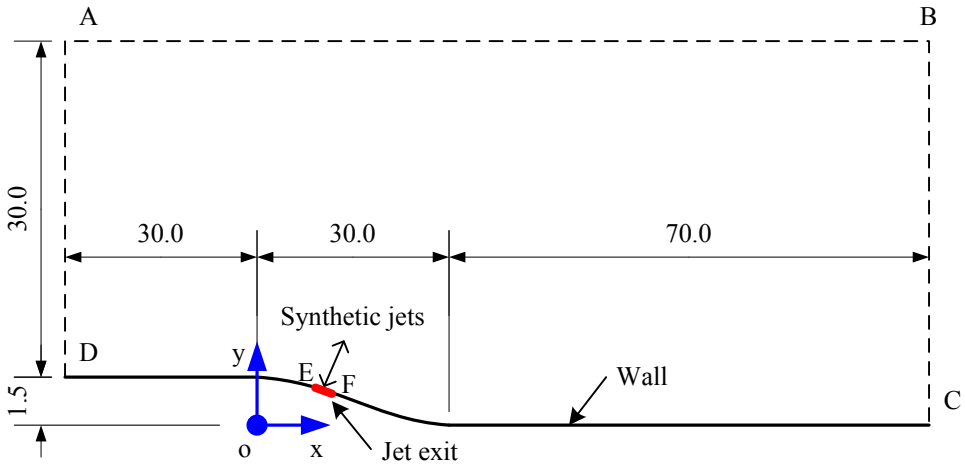

Fig. 37. Schematic diagram for CFD simulation (x and y axes are scaled differently).

in (4.2) is employed with a constant amplitude 2 m/s, which is nondimensionalized to 0.1 for $U_\infty = 20m/s$. The location **EF** for the jet actuation will be discussed in Section D.

The domain consists of 340 elements and the grids are organized to cluster with respect to the step. The grid distribution is presented in Fig. 38. The polynomial order of the spectral element is 12 and the time step for the simulation is 0.005.

C. Flow Separation in the Absence of Synthetic Jets

First, the flow is investigated in the absence of jet actuation as shown in Fig. 39. The reverse pressure gradient develops along the step and decreases as the flow is farther from the wall. The vorticity contours indicate that most of flow variation occur inside the boundary layer. As shown in Fig. 40, the separation bubble is formed along the downstream part of the step such that the streamlines are displaced away from the surface. Generally, the onset of flow separation can be detected by the point where the wall shear stress τ_w becomes

$$\tau_w = \mu \left. \frac{\partial u}{\partial y} \right|_{y=0} = 0.$$

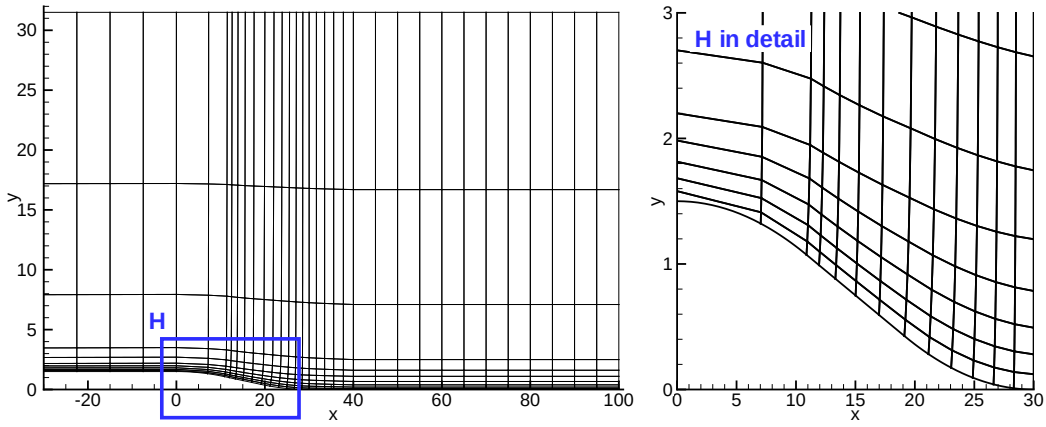

Fig. 38. Grid distribution (x and y axes are scaled differently).

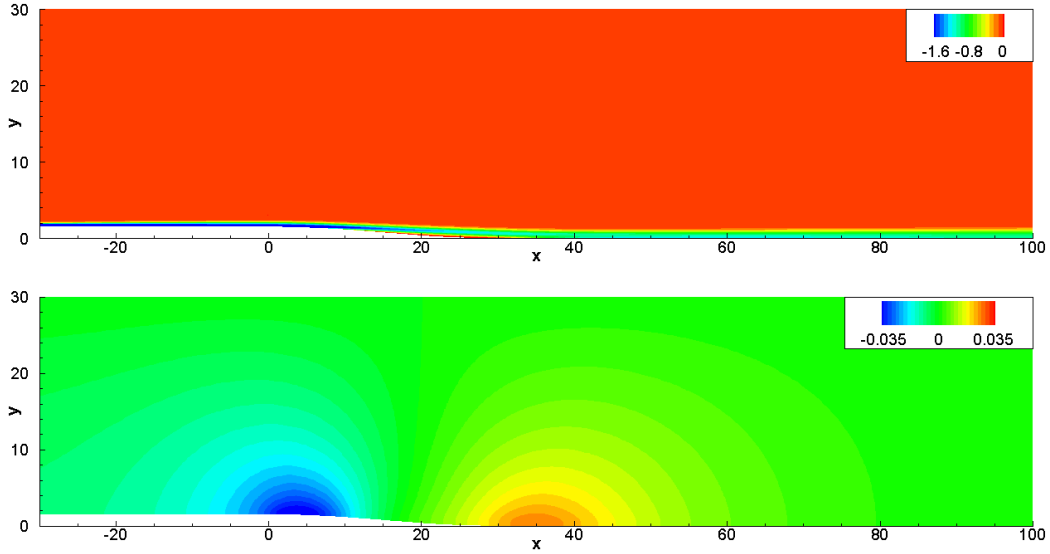

Fig. 39. Vorticity(top) and pressure(bottom) contour plots in the absence of jet actuation.

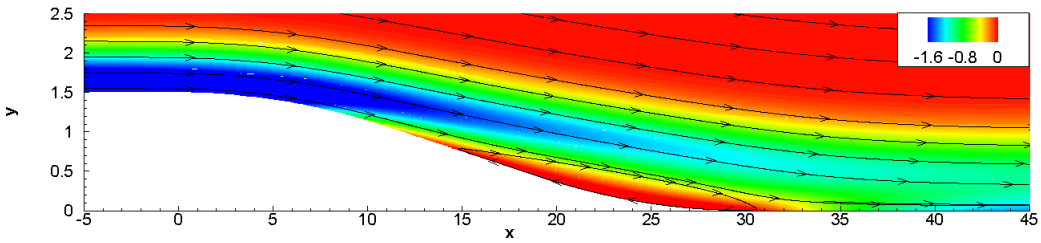

Fig. 40. Vorticity contour plot in the vicinity of the step.

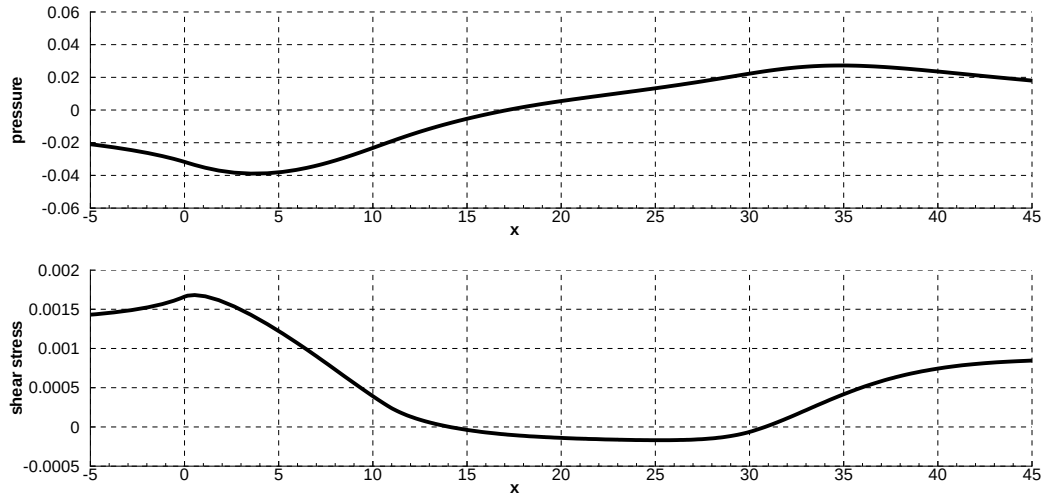

Fig. 41. Pressure (top) and shear stress (bottom) distributions along the wall in the absence of jet actuation.

According to this condition, the wall shear stress distribution in Fig. 41 indicates that the flow is separated at $x = 14$ and reattached at $x = 30.8$, which is in good agreement with the location of the separation bubble in Fig. 40. Consequently, the reverse pressure gradient is reduced after $x = 14$ as shown in the pressure distribution of Fig. 41.

D. Synthetic Jet Actuation

Regarding the placement of the synthetic jet actuation, the most effective location of a jet slot is empirically known to be slightly upstream from the separation point in the absence of jet actuation [35]. Therefore, the synthetic jet is assumed to oscillate at $\mathbf{EF} = \{\mathrm{E} = (10.885, 1.073), \mathrm{F} = (11.941, 0.990)\}$ in Fig. 37.

As the distance L from the jet slot to the flow-reattached point is $19.4\delta_o$ in Fig. 41, the relationship between physical and dimensionless frequencies is computed as shown in Table V. Physical frequency corresponding to $0.5 < F^+ < 1.5$ ranges from 460 to 1360 Hz in $U_\infty = 20m/s$. This range is covered in the simulation by varying the jet frequency from

Table V. Examples of conversion between different frequency scales for $U_\infty = 20m/s$.

frequency(Hz)	100	200	400	800	1200	1600
f for CFD	0.0057	0.0113	0.0226	0.0453	0.0679	0.0906
F^+	0.1098	0.2197	0.4393	0.8787	1.3180	1.7573

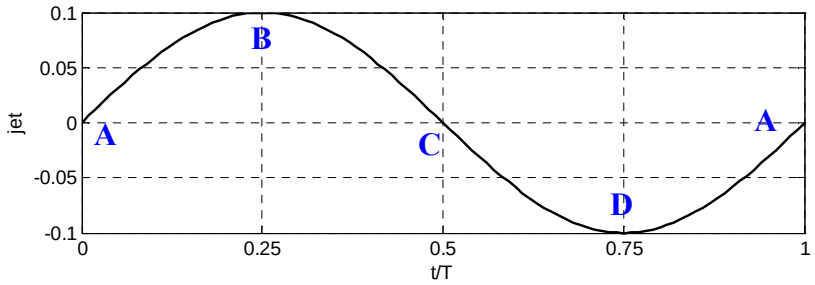

Fig. 42. One period of jet actuation.

100 Hz to 1600 Hz.

One period of jet actuation shown in Fig. 42 can be related with four cyclic stages of a synthetic jet actuator [15]: maximum volume of cavity (A), maximum propulsion (B), minimum volume of cavity (C) and maximum ingestion (D). Figures 43-47 present the vorticity contour plots at each operating stage of the actuator for the different synthetic jet frequencies $F^+ = 0.1098 \sim 1.7573$. At the low jet frequencies, F^+ =0.1098 and 0.2197, the smaller vortices are formed right behind the primary vortex and those are convected downstream as a group as shown in Figs. 43 and 44. The vorticity strength in the main vortex decreases gradually as it moves downstream. In contrast, as the jet frequency approaches $F^+ \simeq 1$, the minor vortices die out immediately and the vortices proceed downstream individually as shown in Figs. 45,46 and 47. In addition, the vorticity magnitudes of the main vortices are maintained more constantly than those of the main vortices of the lower jet frequencies. These counterclockwise vortices promote the mixing of the high momentum outside the edge of the boundary layer with the low momentum near the wall.

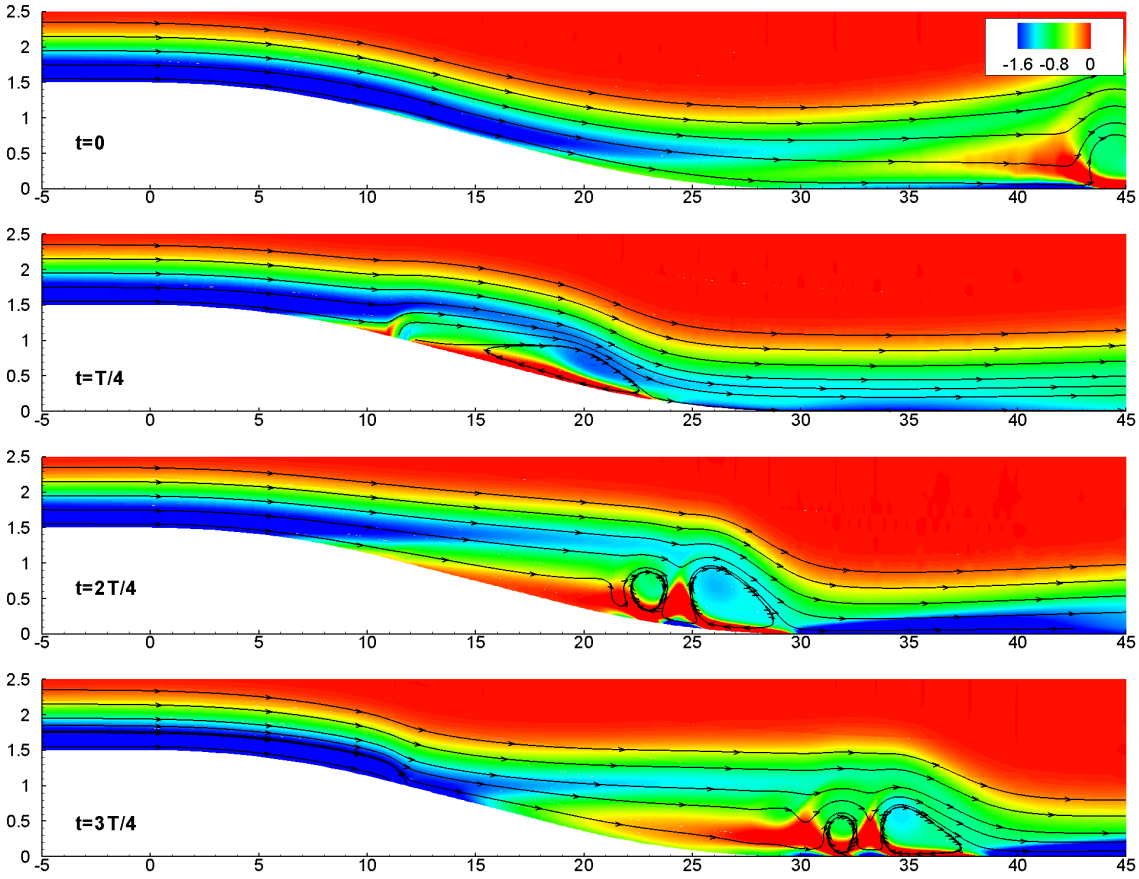

Fig. 43. Vorticity contour plots for the jet frequency $F^+ = 0.1098$ (100 Hz).

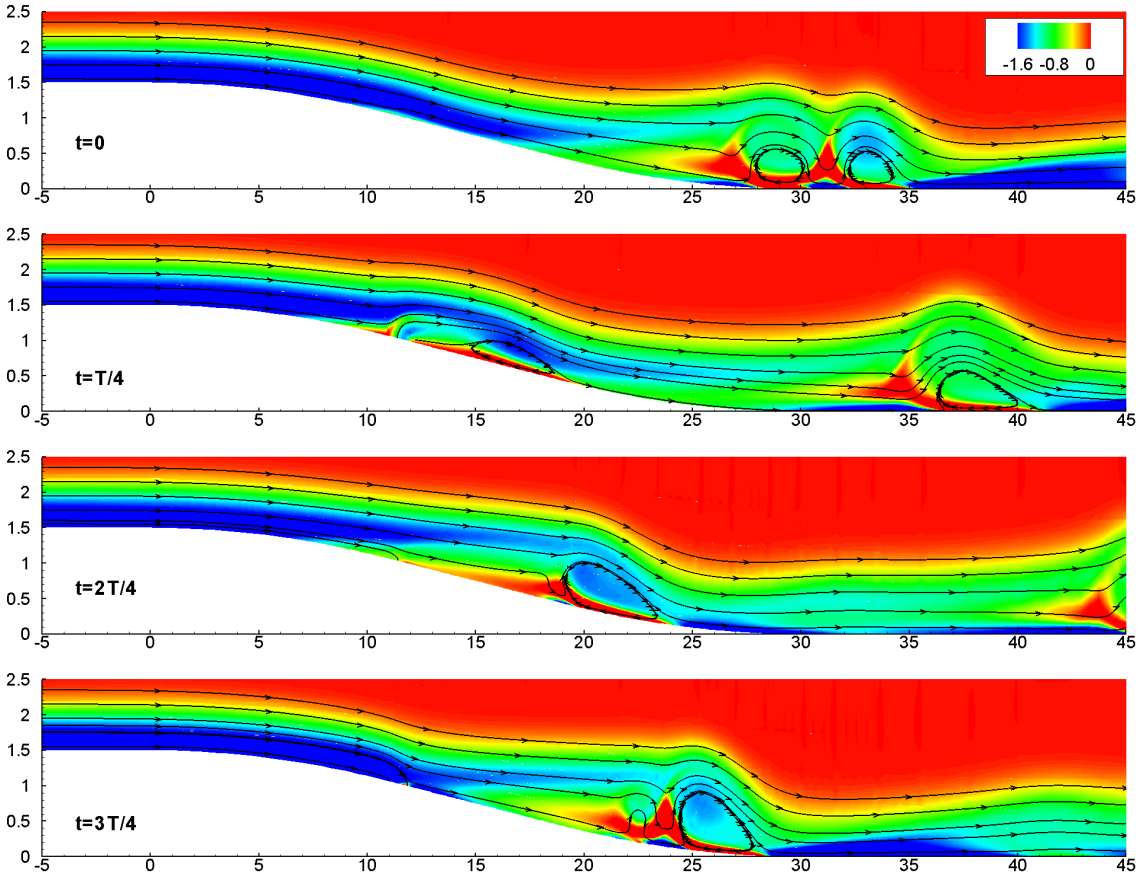

Fig. 44. Vorticity contour plots for the jet frequency $F^+ = 0.2197$ (200 Hz).

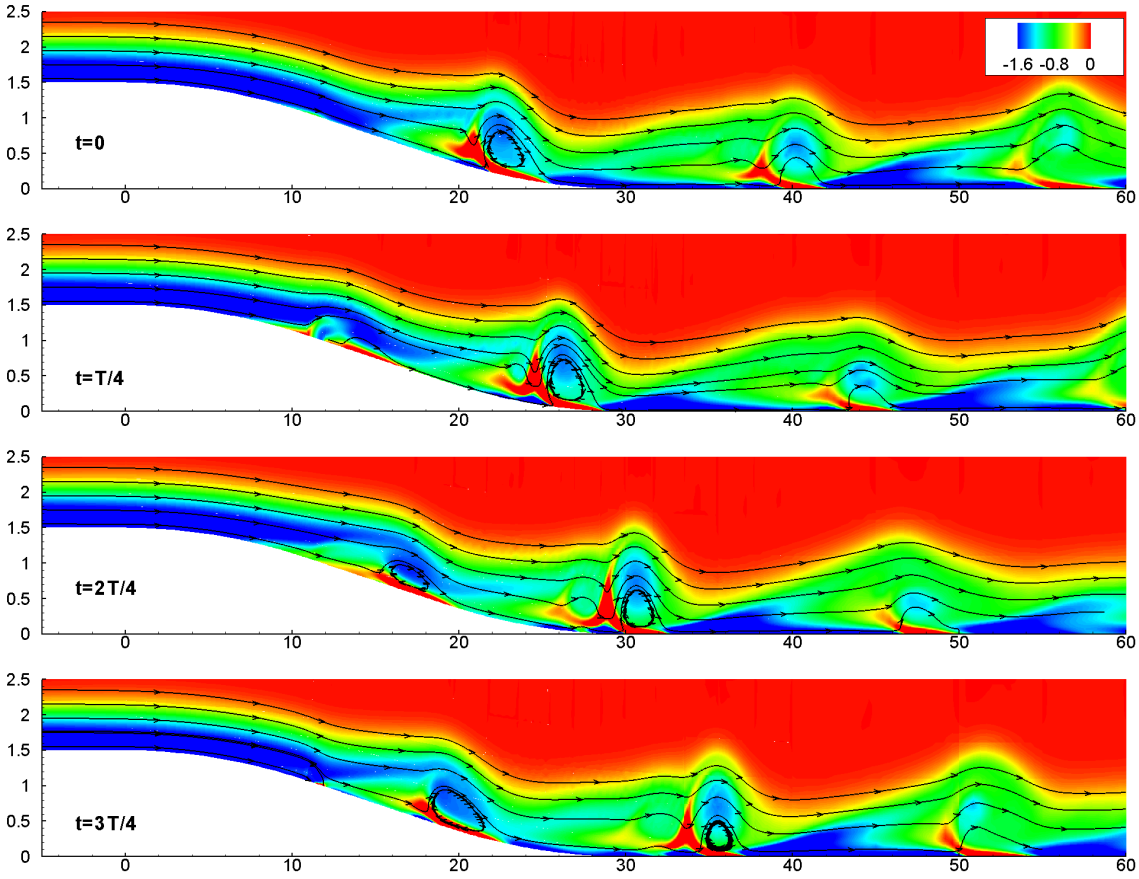

Fig. 45. Vorticity contour plots for the jet frequency $F^+ = 0.4393$ (400 Hz).

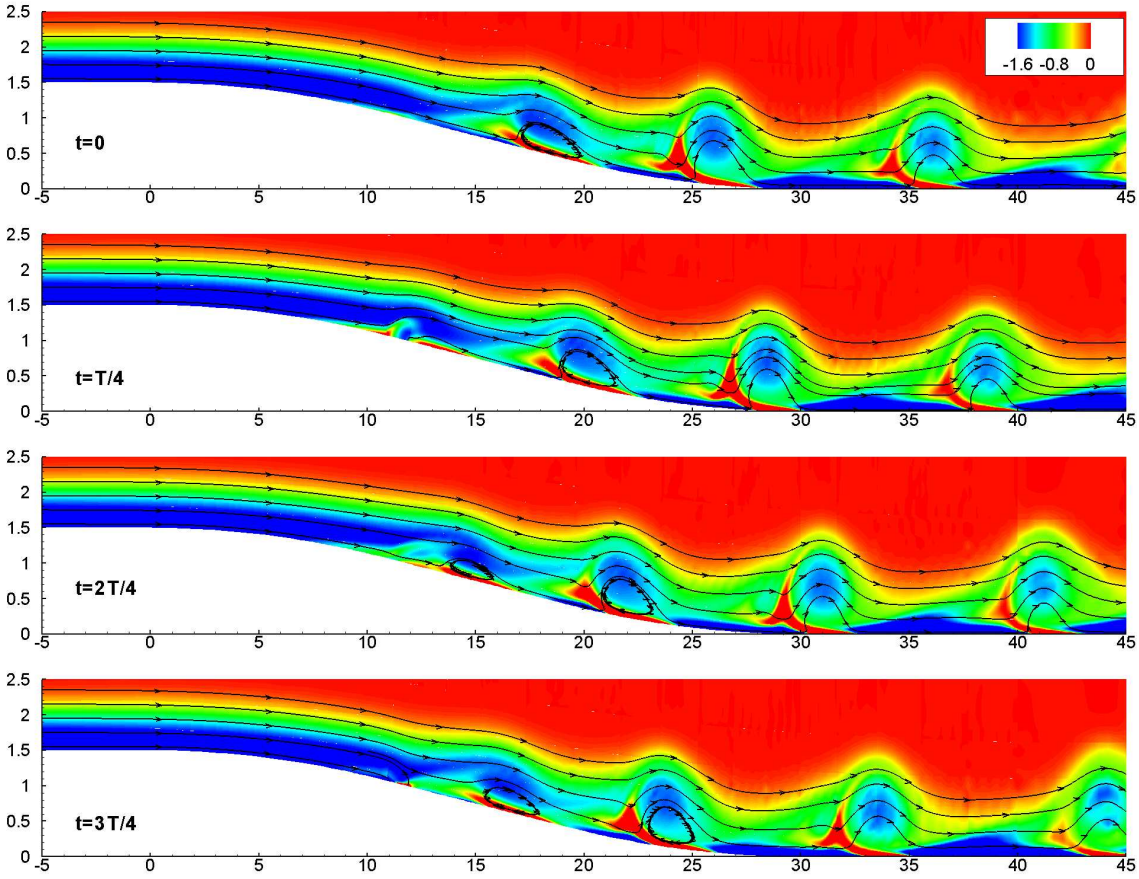

Fig. 46. Vorticity contour plots for the jet frequency $F^+ = 0.8787$ (800 Hz).

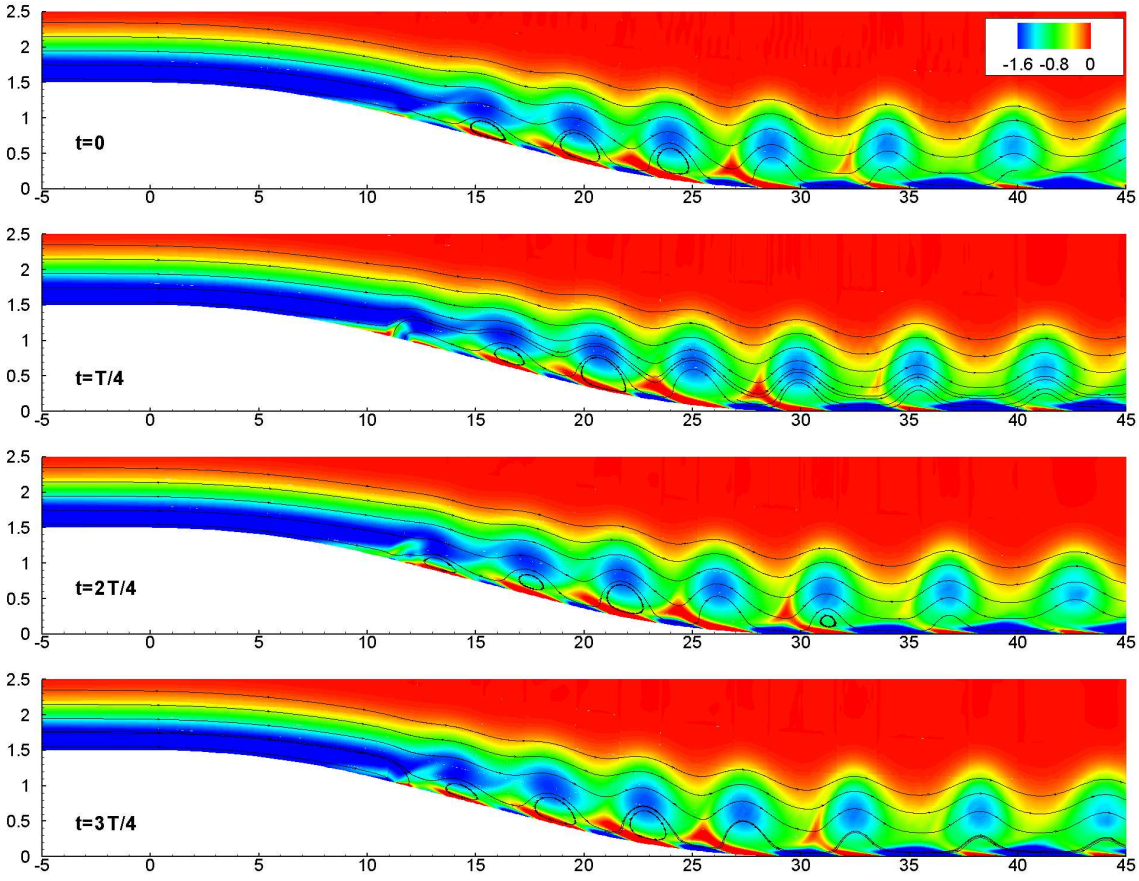

Fig. 47. Vorticity contour plots for the jet frequency $F^+ = 1.7573$ (1600 Hz).

As these vorticity plots are captured at the certain moments of unsteady flow, it is difficult to directly assess the effects of synthetic jets on flow separation. Alternatively, the mean flow properties are proposed to analyze the extent of flow separation. Compared to the flow in the absence of jet actuation in Fig.g 40, the mean vorticity contours in Fig. 48 show that synthetic jets eliminate the separation bubble successfully in terms of the mean value, even though the vorticity distribution near the slope is slightly altered depending on the jet frequency. As a result, the streamlines, which are distant from the wall in the absence of the jets, approach closer to the surface as shown in Fig. 49.

The effects of the jet frequency can be more clearly verified from the mean wall pressure and shear stress distributions in Fig 50. Note that the discontinuity in the plots indicates the jet exit slot. As the jet frequency increases in Fig. 50(a), the reverse pressure gradient is recovered more extensively and the separation region indicated by the negative shear stress is removed. However, as the jet frequency exceeds one in Fig. 51(b), the pressure gradient decreases again and thus the maximum downstream pressure also drops gradually. The wall shear stress is positive over the entire slope regardless of the pressure variation so that the flow is not separated. Form these results, the optimal jet frequency in terms of the maximum pressure recovery is inferred to be around $F^+ = 0.7 \sim 0.9$ under the given CFD conditions.

Integrating the pressure distribution on the step produces the resultant forces, F_x to the horizontal direction and F_y to the vertical direction acting on the step. In particular, F_x can be interpreted as a pressure drag applied on the step. As shown in Fig. 51, the jet actuation with $F^+ = 0.8787$ reduces the pressure drag by 26.7% and the vertical force F_y by 58.5%. As geometric features of a backward facing step is different from those of an airfoil, the synthetic jet actuation reduces the vertical force F_y acting on the step while it increases the lift force, i.e. the vertical force acting on the airfoil.

These results verify that there exists the narrow-frequency-band receptivity of the sep-

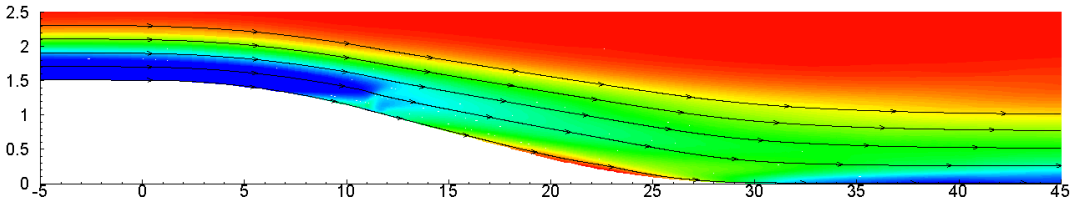

(a) $F^+ = 0.1098$.

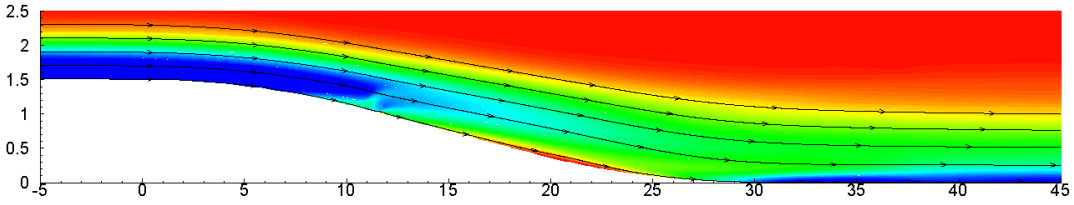

(b) $F^+ = 0.2197$.

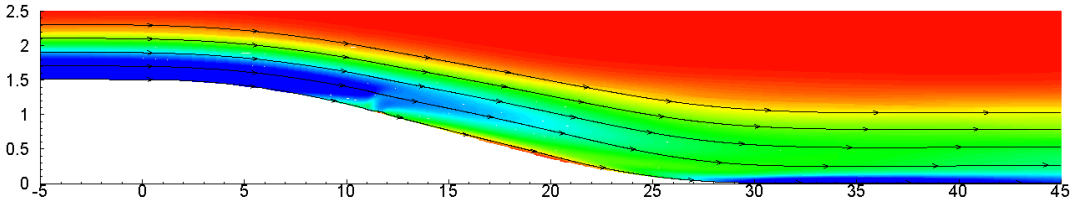

(c) $F^+ = 0.4393$.

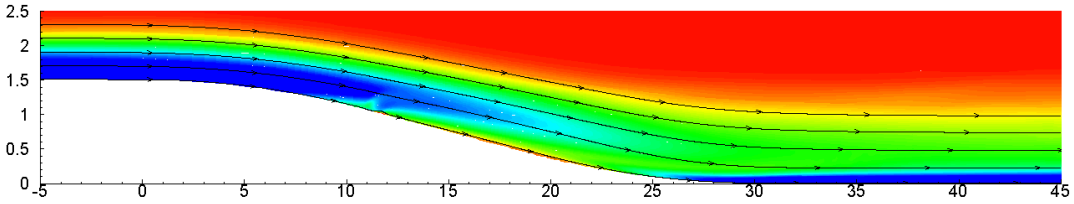

(d) $F^+ = 0.8787$.

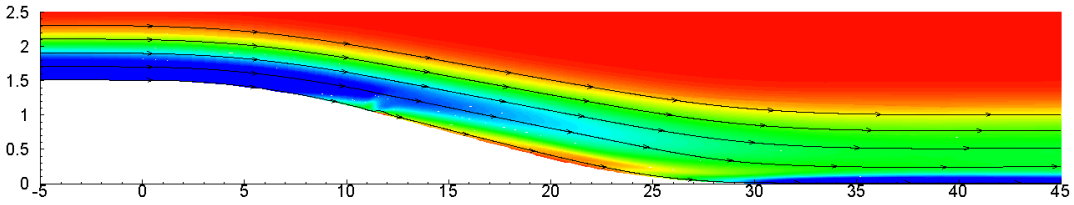

(e) $F^+ = 1.7573$.

Fig. 48. Mean vorticity contour plots for different jet frequencies (the lines denote streamlines).

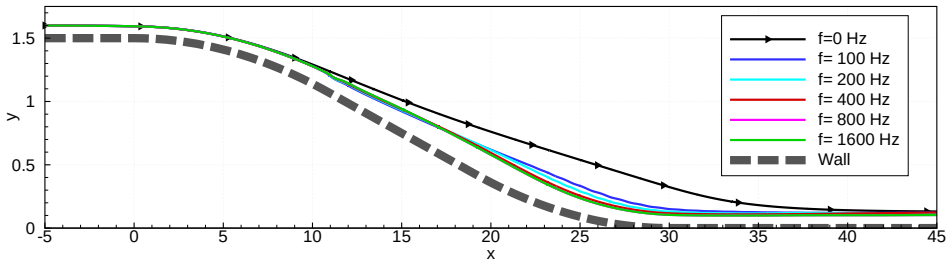

Fig. 49. Variation of streamlines starting at (0, 1.6) for different jet frequencies.

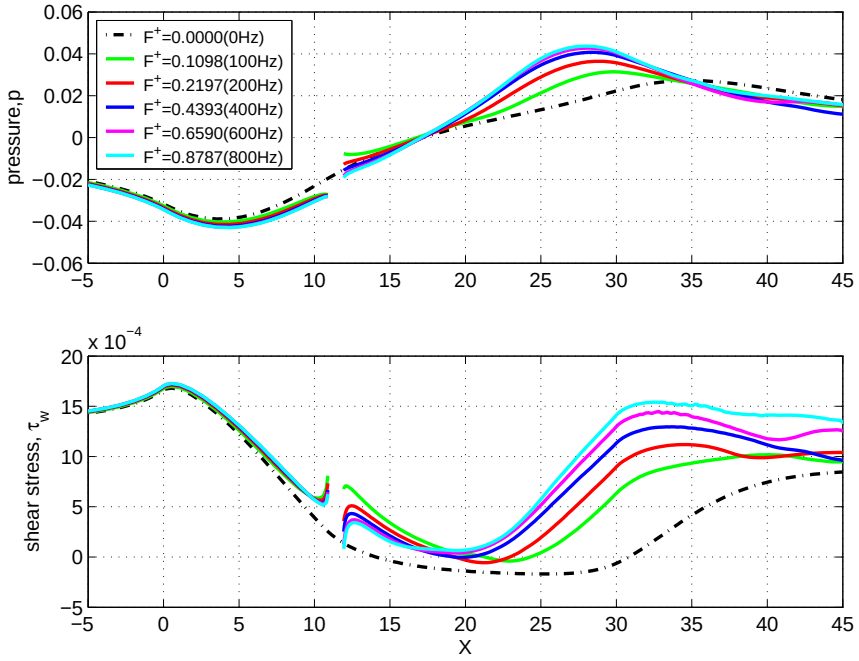

(a) $F^+ < 1$.

Fig. 50. Mean pressure (top) and shear stress (bottom) distribution along the wall for various jet frequencies.

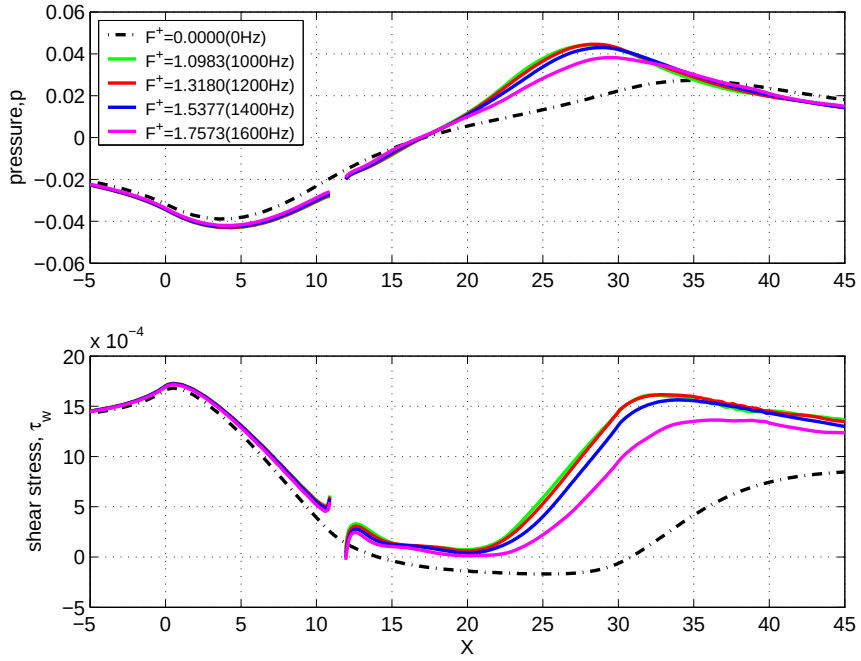

(b) $F^+ > 1$.

Fig. 50. Continued.

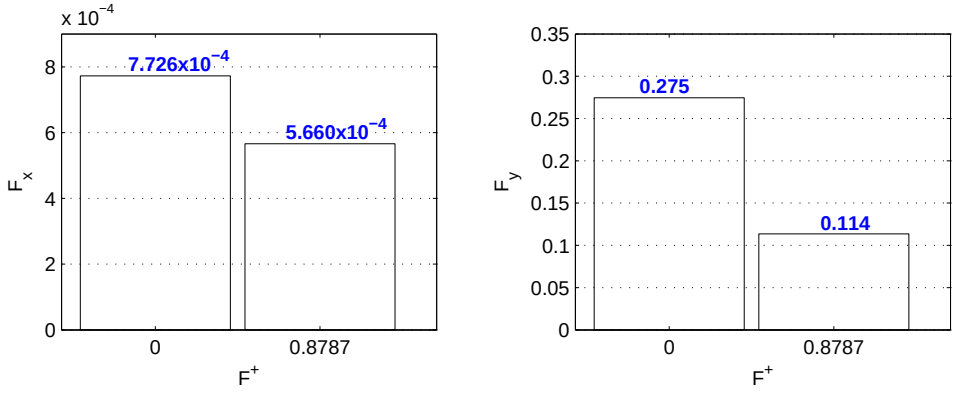

Fig. 51. Resultant forces F_x (left) and F_y (right) acting on the step for F^+ =0 and 0.8787 (800 Hz).

arating shear layer that match approximately the ratio of the free stream velocity to the streamwise length of the separating region [6]. The synthetic jet actuation with this frequency band can improve the mixing effects significantly and lead to achieve the maximum pressure recovery. Employing this unstable characteristics of separating shear layer facilitates the effective flow separation control by synthetic jet actuation at $0.5 < F^+ < 1.5$.

E. Effects of Free Stream Velocity

The free stream velocity is a key factor to affect the performance of synthetic jet actuation, since it determines the degree of flow separation on the domain. The velocity variation is assumed to be $\pm 10\%$ with respect to $U_\infty = 20 m/s$.

Figure 52 presents the baseline distributions of the wall pressure and shear stress in the absence of the actuation. As the Reynolds number increases, i.e. the free stream becomes faster, the separation region expands and the reverse pressure gradient deteriorates even though the variation is not massive within the given range of free stream velocity. The flow is reattached at (30.3, 0.0) for 18 m/s, (30.8, 0.0) for 20 m/s and (31.3, 0.0) for 22 m/s.

Although the jet amplitude is assumed to be constant as 2 m/s, the jet momentum coefficient, C_μ, in (1.3) varies due to the varying free stream velocity. C_μ is 7.838×10^{-4} for 18 m/s, 6.185×10^{-4} for 20 m/s and 4.983×10^{-4} for 22m/s. Therefore, the strength of the jets decreases relatively as the free stream becomes faster.

Figure 53 shows the variation of the mean wall pressure at a certain downstream point (19.12, 0.43) with respect to the jet frequency, combining the effect of the free stream velocity. Regardless of free stream velocity, the maximum pressure recovery is achieved consistently at $F^+ \simeq 0.8$ that corresponds to 673 Hz for 18 m/s, 728 Hz for 20 m/s and 781 Hz for 22 m/s respectively. Therefore, concerning the pressure recovery, the optimal frequency of the jet actuation on a dimensional scale should be increased proportionally to

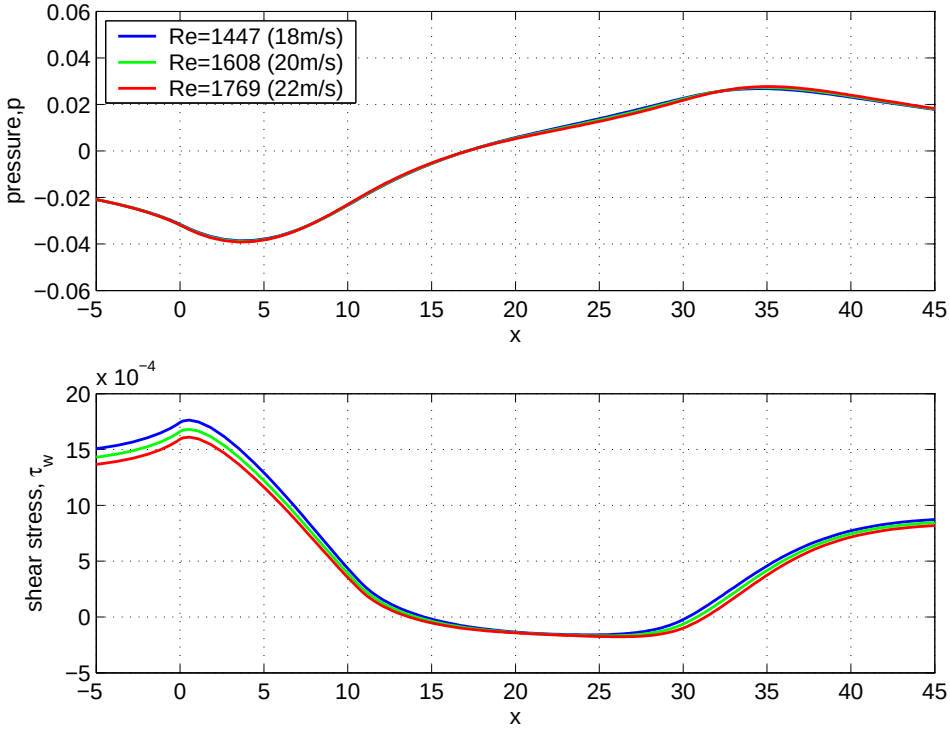

Fig. 52. Mean wall pressure (top) and shear stress distributions for varying free stream velocities without actuation.

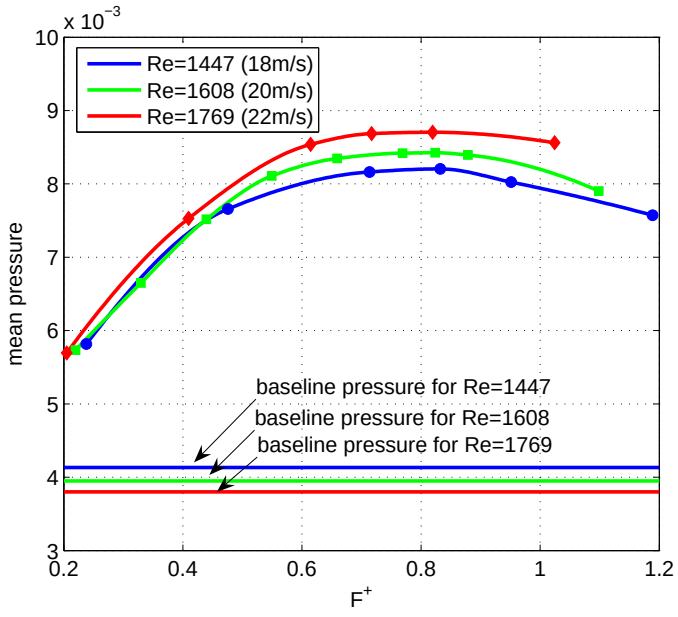

Fig. 53. Variation of the mean wall pressure to the jet frequency at (19.12, 0.43)

the free stream velocity. The differences between each plot broaden as the jet frequency increases, whereas the overall characteristics are not changed despite different free stream velocities. This consistency is beneficial to a feedback control synthesis, since it implies that regarding a flow model, the effects of free stream velocity varying within a certain range can be incorporated into model coefficients, with the model structure retained.

CHAPTER VI

FEEDBACK CONTROL OF FLOW SEPARATION

A. Overview

Given the rounded backward facing step as shown in Fig. 54, a feedback control system for flow separation is developed. The control objective is to maintain the maximum mean wall pressure at B by synthetic jets despite the variation of free stream velocity. The controller commands the synthetic jet frequency to the actuator at A and the downstream pressure at B is utilized as a feedback signal for the controller. Low-pass filtering the feedback pressure separates the quasi-linear response (including DC component) of the pressure signal from the higher harmonic frequency components. The mean wall pressure of the control objective is replaced with the filtered quasi-linear response, since the quasi-linear component of the periodic signal is identical to its mean value. The fact that the filtered pressure response for the synthetic jet frequency shows quasi-linear characteristics facilitates control system design using linear theory.

Regarding the effect of the varying free stream velocity on the flow, It is proposed that the reference pressure command can be adjusted using a lookup table for the maximum average pressure corresponding to the free stream velocity.

B. Nomenclature

e Error, $r - p$.

p Wall pressure at downstream point B.

p_0 =0.003949, Baseline wall pressure at downstream point B at $U = 20m/s$.

p_{lp} Low-pass filtered response of p.

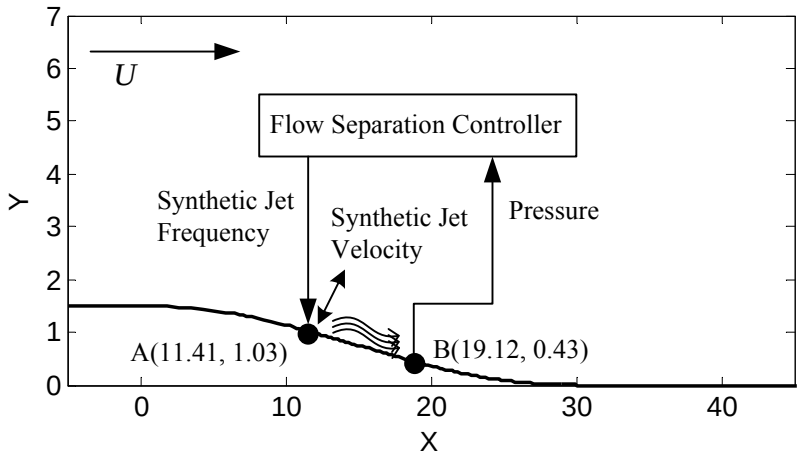

Fig. 54. Schematic diagram for the flow separation control.

$\bar{p}$ Mean wall pressure at downstream point B.

r Reference command for the pressure.

u Controller output.

v Actuator output (synthetic jet velocity).

A Amplitude of the synthetic jets.

$G_c(z)$ Feedback controller.

$G_{lp}(z)$ Low-pass filter.

$G_p(z)$ Linearized plant model.

K_P Proportional gain.

K_I Integral gain.

U Free stream velocity.

T Sampling time.

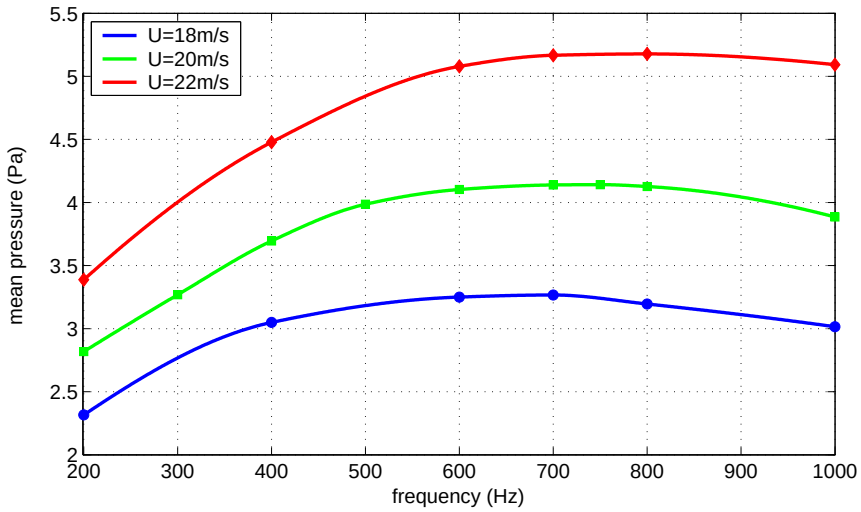

Fig. 55. Variation of the mean wall pressure to the jet frequency at (19.12, 0.43) on a dimensional scale.

f_u Frequency of the controller output u.

f_j Frequency of actuator output v (synthetic jet frequency).

F^+ Reduced synthetic jet frequency.

ω_u Angular frequency of control output, u, $= 2\pi f_u$.

Ω Angular frequency of the synthetic jets, $= 2\pi f_j$.

Note that the analysis in this chapter is performed based upon the dimensionless scale defined in Chapter IV. The conversion table for the different frequency scales such as f_j, f_u and F^+ were shown previously in Table V.

C. Control Objectives and Proposed Approaches

Figure 55, the conversion of Fig. 53 into the dimensional variables, presents the relationship between the jet frequency and the mean pressure for different free stream velocities. It confirms that the free stream velocity is a key parameter affecting the synthetic jet actuation

in case the surface contour is fixed. Therefore, the fluidic system with synthetic jets can be described as

$$p(t) = f(u(t), U), \tag{6.1}$$

where p is the wall pressure, u the synthetic jet frequency and U the free stream velocity. The feedback controller aims to achieve the maximum mean pressure while accommodating the effects of the varying free stream velocity. Therefore, the mean value of p in (6.1), $\bar{p}$, becomes the interesting control variable for this research. To facilitate an initial design of control system, the flow and actuator dynamics are assumed to be much faster than the variation of U such that U will not be involved in the dynamics of the flow model but incorporated as the parameter uncertainty of the model.

The controller design considering free stream effects includes two steps:

- The first step is to design the feedback controller for the nominal plant at $U = 20$ m/s. The nominal system is analyzed to decide the performance specification and stability so that a suitable control may be implemented for the plant.

- In the second step, the uncertain set of the plant in (6.1) is defined from the discrete values of the free stream velocity in a given range and a lookup table relating the maximum pressure and discrete free stream velocity is implemented for the reference pressure. Using the lookup table and the uncertainty set of the flow model, the controller is designed to overcome the variation of the free stream.

Figure 56 presents the proposed feedback control loop for flow separation. Using the lookup table, the reference pressure command is altered depending on the free stream velocity. The controller attempts to minimize the difference between the reference and feedback mean pressure. In this research, only the nominal plant at $U = 20$ m/s is considered for the controller design. The controller design using the lookup table scheme is left

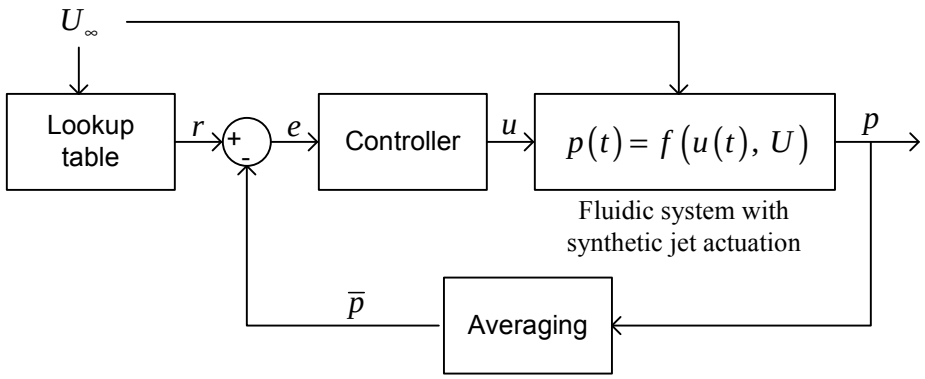

Fig. 56. Overall feedback control loop.

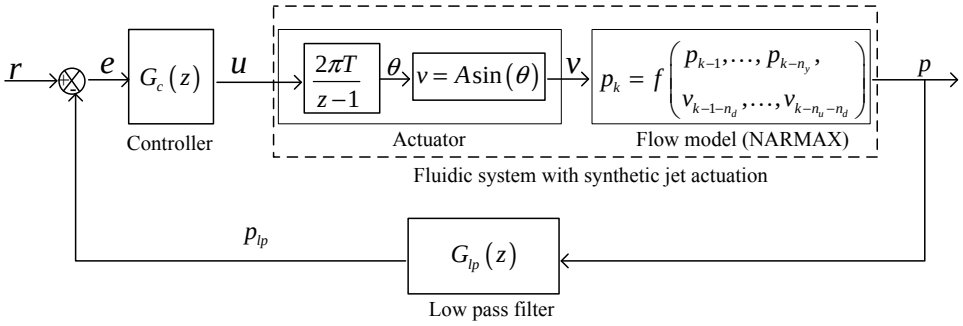

Fig. 57. Feedback control loop for the nominal plant in discrete time domain.

as a future work. The time scale issues regarding the varying free stream velocity are also discussed in Section K.

The closed control loop disregarding the effects of the free stream velocity is given in Fig. 57. The entire system is converted into the discrete time domain with a sampling time T. The actuator is assumed to respond instantly with respect to the controller output such that it is modeled as a simple block of the integrator and sinusoid. The nonlinear model using NARMAX system identification is implemented to relate the pressure output with the oscillating synthetic jet velocity. Compared with Fig. 56, low-pass filtering replaces averaging, since its transient response is faster than averaging, keeping the equivalent role

of averaging. This issue will be discussed in Section G.

The operating mechanism of this control loop is as follows. With low-pass filtering, the filtered pressure, which primarily contains the DC component, is utilized as a feedback signal. The DC component stands for a signal component at the zero frequency of the output signal. According to the error between the aimed maximum pressure recovery and the filtered pressure, the controller generates the synthetic jet frequency as a control output, which is transferred to the actuator. It exposes the uniqueness of the proposed control system. Conventionally, the controller signal acts as velocity, force or torque on the system, whereas the controller in this loop provides the frequency of the jet velocity to the actuator. This characteristic causes a strong nonlinear behavior of the system. In what follows, it will be shown that the low-pass filter can reduce the nonlinearity considerably in terms of the input-output relationship such that it facilitates controller design based upon linear theory.

D. Location of Pressure Measurement

As the pressure acquired at somewhere downstream from the jet actuation will be employed as a feedback signal to the controller, the optimal location for the pressure acquisition is crucial. Key criterions are hypothesized as:

- The measuring point should be as close to the exit slot as possible to minimize the time delay of the pressure response to the jet excitation.
- The pressure sensitivity at the measuring point should be large enough to represent the effects of the jet frequency on the wall pressure distribution.

As shown in Fig. 50, if the pressure is measured too close from the exit slot, the pressure sensitivity for the jet frequency is too weak to capture the effects of the jet frequency. On the other hand, if it is measured far from the exit slot to enhance the pressure sensitivity,

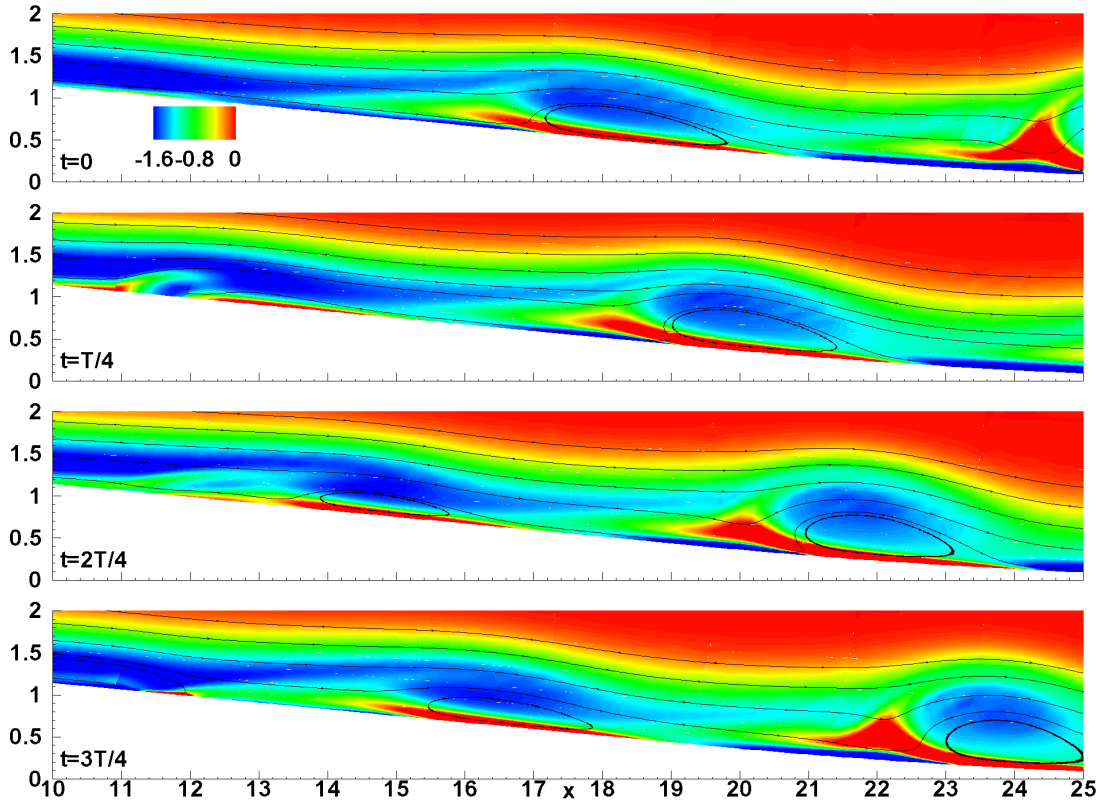

Fig. 58. Vorticity contours for one cycle of the synthetic jet with $F^+ = 0.8787$ (800Hz).

the increasing time delay between the jet actuation and pressure response at the measuring point will have negative effects on the controller design.

Investigating the vicinity of the jet slot, where the interaction of a synthetic jet with a cross flow originates, proposes the basic idea to decide the measuring point. As shown in Fig. 58, the vorticity contours at $F^+ = 0.8787$ are chosen for the investigation, since the interesting frequency band is approximately $F^{\sim}0.8$ for the maximum pressure recovery. Note that the jet slot is located at $x = 10 \sim 11.9$ along the slope. The jets reach the maximum blowing at $t = T/4$ and the maximum suction at $t = 3T/4$. After one period of the actuation is completed, the fully developed vortex reaches at $x = 18 \sim 20$, beyond which it convects downstream close to the wall, maintaining the coherent structure. Once the vorticity is completely developed at the particular region, the wall pressure responses

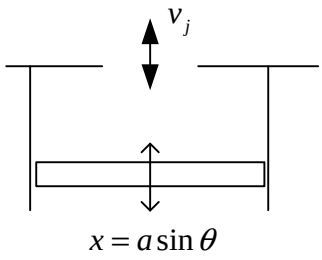

Fig. 59. Simple synthetic jet actuator model.

measured beyond that region will have the identical characteristics.

Therefore, the surface on $x = 18 \sim 20$ are the closest distance from the jet slot where the characteristics of the fully grown vorticity can be captured. This range would vary depending on several factors such as jet frequency, jet magnitude and free stream velocity. The uncertainty caused by these factors can be compensated by the system modeling and controller design. From this observation, the measuring point is located at approximately (x, y)=(19.12, 0.43) on the surface. Figure 55 verifies that the pressure variation at this point shows the sufficient sensitivity representing the effects of synthetic jets on the entire domain.

E. Actuator Model

In this section, the assumptions made for the actuator model in (4.2) are examined from a control perspective.

Suppose that the actuator is driven by a rotating machine such as a motor. First, if the motor dynamics immediately responds an electrical input signal from a controller, the transfer function coupling the controller and the actuator becomes a constant gain, which is assumed one in this model. Secondly, as shown in Fig. 59, the displacement x of the moving surface is assumed as a simple sinusoidal function of the angular displacement θ of the motor as follows.

$$x = a\sin(\theta). \tag{6.2}$$

The time derivative of (6.2) produces the velocity of the moving boundary as

$$\dot{x} = a\Omega_j \cos(\theta), \tag{6.3}$$

where the instantaneous angular frequency $\Omega_j = d\theta/dt$. The velocity amplitude in (6.3) increases proportionally to Ω_j.

Assuming that the jet velocity has the same sinusoidal characteristic as the moving boundary, the jet velocity at the center of the exit slot can be expressed as

$$v = A\sin(\theta), \tag{6.4}$$

where the jet amplitude, A, is constant. It can be rewritten in terms of the jet frequency as

$$v = A\sin\left(\int_0^t 2\pi f_j(\tau)d\tau\right). \tag{6.5}$$

This model has a limitation. If the actuation stops at $t = t_s$, the real actuator does not produce the jet any more, whereas the model in (6.5) will blow out the constant jet $A\sin(theta_s)$ for $t > t_s$. Therefore, this approximate model is valid only if the actuator operates within a certain range of the jet frequency, $f_j(t) > 0$, at all times.

The discrete form of (6.5) with a sampling time T is

$$\begin{aligned} \theta(k+1) &= \theta(k) + 2\pi T \cdot u(k), \\ v(k) &= A\sin\theta(k), \end{aligned} \tag{6.6}$$

where the controller output u replaces the notation of f_j, since both of them are equivalent. Figure 60 shows the Simulink® diagram of (6.6).

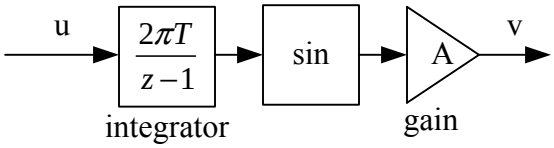

Fig. 60. Simulink® diagram for the actuator model.

1. Frequency Modulation by Actuator

In general, the jet frequency $u(t)$ can be expressed as

$$u(t) = f_j(t) = f_c + f_m(t), \tag{6.7}$$

where f_c is the DC term and $f_m(t)$ is the fluctuation term. In this research, the jet frequency $u(t)$ is ranged from $f_{\min}$ to $f_{\max}$. This assumption is discussed in more detail and implemented as a saturation in Section J. Based on this frequency range, $u(t)$ can be rewritten as

$$\begin{aligned} &u(t) = f_j(t) = f_c + \Delta f \cdot x_m(t), \\ &\text{where } f_c = \frac{f_{\max} + f_{\min}}{2},\ \Delta f = \frac{f_{\max} - f_{\min}}{2},\ |x_m(t)| < 1. \end{aligned} \tag{6.8}$$

Subsequently, the jet velocity in (6.5) becomes

$$v = A\sin\left(2\pi \int_0^t [f_c + \Delta f \cdot x_m(\tau)] d\tau\right). \tag{6.9}$$

The frequency modulation effect is shown in this equation, where f_c stands for the carrier frequency and Δf is the frequency deviation representing the maximum shift away from f_c in one direction. It carries the signal information in $x_m(t)$.

Supposing that $x_m(t) = \sin(2\pi f_u t)$ is chosen in (6.8), the resultant jet velocity can be expressed as

$$v = A\sin\left[2\pi f_c t - \frac{\Delta f}{f_u}\cos(2\pi f_u t)\right]. \tag{6.10}$$

Figure 61 shows the frequency modulation of the actuator for the case of $A = 0.1$, f_c =0.0325 (573.5 Hz), Δf =0.0098 (173.5 Hz) and f_u =0.0027 (48 Hz) for (6.10). Given the DC

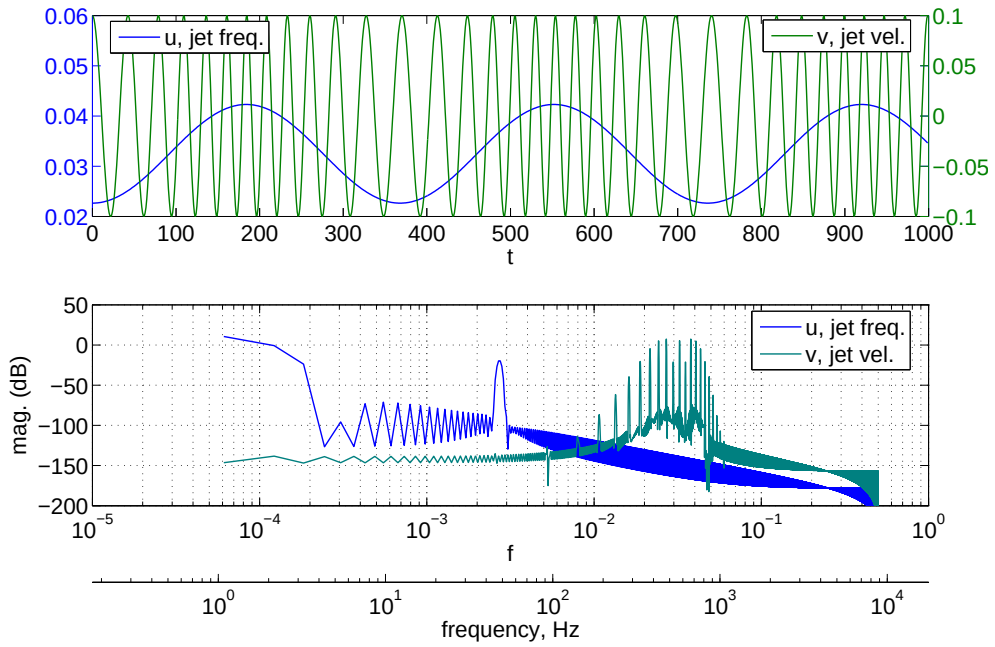

Fig. 61. Relationship between the jet frequency input, u, and the jet velocity, v, for f_c =0.0325 (573.5 Hz), Δf =0.0098 (173.5 Hz) and f_u =0.0027 (48 Hz).

component, f_c, and input frequency component at f_u in the input $u(t)$, the frequency components of the velocity are limited inside $f_c \pm \Delta f$, although some negligible components are scattered outside the bounds.

F. Flow Model

1. Characteristics of Flow System

Figure 62 presents the pressure response at (19.12, 0.43) with respect to the jet velocity input in Fig. 61. The flow system creates dominant frequency components at the carrier frequency band and higher harmonics, while it demodulates nonlinearly the frequency components of the input frequency band corresponding to $u(t) = f_c + \Delta f \sin(2\pi f_u t)$. As the system response in the input frequency band is critical to control system design, the system identification is performed in that frequency band.

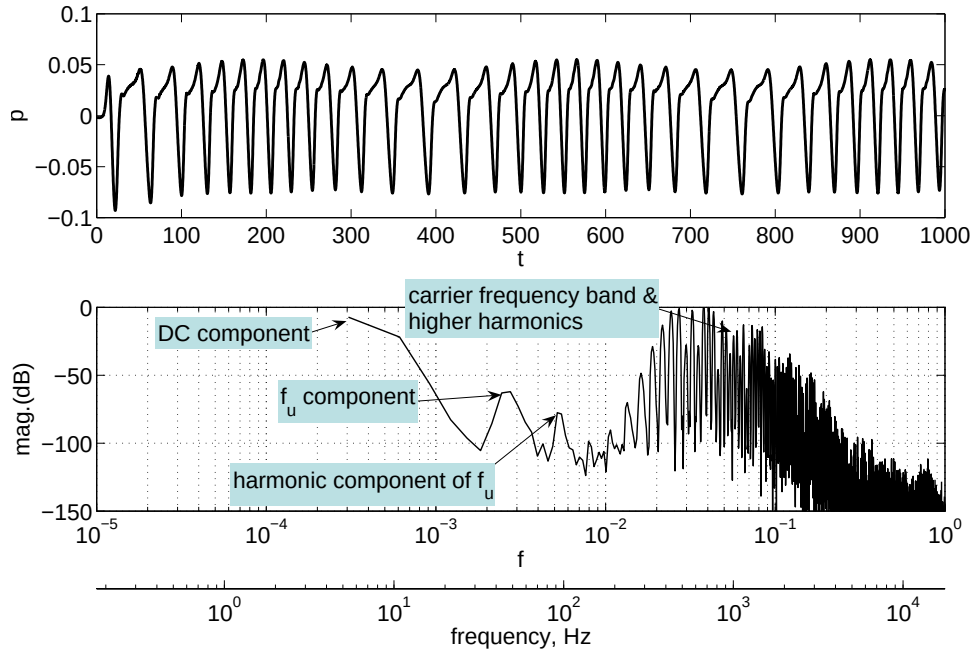

Fig. 62. Pressure response at (19.12, 0.43) for the jet velocity input shown in Fig. 61.

2. Input Design for System Identification

In order to identify the system coupling the jet frequency input $u(t)$ to the jet velocity output $v(t)$, a chirp signal can be implemented for $u(t)$ as follows:

$$f_u(t) = f_{u1} + \frac{f_{u2} - f_{u1}}{M} t, \text{ for } 0 \le t \le M, \tag{6.11}$$

$$\begin{aligned} u(t) &= f_c + \Delta f \cdot \sin\left(\int_0^t f_u(\tau) d\tau \right), \\ &= f_c + \Delta f \cdot \sin\left(2\pi \left[f_{u1} t + \frac{f_{u2} - f_{u1}}{2M} t^2 \right] \right), \end{aligned} \tag{6.12}$$

where the instantaneous frequency $f_u(t)$ of $u(t)$ increases from f_{u1} to f_{u2} over a time period M. Subsequently, the jet velocity in (6.9) can be reformulated as

$$v = A \sin\left(2\pi \int_0^t \left[f_c + \Delta f \cdot \sin(f_{u1}\tau + \frac{f_{u2} - f_{u1}}{2M} \tau^2) \right] d\tau \right), \text{ for } 0 < t, M. \tag{6.13}$$

As shown in Fig. 55, the maximum pressure recovery at $U = 20 m/s$ is achieved around

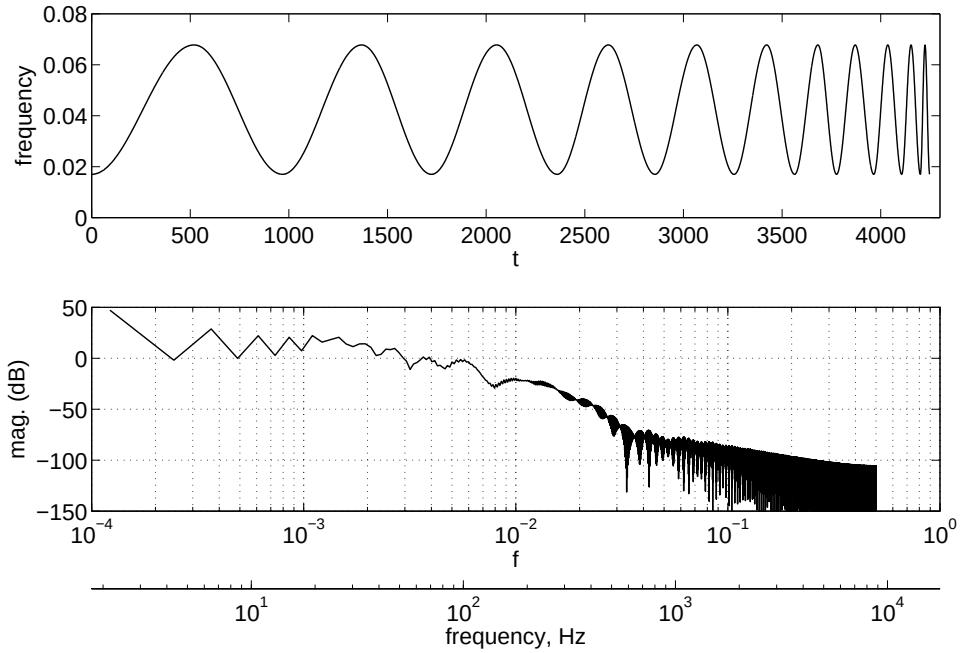

Fig. 63. Jet frequency as an input data for the identification. Upper plot: Time domain, Lower plot: Frequency spectrum.

a jet frequency 0.0396 (700 Hz). Accordingly, f_c and Δf in (6.13) are set by 0.0425 (750 Hz) and 0.0255 (450 Hz), respectively to include this frequency. Regarding the feedback control loop, the stop frequency of the low-pass filter will be located below the lower frequency bound of the carrier frequency band, which is 0.0226 (400 Hz) in Section J, to filter out the carrier frequency band. Therefore, the bandwidth of the feedback controller will be lower than the filter stop frequency and thus 0.0226 (400 Hz) would be sufficient as a maximum value of f_{u2} for the chirp signal.

Unfortunately, the formulation in (6.13) is not supported by the CFD code utilized in this research at the moment. Alternatively, f_u is designed to increase discretely every half a period from $f_{u1} = 0.00096$ (17.5 Hz) up to $f_{u2} = 0.0212$ (374 Hz) as shown in Fig. 63. Given the jet frequency input, the actuator creates the jet velocity shown in Fig. 64, which is implemented in the CFD simulation for the system identification.

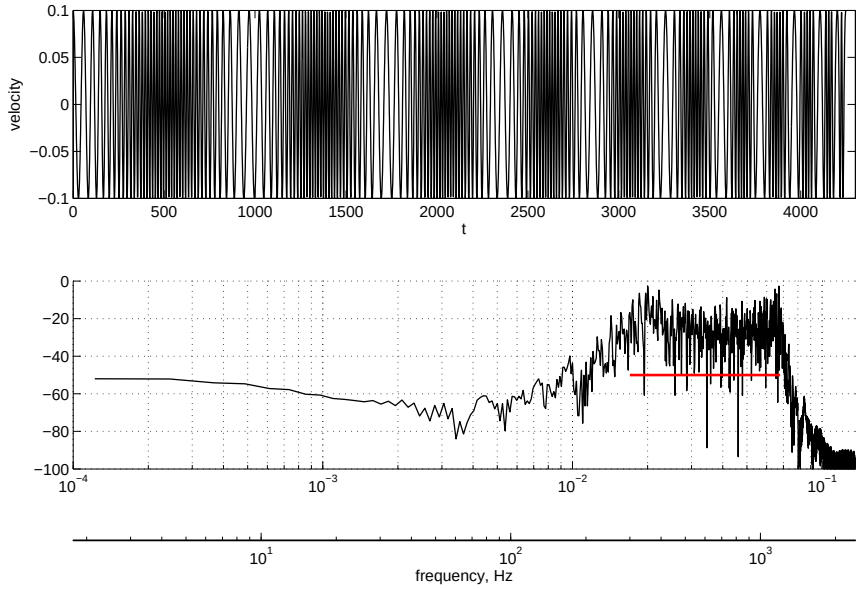

Fig. 64. Jet velocity used in the CFD simulation for the identification. Upper plot: Time domain. Lower plot: Frequency spectrum. The red line indicates the frequency range $f_c \pm \Delta f$.

3. System Identification

The NARMAX method is employed to identify the nonlinear flow model excited by synthetic jets.

Regarding the model structure, there exist several factors to determine the structure: sampling time, order of nonlinearity, maximum time lag for output p, maximum time lag for input v and input time delays. Unfortunately, there are no general rules to determine those factors. It is demanding to optimize the model by examining all these factors simultaneously. Therefore, some of the factors are assumed to have certain values and the rest of them are chosen by comparing the errors that each factor causes. The assumptions made regarding the model structures are:

- Only second-order nonlinearity for polynomials is considered. It is the minimum nonlinearity and is sufficient to approximate numerous dynamic systems.
- The pressure response is assumed to have second-order dynamics so that the maximum time lag for p is given by $p(k-2)$.
- The time delays should be included in the input terms. As the distance from the exit slot at (11.4, 1.03) to the measuring point at (19.12, 0.43) is 7.74, it will take $t = 7.74$ for the free stream to travel that distance. Note that the dimensionless free stream velocity is one. Therefore, the input delays can be assumed to be the integer value near $7.74/T$ after the sampling time T is chosen.

The sampling time is a crucial variable to convert a continuous system into a discrete NARMAX model. To avoid the aliasing effect and improve the accuracy of the estimation, it is desirable to choose a high sampling frequency. However, if the sampling frequency is extremely high, the regression matrix in the identification procedure may become ill-conditioned and significant nonlinear terms can get neglected [65]. Considering the maxi-

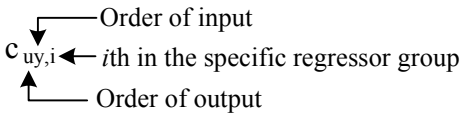

Fig. 65. Notation for the model coefficients.

Table VI. First-order regressors and corresponding coefficients.

$v(k-n_{10,i})$	$c_{10,i}$	eRR	$\hat{p}(k-n_{01,i})$	$c_{01,i}$	eRR
$v(k-10)$	-4.82405	1.491e-005	$\hat{p}(k-1)$	1.40303	8.740e-001
$v(k-11)$	18.23427	1.772e-003	$\hat{p}(k-2)$	-0.53417	1.145e-001
$v(k-12)$	-26.48305	7.962e-005			
$v(k-13)$	17.73475	8.002e-005			
$v(k-14)$	-4.70585	6.759e-004			

mum input lag, it should be minimized because increasing the maximum lag escalates the complexity of the model. These two variables are chosen to minimize the normalized mean squares error in (4.17) between the CFD results and the NARMAX model. Consequently, $T = 1$ (5.6615×10^{-5} sec.) is chosen for the sampling time and five is chosen for the maximum input lag.

Taking these factors into account, the flow model is identified based on the jet velocity shown in Fig. 64. The resulting model equation is

$$\begin{aligned}\hat{p}(k) &= f\left(v(k-10), v(k-11), v(k-12), v(k-13), v(k-14), \hat{p}(k-1), \hat{p}(k-2)\right) \\ &= \sum_{i=1}^{m_{10}} c_{10,i} v\left(k-n_{10,i}\right) + \sum_{i=1}^{m_{01}} c_{01,i} \hat{p}\left(k-n_{01,i}\right) + \sum_{i=1}^{m_{20}} c_{20,i} v\left(k-n_{20,i_1}\right) v\left(k-n_{20,i_2}\right) \\ &+ \sum_{i=1}^{m_{02}} c_{02,i} \hat{p}\left(k-n_{02,i_1}\right) \hat{p}\left(k-n_{02,i_2}\right) + \sum_{i=1}^{m_{11}} c_{11,i} v\left(k-n_{11,i_1}\right) \hat{p}\left(k-n_{11,i_2}\right),\end{aligned} \tag{6.14}$$

where $\hat{p} = p - p_0$. As shown in Fig. 65, the notation for the model coefficients follows the prior research [47]. The selected regressor terms and corresponding coefficients in (6.14) are shown in Tables VI, VII and VIII.

The response of the identified model is compared to the CFD results for the input data

Table VII. Second-order regressors and corresponding coefficients.

$v(k-n_{20,i})$	$c_{20,i}$	eRR	$\hat{p}(k-n_{02,i})$	$c_{02,i}$	eRR
$v(k-10)^2$	-84.59979	5.174e-006	$\hat{p}(k-1)^2$	-8.27884	1.207e-003
$v(k-10)v(k-11)$	361.72958	2.324e-005	$\hat{p}(k-1)y(k-2)$	8.84671	6.285e-004
$v(k-10)v(k-12)$	-318.45314	3.606e-004	$\hat{p}(k-2)^2$	-0.91634	9.539e-004
$v(k-10)v(k-13)$	194.98384	1.543e-005			
$v(k-10)v(k-14)$	-32.71129	2.072e-006			
$v(k-11)^2$	-216.76921	3.924e-006			
$v(k-11)v(k-14)$	-69.28537	1.163e-006			
$v(k-12)^2$	259.91455	1.012e-005			
$v(k-13)^2$	-309.28766	1.216e-005			
$v(k-13)v(k-14)$	301.53712	2.061e-006			
$v(k-14)^2$	-87.00064	2.868e-006			

Table VIII. Coupled regressors and corresponding coefficients.

$v(k-n_{11,i_1})\hat{p}(k-n_{11,i_2})$	$c_{11,i}$	eRR	$v(k-n_{11,i_1})\hat{p}(k-n_{11,i_2})$	$c_{11,i}$	eRR
$v(k-10)\hat{p}(k-1)$	209.50637	7.296e-005	$v(k-13)\hat{p}(k-1)$	-1100.05214	2.765e-003
$v(k-10)\hat{p}(k-2)$	-217.78114	3.870e-006	$v(k-13)\hat{p}(k-2)$	1162.65523	1.987e-003
$v(k-11)\hat{p}(k-1)$	-902.25087	1.936e-005	$v(k-14)\hat{p}(k-1)$	310.93595	1.785e-005
$v(k-11)\hat{p}(k-2)$	934.75351	6.264e-006	$v(k-14)\hat{p}(k-2)$	-336.81430	6.351e-006
$v(k-12)\hat{p}(k-1)$	1484.38763	4.712e-004			
$v(k-12)\hat{p}(k-2)$	-1545.48451	1.299e-005			

utilized in the identification procedure as shown in Fig. 66 From Fig. 66(a), the normalized mean squares error in (4.17) is estimated at 10.19%. In Fig. 66(b), the errors between the model and the CFD simulation are presented in the frequency domain. The error is normalized with respect to the model, since this relative error would be employed to estimate the uncertainty of the model with respect to the original plant. Note that as the errors are presented relatively at each frequency component, those are exaggerated at some frequencies although the signal magnitudes are very weak. For example, the large error peaks in $f = 0.006 \sim 0.010$ can be negligible.

The model errors range from -20 dB to 10 dB in the input frequency band and from -30 dB to -10 dB in the carrier frequency band. The identified model matches the response of the carrier frequency band more accurately than that of the input frequency band. However, the NARMAX model captures the overall characteristics of the frequency distribution qual-

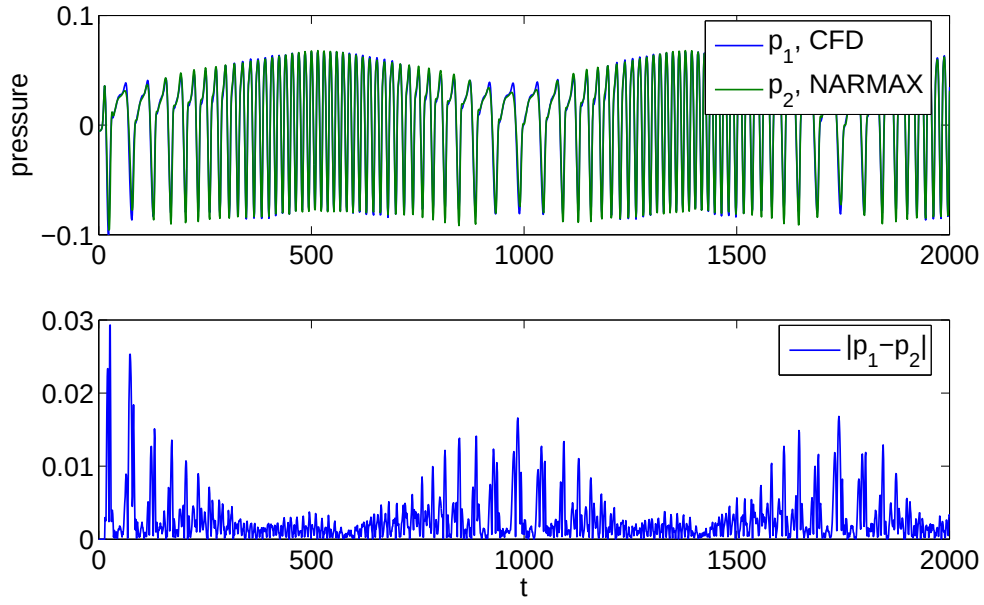

(a) Time domain (partially presented).

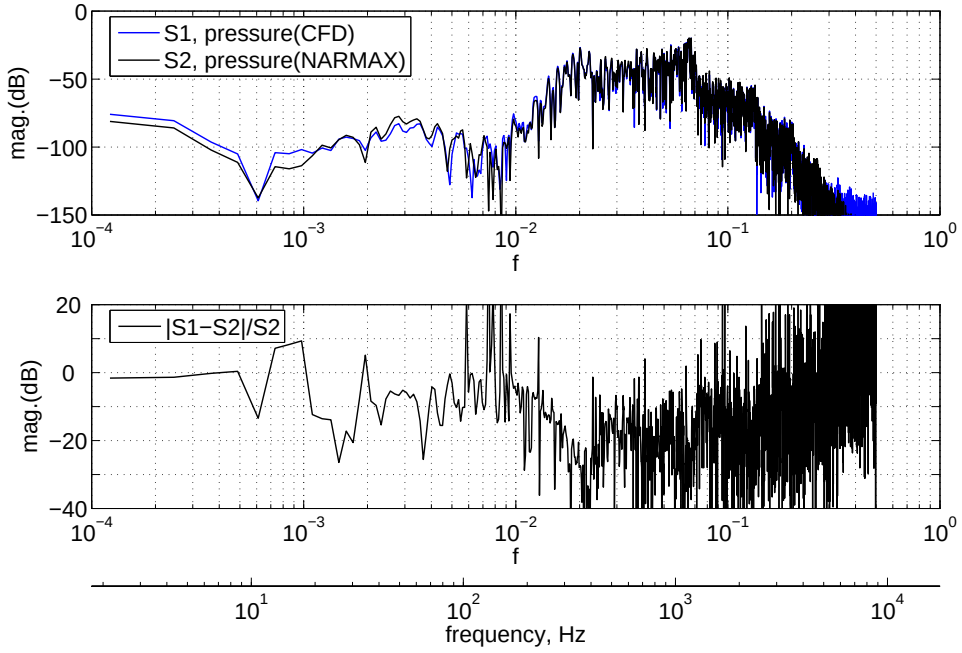

(b) Frequency spectrum (DC component is detrended).

Fig. 66. Comparison of the CFD results and the NARMAX model for the velocity profile of Fig. 64.

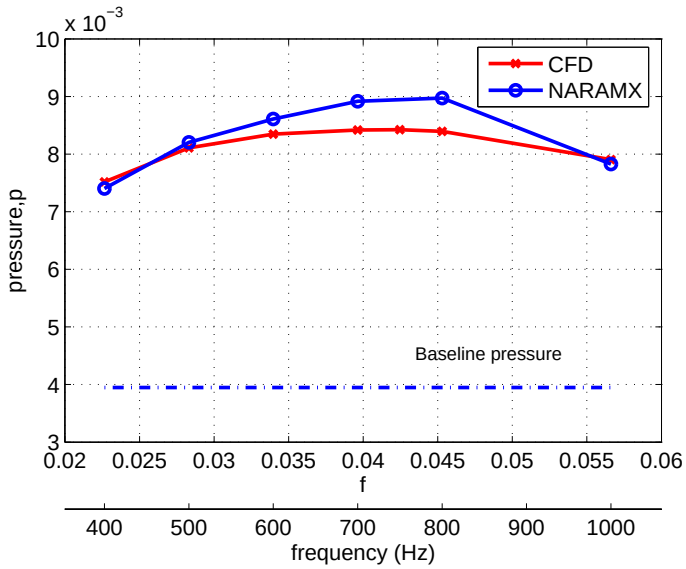

Fig. 67. Relationship between the mean pressure and the jet frequency for the NARMAX model and the CFD results.

itatively. Hence, despite the error of the NARMAX model, the feasibility of the proposed feedback control approach can be examined based upon the identified model.

4. Model Verification

First of all, Fig. 67 shows the relationship between the mean pressure and the jet frequency in the NARMAX model, which is compared with the CFD results. The identified model matches the CFD model within 8% error in terms of the mean pressure.

To verify the model accuracy in the input frequency band, different constant frequencies are chosen for f_u in (6.10). In Fig. 68, the case for f_u =0.0022 (38.8 Hz), f_c =0.0395 (698 Hz) and Δf =0.0197 (348 Hz) in (6.10) is examined in the time and frequency domain, respectively. The bottom plot in Fig. 68(a) presents the pressure signal passing through the low-pass filter designed in Section G. The frequency component at f_u shows -5 dB magnitude and 44 degree phase errors. Figure 69 presents the case for f_u =0.0027 (47.4 Hz), f_c =0.0324 (573 Hz) and Δf =0.0098 (173 Hz). The frequency component at f_u shows -5

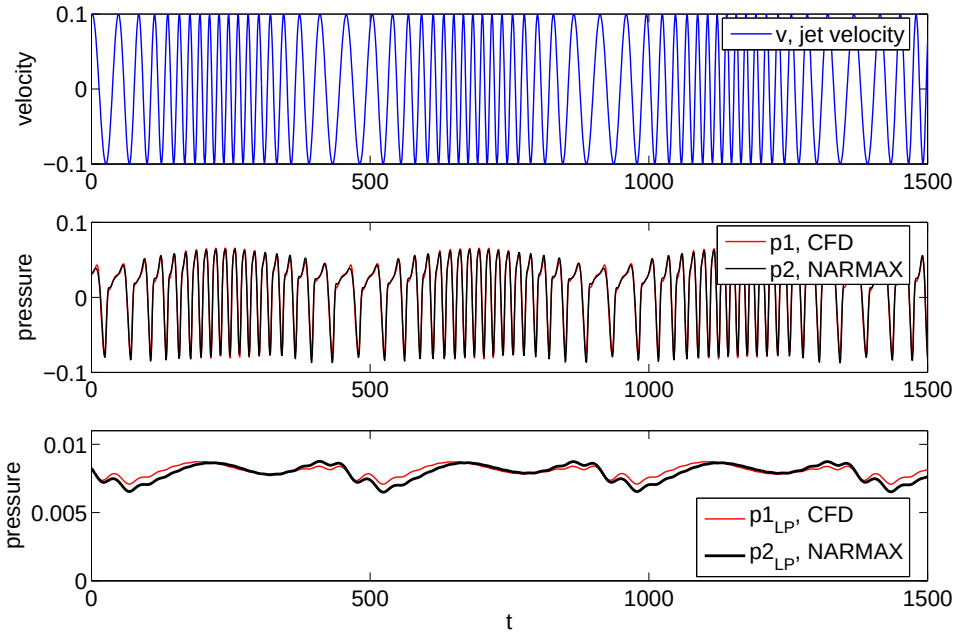

(a) Time domain (partially presented).

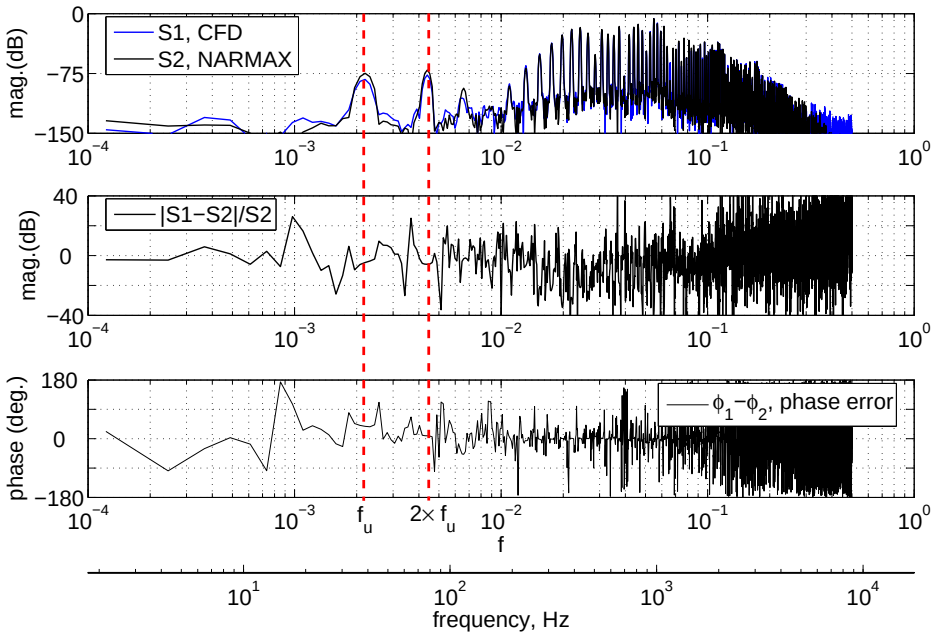

(b) Frequency spectrum (DC component is detrended).

Fig. 68. Comparison of the CFD result and the NARMAX model for the input f_c =0.0395 (698 Hz), Δf =0.0197 (348 Hz) and f_u =0.0022 (38.8 Hz).

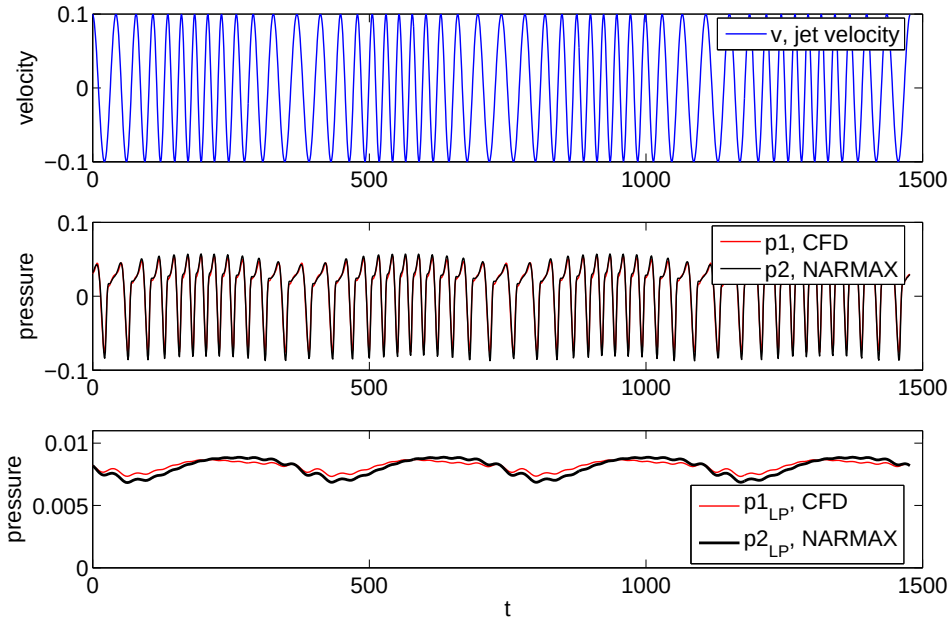

(a) Time domain (partially presented).

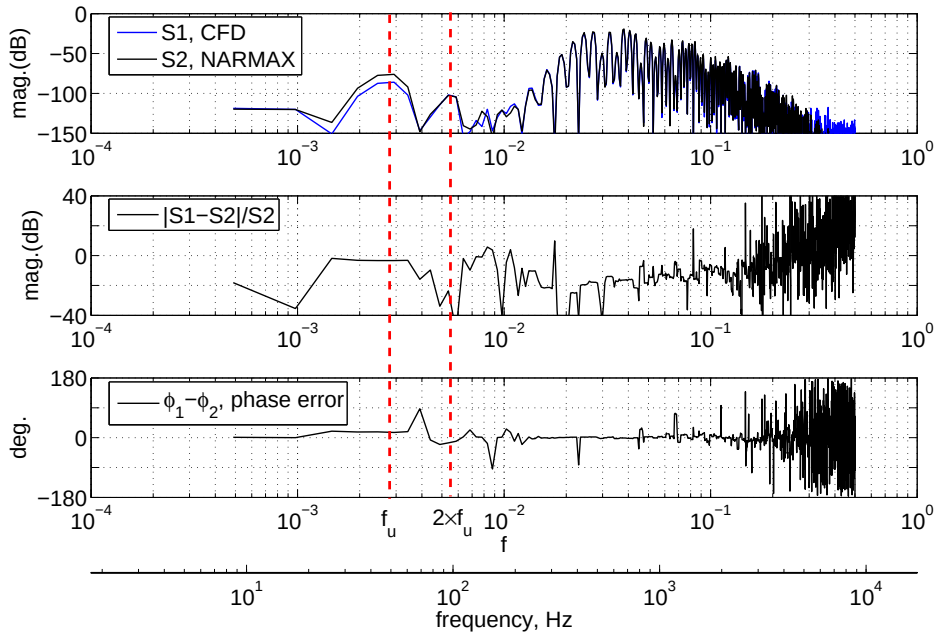

(b) Frequency spectrum (DC component is detrended).

Fig. 69. Comparison of the CFD result and the NARMAX model for the input f_c =0.0324 (573 Hz), Δf =0.0098 (173 Hz) and f_u =0.0027 (47.4 Hz).

dB magnitude and 14 degree phase errors.

Based on these and other results, the NARMAX model shows -20$\sim$10 dB magnitude and 0$\sim$50 degree phase errors compared with the CFD results. These errors are considered for the stability margin in the feedback controller design.

5. Summary of NARMAX Model

The fluidic system including synthetic jet actuation shows distinctive behaviors: The actuator modulates the jet velocity by the input signal, using the DC magnitude of the input as a carrier frequency. The nonlinear fluidic system passes the carrier frequency band and demodulates the input signal into the low frequency range. As the control system operates in the low frequency range, the main goal of the system identification is to identify the relationship between the input jet frequency and the demodulated nonlinear response.

The NARMAX model shows accurate performance in the carrier frequency band (-30 dB $\sim$ -10 dB error), whereas it is less accurate in the input frequency band (-20 dB $\sim$ 10 dB error), i.e. less accurate demodulation. However, it captures the key characteristics of the system qualitatively: DC component, demodulated signal components and high carrier frequency components. While the controller based on the NARMAX model may not work properly if the controller is applied directly to CFD simulations or experiments, the proposed control methodology can be validated by the identified model.

The magnitudes of the demodulated frequency components are -40 dB less than those of the carrier frequency band. It is conjectured that the NARMAX model is identified to match the carrier frequency band more accurately, as it has a dominant signal strength. Therefore, if the identification method is applied to the fluidic system including the actuator in (6.9) and low-pass filter, the model accuracy could be improved with respect to the input frequency band, as the input frequency band becomes dominant for this system.

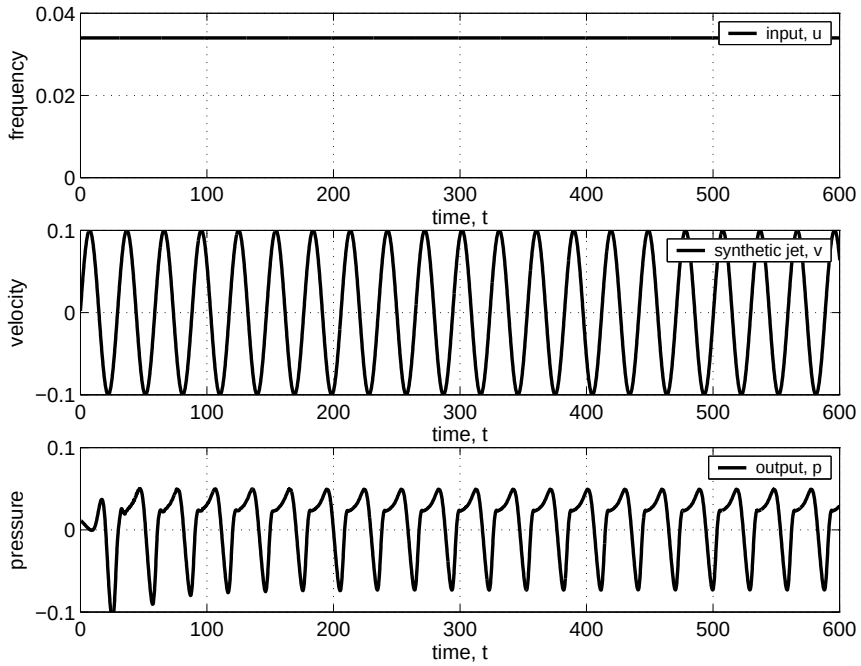

Fig. 70. Pressure response with respect to a constant input $u = 0.0340$ (600Hz).

G. Design of a Low-pass Filter

The difficulties of this control problem arise from the sinusoidal characteristics of the actuator as well as the nonlinear flow dynamics. To keep the fundamental nature of synthetic jets, i.e. zero-net-mass-flux, the actuator cannot produce an arbitrary profile of the jet velocity. The velocity profile is restricted to a periodic configuration so that possible control variables are jet magnitude and frequency. In this research, the jet magnitude is assumed to be constant and only the frequency can be varied as shown in (6.6).

Given a constant input, a linear system produces a constant value in the steady state. In contrast, this fluidic system behaves in a different way with respect to the constant input as shown in Fig. 70. Although the input u is constant, the synthetic jet velocity v oscillates due to the integral operation inside of the actuator and the pressure output p also fluctuates periodically. These difficulties, however, can be alleviated, considering that the aimed

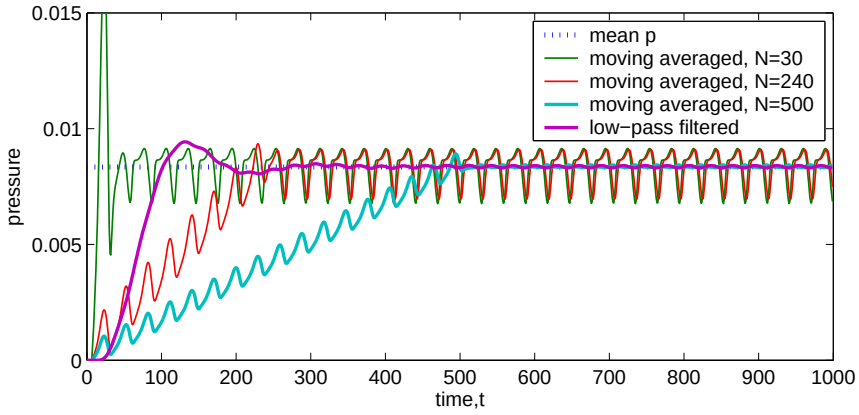

Fig. 71. Moving average of the pressure response with respect to the constant input $u = 0.0340$ (600Hz).

property for the control is not the pressure response p itself but the mean pressure $\bar{p}$ as shown in Fig. 56.

Before going further, the drawbacks of averaging are discussed and a low-pass filter is introduced as an alternative. Suppose that a moving-average-type filter using N data points in (6.15) is applied to extract the mean pressure while the system runs.

$$\bar{p}(k) = \frac{1}{N}\sum_{i=0}^{N-1} p(k-i). \tag{6.15}$$

This filter, however, is not suitable for this application. As the moving average is basically the method to smooth data with a small N, a great number of data is necessary to effectively suppress the harmonic frequency components. For example, if the jet frequency is $f_j = 0.0340$ (600Hz) in Fig. 70, the least number of N to get the average of one cycle is 30 for the sampling time $T = 1$. Figure 71 presents the results of the moving average applied to the pressure output p of Fig. 70. It shows that the moving average needs 500 data points to obtain a mean value close to the mean pressure and it has a slow transition until the steady state is reached.

In this research, a IIR low-pass filter is proposed in place of averaging, based upon

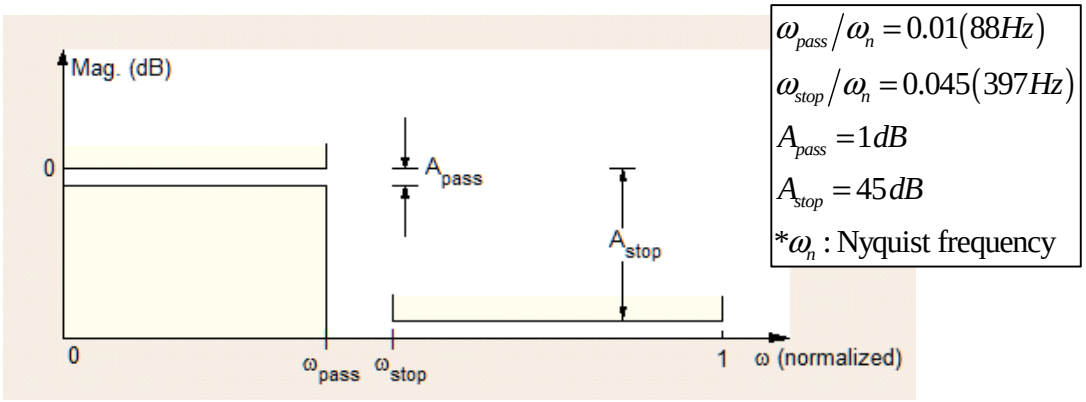

Fig. 72. Specification for the fourth order Butterworth low-pass filter.

two facts: First, a DC component at zero frequency, extracted by the low-pass filter, is equivalent to the average of the signal, since the pressure signal is periodic. Secondly, low-pass filtering requires the smaller number of the data and shows the faster transient response than averaging as shown in Fig. 71.

The effect of low-pass filtering on the pressure response is to preserve the DC component and attenuate the higher frequency component at the same time. If the DC component dominates the higher frequency components after filtering, the chance to design the successful linear controller would be improved, since the relationship between the system input, i.e. jet frequency input and DC component in p resembles a linear system, even though it is still the nonlinear system. In order to guarantee the dominance of the DC component in the filtered signal, the stop frequency of the filter is to be less than or equal to the lower bound of the synthetic jet frequency. Considering the prior discussions as to the control objectives, the lower limit of the jet frequency is assumed to be $f = 0.0226$ (400Hz). As a result, the specification of the designed low pass filter is shown in Fig. 72. The pass frequency is 0.0050 (88 Hz) and the signal is suppressed by -45dB at the stop frequency

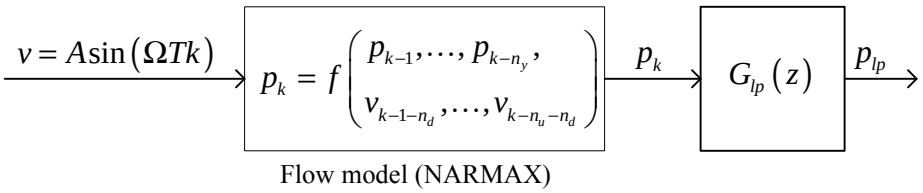

Fig. 73. Fluidic system blocks where the describing function analysis is applied.

0.0225 (397 Hz). The resultant fourth order Butterworth low-pass filter is

$$G_{lp}(z) = \frac{a_0 + a_1 z^{-1} + a_2 z^{-2} + a_3 z^{-3} + a_4 z^{-4}}{b_0 + b_1 z^{-1} + b_2 z^{-2} + b_3 z^{-3} + b_4 z^{-4}}, \tag{6.16}$$

where the filter coefficients satisfying the specification are

$$\begin{bmatrix} a_0 \\ a_1 \\ a_2 \\ a_3 \\ a_4 \end{bmatrix} = \begin{bmatrix} 0.1343 \\ 0.5374 \\ 0.8061 \\ 0.5374 \\ 0.1343 \end{bmatrix} \times 10^{-6}, \qquad \begin{bmatrix} b_0 \\ b_1 \\ b_2 \\ b_3 \\ b_4 \end{bmatrix} = \begin{bmatrix} 1.0000 \\ -3.8987 \\ 5.7012 \\ -3.7061 \\ 0.9036 \end{bmatrix}. \tag{6.17}$$

H. Describing Function Analysis

The effects of the low-pass filter on the fluidic system shown in Fig. 73 are examined by the frequency response analysis. A direct frequency analysis for the fluidic system is not possible due to its nonlinearity. Alternatively, the describing function method is employed to analyze the quasi-linear frequency response of the NARMAX model with respect to the sinusoidal input. In addition, by comparing the frequency response of the pressure before and after low-pass filtering G_{lp}, the benefits of the filter to facilitate the feedback controller design are discussed.

1. Describing Function

Similar to a linear frequency response method, a describing function method can be used to approximately analyze the frequency response of a nonlinear system while its main purpose is to predict a limit cycle oscillation of the system [47,66]. The describing function, i.e. the quasi-linear model, of the nonlinear system varies depending on the type of input such as a bias, a sinusoid, or a Gaussian random signal. In this research, the sinusoidal input describing function (SIDF) is considered.

The fundamental assumption of the SIDF is that given the sinusoidal input, the higher frequency component of the nonlinear output can be neglected compared with the fundamental frequency component. It is referred to as low-pass filtering hypothesis [66]. Suppose that the single sinusoidal input is

$$\begin{aligned} v(t) &= A\sin(\Omega t), \\ &= \frac{A}{2j}\left(e^{j\Omega t} - e^{-j\Omega t}\right). \end{aligned} \tag{6.18}$$

If the nonlinear output $p(t)$ is periodic and its derivative is piecewise smooth on the periodic interval $0 \leq t \leq \frac{2\pi}{\Omega}$ [48], $p(t)$ can be expanded to a Fourier series

$$p(t) = \sum_{n=0}^{\infty} H_n e^{jn\Omega t},\ H_n = \frac{\Omega}{2\pi}\int_0^{2\pi/\Omega} p(t)\, e^{-jn\Omega t} dt. \tag{6.19}$$

Dividing the fundamental Fourier coefficient in (6.19) by the input amplitude leads to the describing function [67]

$$N_A(A, j\Omega) = \frac{\Omega}{\pi A}\int_0^{2\pi/\Omega} p(t)\,(\sin\Omega t + j\cos\Omega t)\, dt. \tag{6.20}$$

2. Harmonic Balance Method

The prior research has developed the method to compute the describing function in a NARMAX system [47]. The input sinusoid and the truncated Fourier series of the output in

(6.19) are discretized and substituted into the NARMAX equation. Based upon the harmonic balance method [68], the value of the describing function at the frequency Ω is sought to satisfy the coefficients of each harmonic component. This method is implemented to extract and analyze the harmonic frequency components of the pressure output.

Since the identified NARMAX model has the periodic steady-state output response with respect to the single sinusoidal input $v(k) = A\sin(\Omega T \cdot k)$, the output can be expanded by the Fourier series

$$p(k) = A_{DC} + \sum_{n=1}^{\infty} a_k \sin(n\Omega T \cdot k + \phi_n), \tag{6.21}$$

where A_{DC} is a DC component and a_k a Fourier series coefficient. In the complex domain, the input and output can be rewritten as

$$v(k) = \frac{A}{2j}\left(e^{j\Omega Tk} - e^{-j\Omega Tk}\right), \tag{6.22}$$

$$p(k) = A_{DC}(A, j\Omega) + \sum_{n=1}^{\infty} \frac{1}{2j}\left(H_n(A, jn\Omega)e^{jn\Omega Tk} - H_n(A, -jn\Omega)e^{-jn\Omega Tk}\right). \tag{6.23}$$

Consequently, the describing function is derived from (6.22) and (6.23) as

$$N(A, j\Omega) = \frac{H_1(A, j\Omega)}{A}. \tag{6.24}$$

If the DC and fundamental frequency terms are dominant in (6.23), the truncated response is considered as

$$\tilde{p}(k) = A_{DC}(A, j\Omega) + \frac{1}{2j}H_1(A, j\Omega)e^{j\Omega Tk} - \frac{1}{2j}H_1(A, -j\Omega)e^{-j\Omega Tk}. \tag{6.25}$$

By applying the sinusoidal input (6.22) and output (6.23) to the NARMAX equation, the first order harmonic balance equations are derived as

$$C_3X^2 + (C_1 - 1)X + C_4Y^2 + 2C_5Y + C_4Z^2 - 2C_6Z + C_2 = 0, \tag{6.26}$$

$$(C_{11}X + C_9)Y - \left(C_{12}X + C_{10} + \frac{1}{2}\right)Z + C_{13}X + C_7 = 0, \tag{6.27}$$

$$\left(C_{12}X + C_{10} + \frac{1}{2}\right)Y + (C_{11}X + C_9)Z + C_{14}X + C_8 = 0, \tag{6.28}$$

where $X = A_{DC}(A, j\Omega)$, $Y + jZ = H_1(A, j\Omega)$ and $[X, Y, Z, \forall C_s] \in R$, $s \in [1, \ldots, 14]$. The reader may refer to Appendix A for the detailed derivation. The variables X, Y and Z are numerically solved with the given A, Ω and known C's.

The more the higher harmonic terms are added to (6.25), the better the accuracy of A_{DC} and H_1 improves. However, the computation becomes more intensive due to the increasing complexity of the harmonic balance equations. Considering the second harmonic component in (6.23), the second order harmonic balance equations turn out to be

$$C_3X^2 + (C_1 - 1)X + C_4Y^2 + 2C_5Y + C_4Z^2 - 2C_6Z + C_2 + C_{15}S^2 + C_{15}T^2 = 0, \tag{6.29}$$

$$\begin{aligned}&(C_{11}X + C_9)Y - \left(C_{12}X + C_{10} + \frac{1}{2}\right)Z + C_{13}X + C_7 + C_{18}S - C_{19}T \\ &+C_{16}(YS + ZT) - C_{17}(YT - SZ) = 0,\end{aligned} \tag{6.30}$$

$$\begin{aligned}&\left(C_{12}X + C_{10} + \frac{1}{2}\right)Y + (C_{11}X + C_9)Z + C_{14}X + C_8 + C_{19}S + C_{18}T \\ &+C_{17}(YS + ZT) + C_{16}(YT - SZ) = 0,\end{aligned} \tag{6.31}$$

$$\begin{aligned}&-\frac{1}{2}T + C_{20}S - C_{21}T + C_{22} + C_{24}\left(Y^2 - Z^2\right) - 2C_{25}YZ + C_{26}XS \\ &-C_{27}XT + C_{28}Y - C_{29}Z = 0,\end{aligned} \tag{6.32}$$

$$\begin{aligned}&\frac{1}{2}S + C_{20}T + C_{21}S + C_{23} + C_{25}\left(Y^2 - Z^2\right) + 2C_{24}YZ \\ &+C_{27}XS + C_{26}XT + C_{29}Y + C_{28}Z = 0,\end{aligned} \tag{6.33}$$

where $X = A_{DC}(A, j\Omega)$, $Y + jZ = H_1(A, j\Omega)$, $S + jT = H_2(A, j2\Omega)$ and $[X, Y, Z, S, T, \forall C_s] \in R$, $s \in [1, \ldots, 28]$. The reader may refer to Appendix B for the detailed derivation. As the same way with the first order equations, the unknown variables X, Y, Z, S and T are

numerically solved with the given A, Ω and known C's.

Figure 74 compares $A_{DC}(A, j\Omega)$, $H_1(A, j\Omega)$ and $H_2(A, j\Omega)$ computed from the first and second-order harmonic balance equations of the NARMAX model. The jet frequency $f_j(=\Omega/2\pi)$ ranges from 0.0283 (500 Hz) to 0.0566 (1000Hz). Regarding the magnitude of the DC component, the second-order harmonic balance equations capture the value more accurately than the 1 st order equations do, compared with mean wall pressure.

3. Effects of the Low-pass Filter

The frequency responses of the second-order harmonic balance equations allow estimating the first and second harmonic frequency components of the steady-state output as follows.

$$\tilde{p}_{\Omega} = \frac{1}{2j}\left\{H_1(A, j\Omega)e^{j\Omega Tk} - H_1(A, -j\Omega)e^{-j\Omega Tk}\right\}, \tag{6.34}$$

$$\tilde{p}_{2\Omega} = \frac{1}{2j}\left\{H_2(A, j2\Omega)e^{j2\Omega Tk} - H_2(A, -j2\Omega)e^{-j2\Omega Tk}\right\}. \tag{6.35}$$

Figure 75 presents how the designed low-pass filter, $G_{lp}(z)$, affects each frequency components. Evidently, the low-pass filter attenuates the amplitude of $\tilde{p}_{\Omega}$ and $\tilde{p}_{2\Omega}$ while it preserves the magnitude of A_{DC}. The signal level of the harmonic components is reduced approximately from $5\times10^{-}2$ to $5\times10^{-}5$. Figure 76 presents the magnitudes of H_1, which is the approximation of the first harmonic component and $G_{lp}\cdot H_1$, which is the first harmonic component after filtering, over the range of the jet frequency $f_j = 0.0283 \sim 0.0566$. Before filtering, the fundamental component, H_1, is greater about 20 dB than the DC component, A_{DC}. The filtering drops the magnitude of $H_1 G_{lp}$ by more than -35 dB over the entire frequency domain with respect to the DC component. Thus the harmonic components, which are dominant signals by comparison with the DC component before filtering, become less significant than the DC value after filtering.

Conclusively, if the low-pass filter is properly designed, which means that the filter

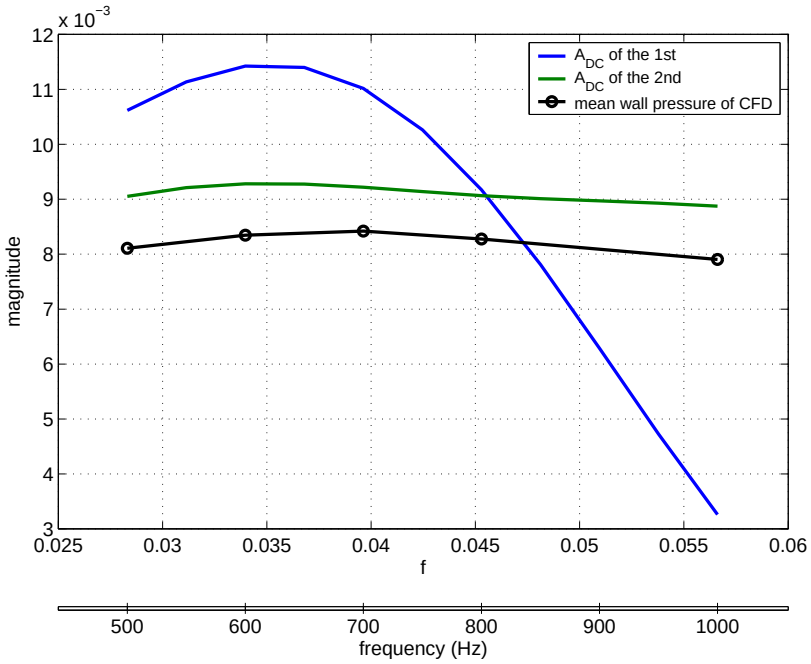

(a) A_{DC} (DC component).

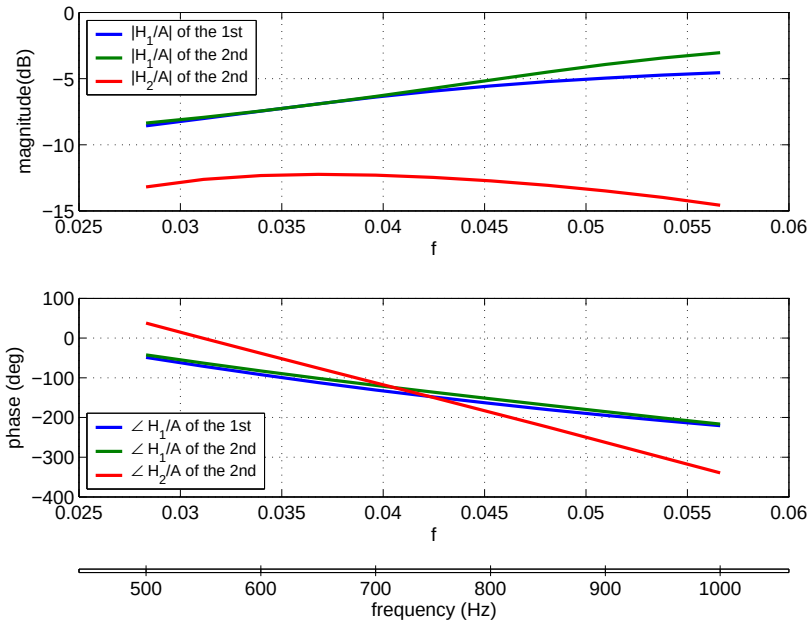

(b) H_1, H_2 (Harmonic components).

Fig. 74. Comparison of A_{DC}, H_1 and H_2 obtained from the first and second harmonic balance equations.

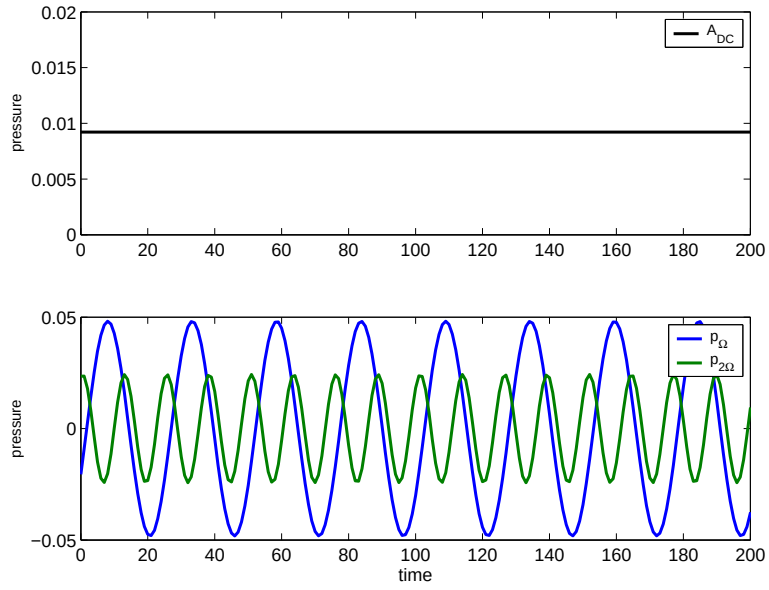

(a) Before filtering.

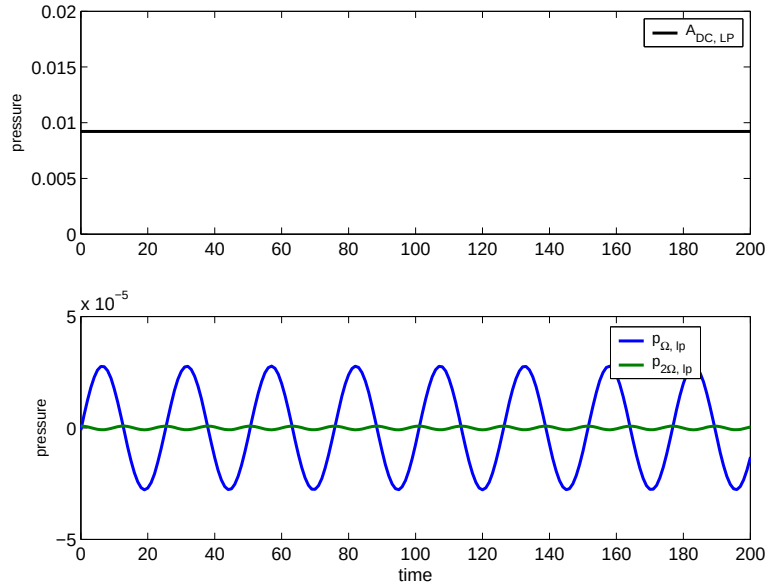

(b) After filtering.

Fig. 75. Effects of the low-pass filtering on each DC and harmonic component for the jet frequency $f = 0.0396$ (700 Hz).

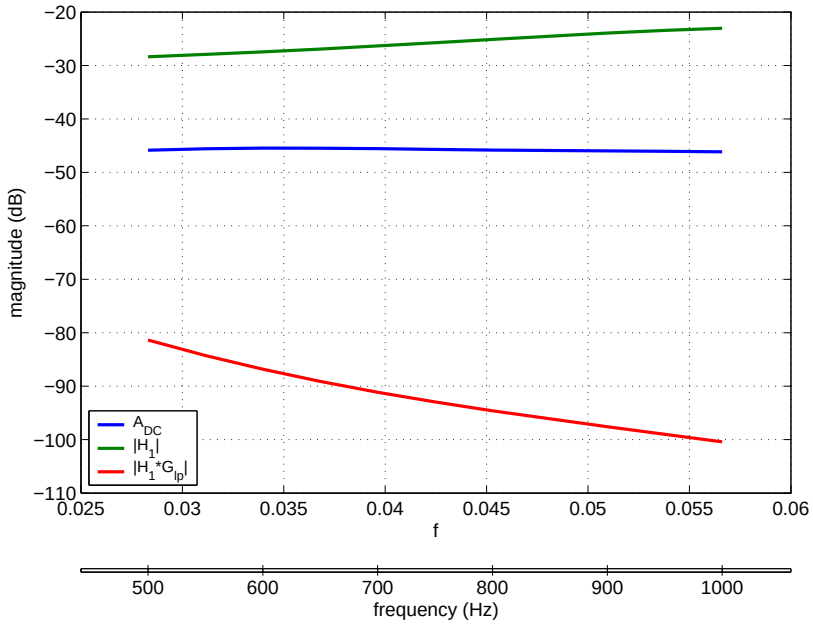

Fig. 76. Variation of the fundamental frequency component of the pressure output by the low-pass filtering.

attenuation over the stop frequency should be enough to suppress the higher harmonic components of the system response, the nonlinear signal passing through the filter is separated into the DC component and the attenuated harmonic frequency components. In the controller design, the former is implemented for the feedback signal and the latter can be treated as internal nonlinear disturbances.

In what follows, the term “quasi-linear response” will be preferred rather than the term “DC component” in order to describe the low-pass filtered output p_{lp} more correctly. If the frequency input u varies in time, i.e. the rate of change of u is not zero, the “DC component” will not stay at the zero frequency any more. In that sense, the term “quasi-linear response” is used, taking into account that p_{lp} shows the quasi-linear characteristics with respect to u as evidenced in the following section.

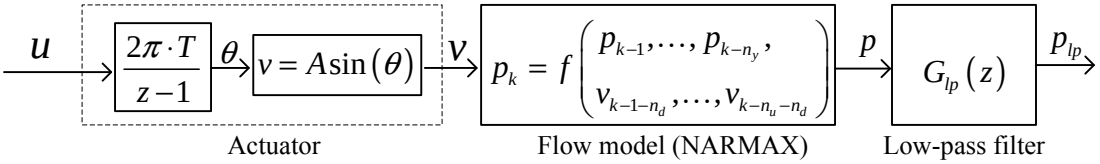

Fig. 77. Open loop system.

I. Open Loop Responses

In this section, the frequency response of the open loop system shown in Fig. 77 is analyzed. Utilizing step and sinusoidal inputs for the jet frequency *u*, the quasi-linear characteristics of the system incorporating the low pass filter are discussed.

First of all, the system response for the step inputs is demonstrated in Fig. 78. At $f = 0.0266$ (400 Hz), the filtered output shows the disturbance coming internally from the high frequency components. The disturbances disappear by increasing the jet frequency to 0.0425 (750 Hz), since the filter is more effective as the frequency increases over the stop frequency. Interestingly, with the jet frequency stepped onto 0.0623, the filtered pressure falls down due to the nonlinear relationship between the jet frequency and the mean wall pressure in Fig. 67. Evidently, the transient response of the filtered output resembles the typical characteristics of a second-order linear system.

Figure 79 presents the example of the system response for the sinusoidal input. The jet actuation frequency is assumed to oscillate from 0.0226 (400 Hz) to 0.0425 (750 Hz) by the rate of change $f_u = 0.0011$ (20Hz). The resultant input signal is

$$u(k) = -\frac{0.0425 - 0.0226}{2}\cos\left(2\pi \cdot 0.0011Tk\right) + \frac{0.0425 + 0.0226}{2}. \tag{6.36}$$

The oscillation of the jet frequency results in chirping of the jet velocity. Responding to the chirping jet velocity, the output pressure can be divided into three distinctive frequency bands: the DC component, the harmonic components of f_u and the dominant widespread

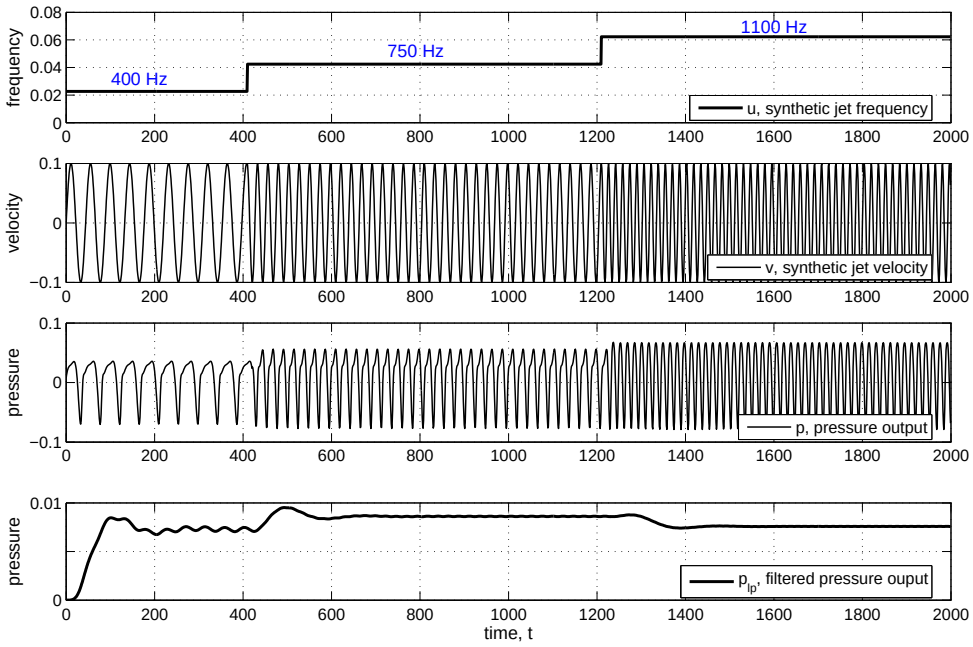

Fig. 78. Open loop responses for the step inputs.

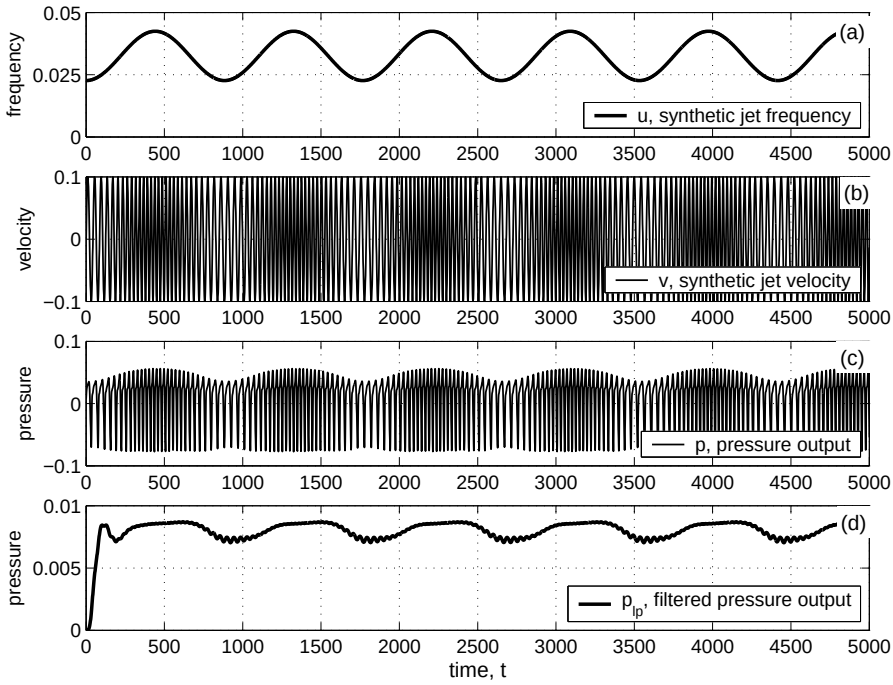

(a) Time domain.

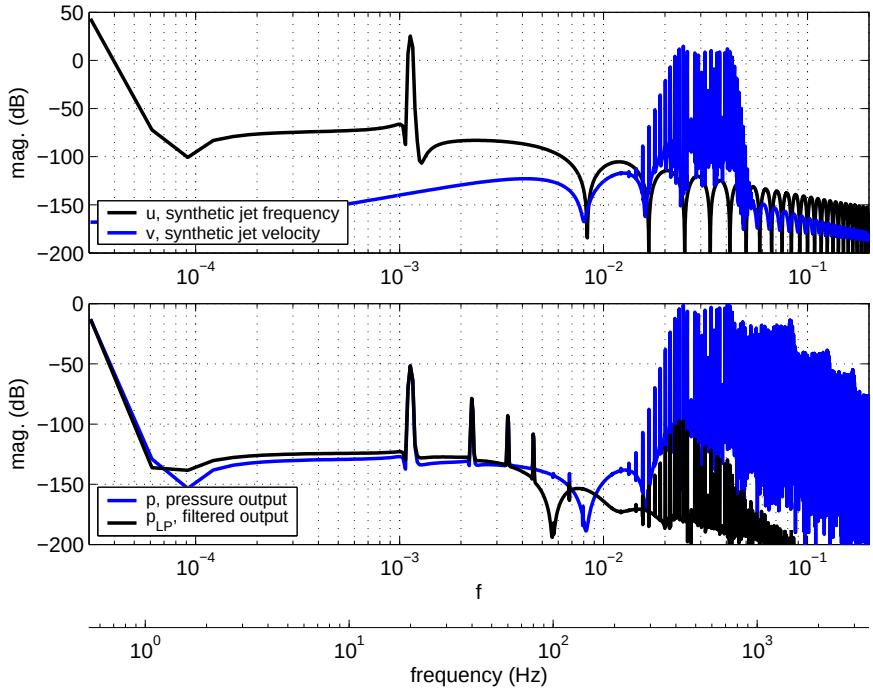

(b) Frequency domain.

Fig. 79. Open loop system responses for the sinusoidal input with $f_u = 0.0011$ (20 Hz).

frequency components beyond $f = 0.01$. After low-pass filtering, the fundamental frequency component corresponding to f_u emerges as a primary component except the DC component. Approximately, the higher frequency components are -30 dB less than the fundamental component so that those behave as if those were small disturbances.

Figure 80 shows the extreme cases for $f_u = 0.0003$(5 Hz), which is close to zero, and $f_u = 0.0045$ (80 Hz), which is just below the filter pass frequency. The features of the frequency spectrums are consistent with the former case.

1. Low-pass Filter Hypothesis

In what follows, The effects of the low-pass filter on the system response are generalized. Suppose that the oscillating jet frequency as an input is assumed to be

$$u(k) = \frac{\Omega}{2\pi} + \frac{\Delta\Omega}{2\pi}\sin(\omega_u T k), \tag{6.37}$$

where $\Omega = 2\pi f_j$, $\omega_u = 2\pi f_u$. Ω stands for the constant synthetic jet frequency and ω_u does for the rate of change of the synthetic jet frequency. $\Delta\Omega$ denotes the magnitude of oscillation and is less than $\Omega/2$. Those are expressed in terms of the angular frequency.

With an emphasis on the coupled effects of Ω and ω_u, the steady-state open loop response to this input can be described as

$$\begin{aligned} p(k) =& DC(\Omega) + H_1(\Omega, \Delta\Omega, j\omega_u)e^{j\omega_u T k} \\ &+ \sum_{n=2}^{\infty} H_n(\Omega, \Delta\Omega, jn\omega_u)e^{jn\omega_u T k} + B(j\Omega, j\Delta\Omega, j\omega_u), \end{aligned} \tag{6.38}$$

where DC, H_1 and H_n denote the complex coefficients corresponding to each frequency component of the signal. These terms are illustrated in Fig. 81(a). The DC and H_1 terms are the direct counterparts of Ω and $\sin(\omega_u T k)$ in the input respectively. $H_n (n \geq 2)$ terms are generated as higher harmonics of ω_u due to the nonlinearity. The last term B represents widespread frequency components caused by coupling of Ω, $\Delta\Omega$ and ω_u.

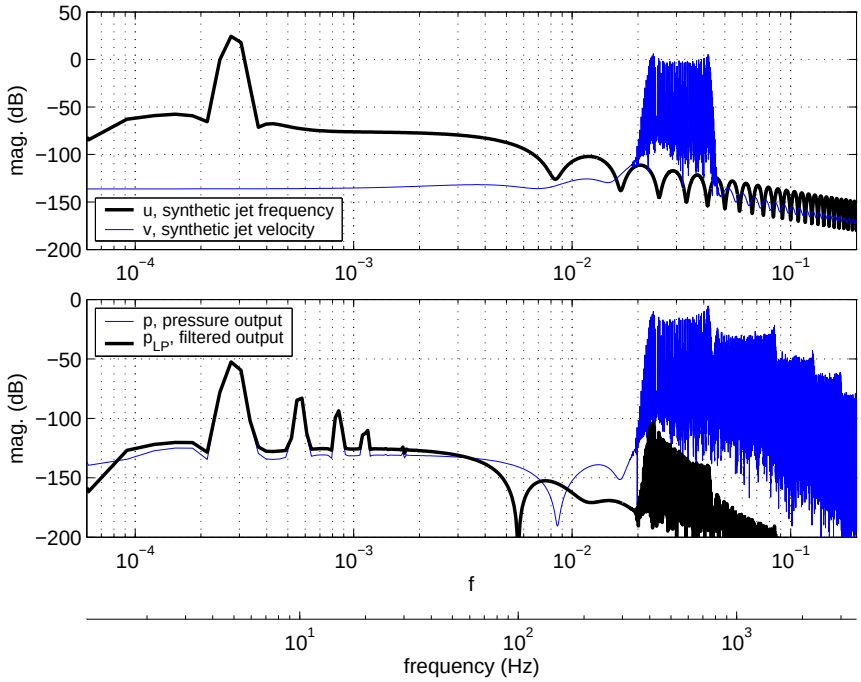

(a) $f_u = 0.0003$ (5Hz)

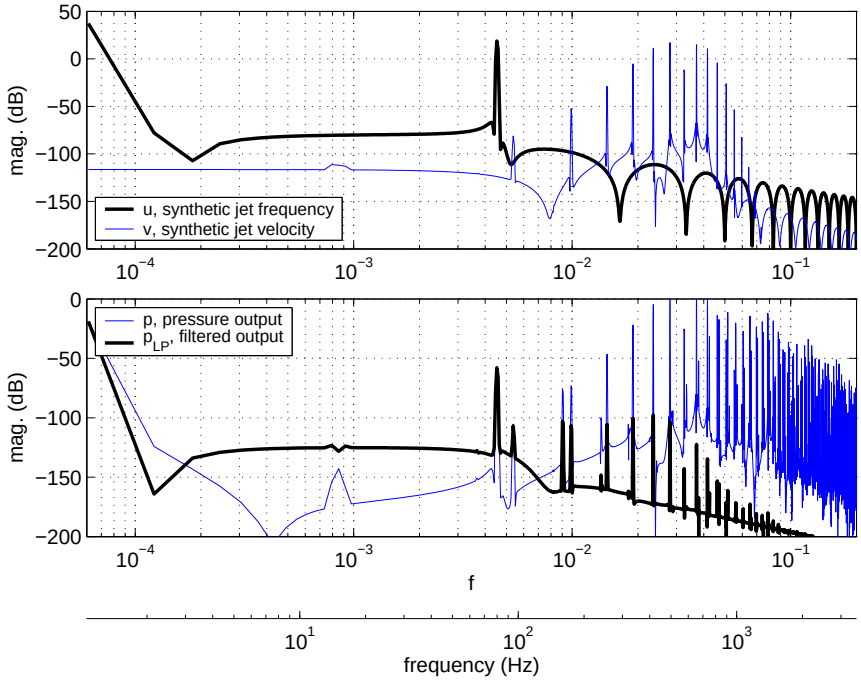

(b) $f_u = 0.0045$ (80Hz)

Fig. 80. Frequency spectrum of open loop responses for the different sinusoidal inputs.

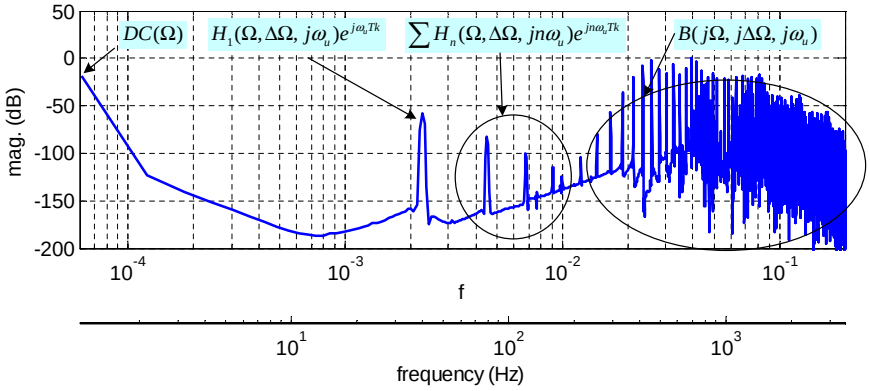

(a) Before low-pass filtering

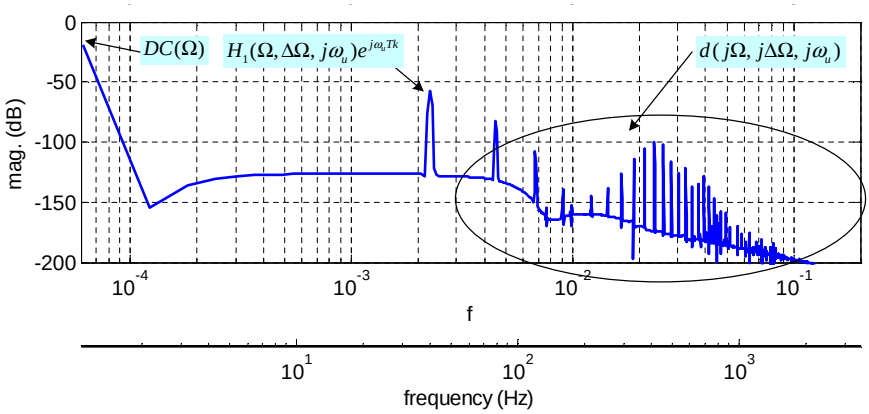

(b) After low-pass filtering

Fig. 81. Frequency spectrum of the steady-state pressure response to the sinusoidal input with $f_u = 0.0023$ (40Hz).

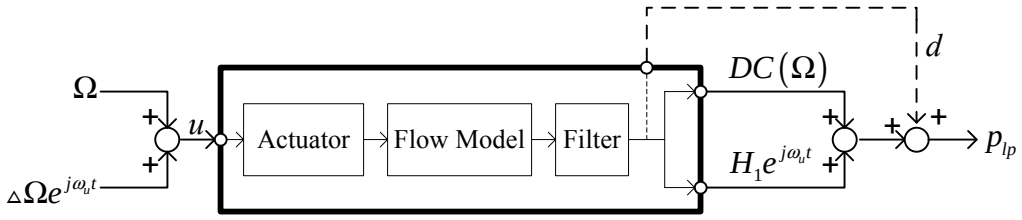

Fig. 82. Quasi-linear characteristics of the nonlinear flow system incorporating the low-pass filter.

As shown in Fig. 81(a), the magnitudes of H_n are inherently small compared with the fundamental frequency term, H_1. This characteristic is crucial for the linear approximation of the system, since these harmonics are usually lower than the filter pass frequency so that the filter can hardly affect those. In contrast, the term B, which is a main signal before filtering, can be readily filtered out, since it is located at the high frequency band of jet actuation. Finally, the low-pass filtering reduces (6.38) to

$$p(k) \approx DC(\Omega) + H_1(\Omega, \Delta\Omega, j\omega_u)e^{j\omega_u Tk} + d(j\Omega, j\Delta\Omega, j\omega_u), \tag{6.39}$$

where all the higher harmonic components are collapsed into the small disturbance, d. Figure 81(b) illustrates these effects. This low-pass filtering effects can be justified by the low-pass filter hypothesis [66], which claims that all the higher harmonics can be neglected in the analysis, as compared with the fundamental component, only if the low-pass filter can attenuate the higher harmonic terms significantly.

As shown in Fig. 82, incorporating the low-pass filter into the fluid system facilitates to disregard higher harmonics and analyze the system based upon the one-to-one correspondence of the input-output frequency components at DC and ω_u. Interestingly, this relationship is similar to the basic characteristic of linear system so that it can be considered as a quasi-linear approximation of the system and utilized to design the linear feedback controller. The characteristics of $DC(\Omega)$ are already known from the relationship between

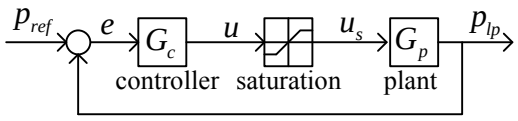

Fig. 83. Closed loop containing the quasi-linear plant model.

the jet frequency and the mean pressure in Fig. 67. In the following section, the analysis of H_1, which stands for the quasi-linear dynamics of the system, is performed.

J. Closed Loop Responses

Fig 83 presents the closed control loop for the fluidic system, $G_p(z)$, including the actuator model, NARMAX flow model and low-pass filter. $G_c(z)$ denotes the linear controller to be designed.

1. Saturation

In this closed loop, the saturation is interposed between the controller and the plant model as follows.

$$u_s = \begin{cases} f_{\min} & \text{for } u < f_{\min}, \\ u & \text{for } f_{\min} \le u \le f_{\max}, \\ f_{\max} & \text{for } u > f_{\max}. \end{cases} \tag{6.40}$$

The roles of the saturation are:

- The single value of the pressure is achieved simultaneously at two different jet frequencies as shown in Fig. 84. The upper bound of the saturation, $\Omega_{\max}(=2\pi f_{\max})$, is set at the jet frequency corresponding to the maximum pressure peak, $p_{lp,\max}$, so as to ensure that the jet frequency operates only on the left side of the plot in Fig. 84.

- The lower bound of the saturation, $\Omega_{\min}(=2\pi f_{\min})$, should be equal to or greater

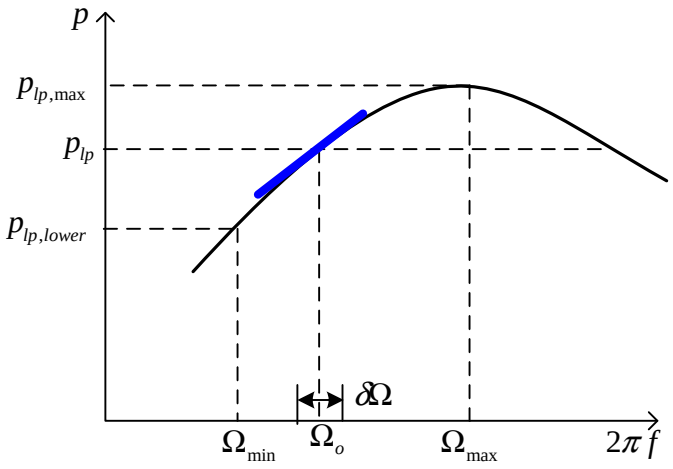

Fig. 84. Typical characteristic curve in steady state between the synthetic jet frequency and the filter output.

than the filter stop frequency to guarantee the frequency-band separation between the jet actuation frequency and the rate of change of the jet frequency.

Consequently, the range of the saturation is set by $f_{\min} = 0.0266$ (400Hz) and $f_{\max} = 0.0455$ (750Hz).

2. Frequency Response Analysis

If the linearized model of a nonlinear system with respect to a certain operating point is available, the frequency response is obtained readily from its Fourier transform although the system is assumed to operate near the operating point. However, the fluidic system in this research is not linearizable due to the integration inside of the actuator. Therefore, the approximate frequency response as regards $H_1(\Omega, \Delta\Omega, j\omega_u)$ is analyzed using the describing function method.

Assuming the small perturbation, $\delta\Omega(\ll \Omega)$, at the constant jet frequency Ω, the sinusoidal input is applied to the system as follows.

$$u(k) = \frac{\Omega}{2\pi} + \frac{\delta\Omega}{2\pi}\sin(\omega_u T k) = f_o + \delta f \sin(2\pi f_u T k). \tag{6.41}$$

Thus the approximate frequency responses, N, with respect to ω_u can be defined as follows.

$$\begin{aligned} N(\Omega, \delta\Omega, j\omega_u) &= \frac{H_1(\Omega, \delta\Omega, j\omega_u)}{\delta\Omega}, \\ &= \frac{\omega_u}{\pi\delta\Omega}\int_0^{2\pi/\omega_u} p_{lp}(t)(\sin\omega_u t + j\cos\omega_u t)\,dt \end{aligned} \tag{6.42}$$

As alluded to earlier, the describing function method can be implemented for the approximate frequency response analysis, since the system response with the low-pass filter satisfies the low-pass filter hypothesis that is the fundamental assumption of the describing method. However, the analytical derivation such as the harmonic balance equations in (6.29)$\sim$(6.29) are hardly possible for computing H_1. Instead, the numerical computation using the definition of the describing function in (6.20) is implemented. See the MATLAB® source code in Appendix D. Repeating this procedure for different Ω, the set of the approximate frequency responses can be obtained. Therefore, G_p in Fig. 83 can be defined as

$$G_p = \{N(\Omega, \delta\Omega, j\omega_u) | 2\pi f_{\min} \leqslant \Omega \leqslant 2\pi f_{\max}, \delta\Omega \ll \Omega\}.$$

The controller design can be performed based upon this quantification of the output response. In effect, this approach performs an approximate linearization of the plant dynamics about each input frequency. If the linearization is valid, there will exist a domain of attraction for stability and regulation for each of the designed controllers. If linearization points are employed sufficiently, one can be confident that the overall control system will be stable and will regulate the pressure to the desired value for recovery.

Using the small disturbance $\delta f = 5.662 \times 10^{-4}$ (10 Hz), f_o is varied discretely by 0.0255 (450 Hz), 0.0311 (550 Hz), 0.0340 (600 Hz), 0.0368 (650 Hz), 0.0396 (700 Hz) within the operating range of $f_j = 0.0266 \sim 0.0455$ (400$\sim$750 Hz). The resultant set of G_p is shown in Fig. 85.

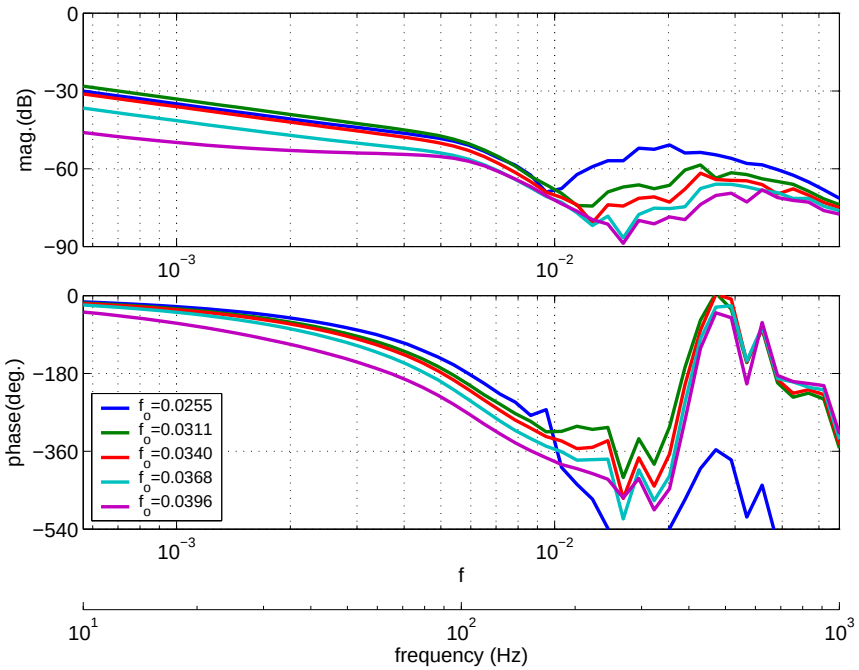

Fig. 85. A set of frequency responses of the linearized plant.

3. Design of PI Controller

Based upon the errors of the NARMAX model compared with the CFD results, the phase margin should be greater than 60 degree and the gain margin should be greater than 20 dB in order to satisfy the robust stability of the feedback loop.

A PI controller $G_c(z)$ is proposed for the system as shown in Fig. 86. The controller is turned on at $t = 0$.

The control results with the proportional gain (K_P) 3.2 and integral gain (K_I) 0.08 are presented in Fig. 87. The response p_{lp} converges successfully to the reference pressure $p_{ref} = 0.0084$. Initially, the jet frequency is saturated at the lower bound and it takes about $t = 200$ on a dimensionless time scale for the integral efforts in the controller to compensate the feedback error. The jet frequency is operating at $f_j = 0.0356$ (629 Hz) in steady state. Figure 88 presents the frequency response of the loop transfer function, $G_p \cdot G_c$.

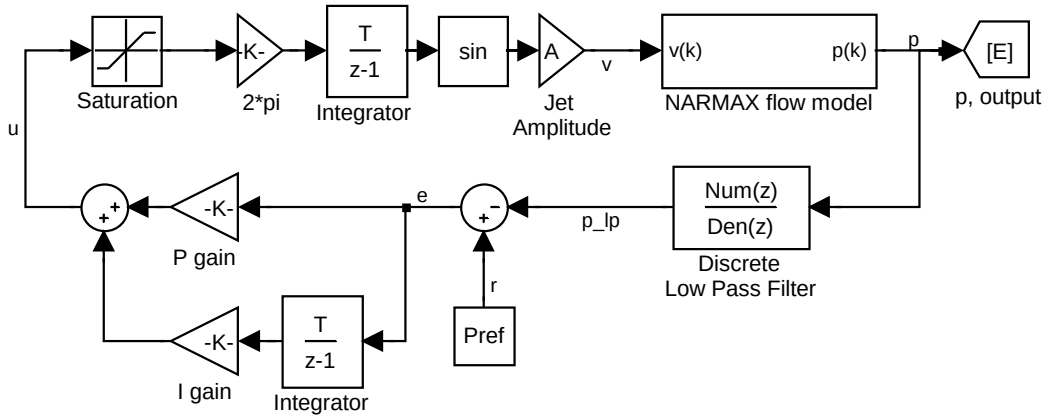

Fig. 86. Simulink® diagram for PI feedback control.

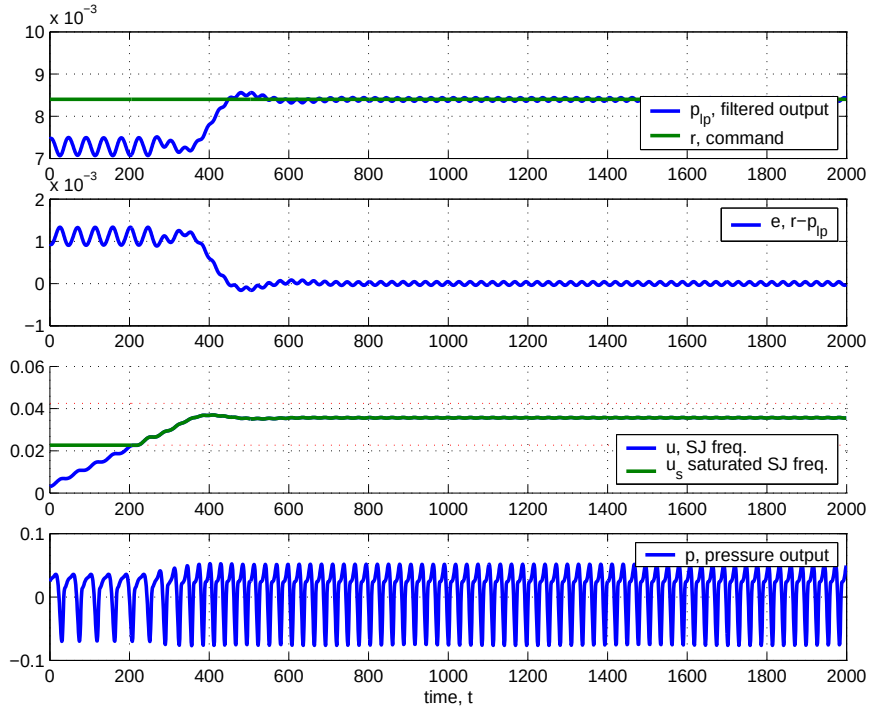

Fig. 87. Closed loop responses using the PI controller with a proportional gain 3.2 and integral gain 0.08.

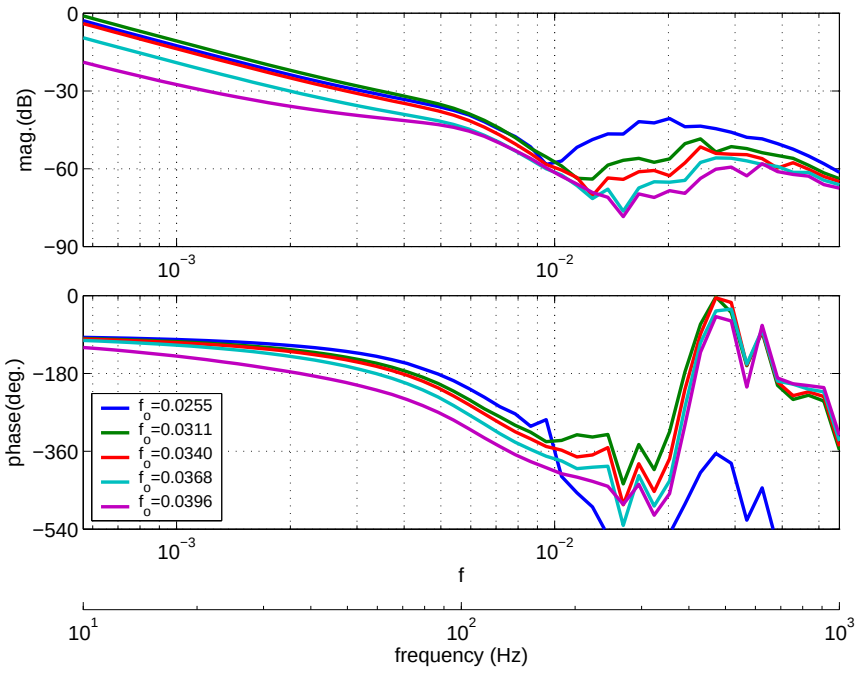

Fig. 88. Frequency responses of the loop transfer functions, $G_p \cdot G_c$.

The gain set of $K_P = 3.2, K_I = 0.08$ turns out to be a best choice for this control system. Figure 89 shows the time domain responses using only proportional gain. The proportional gain up to $K_P = 15$ is not enough to have the control output, u, overcome the lower bound of the jet frequency. As a result, the lower limit of the jet frequency is commanded continuously to the system and thus the steady state error is significant. In contrast, larger proportional gains than $K_P = 15$ have the controller output hit the upper and lower bounds repeatedly. This behavior is similar to a limit cycle oscillation caused by the saturation. Therefore, the saturation of the jet frequency, a crucial condition for the linear controller design in this research, limits the proportional gain so that it has a negative effect on the bandwidth of the controller.

With a relatively small proportional gain, adding an integral gain improves the control performance effectively as shown in Fig. 90. The integral gain eliminates the steady state error. Furthermore, the transient response improves as the integral gain increases. How-

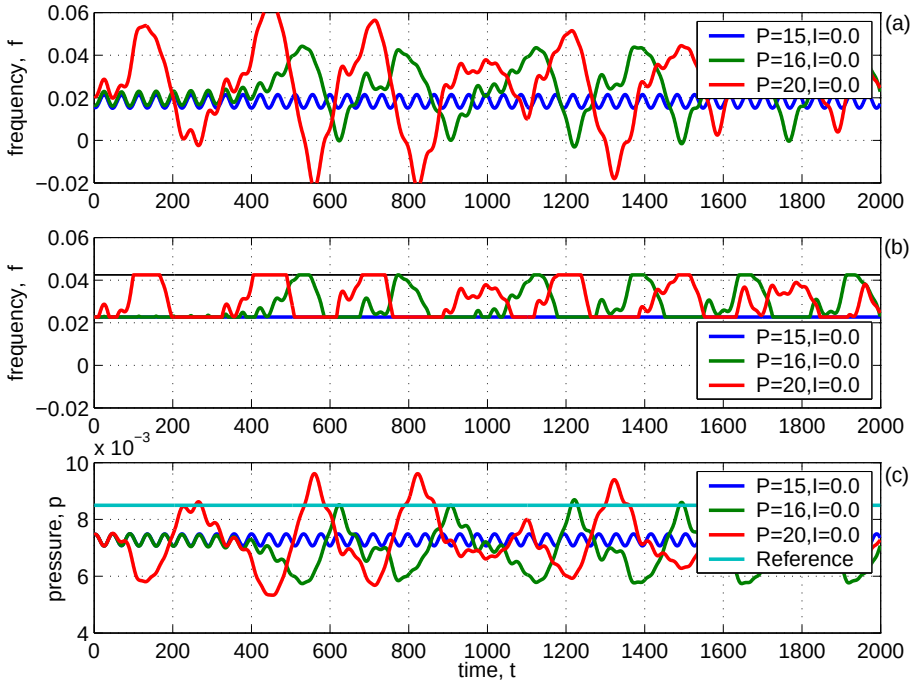

Fig. 89. Closed loop responses for a proportional controller with various gains. (a): u before passing saturation, (b): u after passing saturation and (c): p_{lp}.

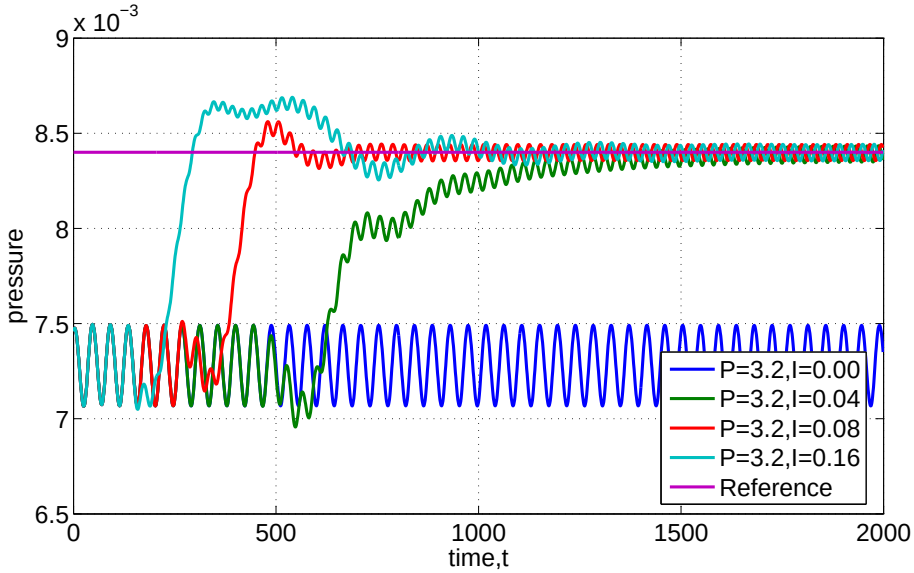

Fig. 90. Closed loop responses for a PI controller with a proportional gain 3.2 and various integral gains.

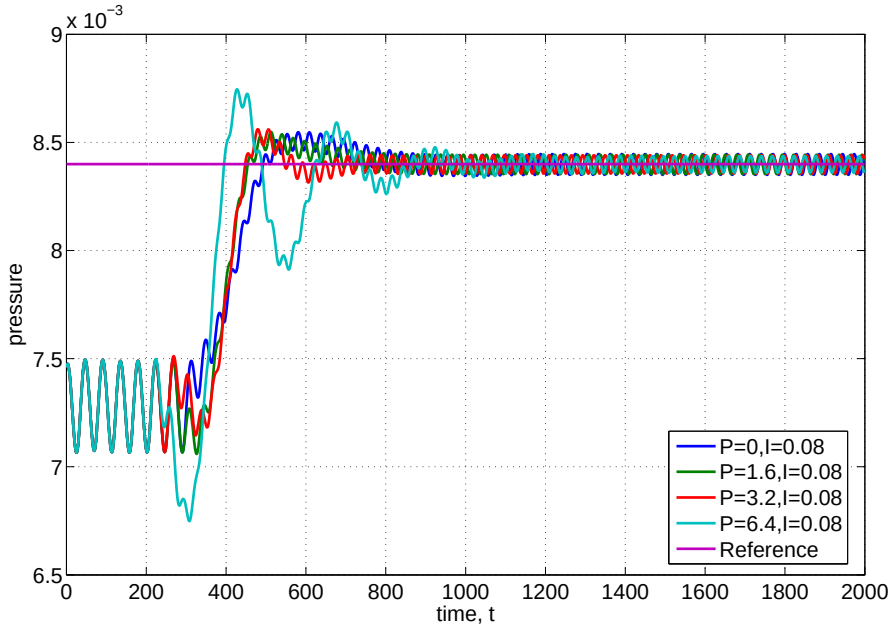

Fig. 91. Closed loop responses for a PI controller with various proportional gains and a integral gain 0.08.

ever, the oversized integral gain increases the overshoot of the system response. Figure 91 presents the effects of the proportional gain on the system response with a constant integral gain. The proportional gain with an adequate magnitude expedites the system performance considerably.

The designed controller is only effective for a constant free stream velocity. As shown in Fig 55, the variation of the free stream velocity shifts the characteristic curve between the jet frequency and mean pressure. Consequently, the model coefficients of the NARMAX equation will be dependent of the free stream as discussed in Chapter IV. Implementation of the lookup table for the reference pressure, which varies dependent of the free stream, is feasible to cope with the effects of the free stream. However, the essential condition for the validity of the lookup table implementation is that the rate of change of the free stream velocity should be sufficiently slower than the rate of change of control output and the synthetic jet frequency.

K. Outstanding Issues for Control Approach

The fluidic system with synthetic jet jets is a nonlinear parameter varying (NLPV) system. After low-pass filtering of the system output, it turns out that the system can be separated as a dominant quasi-linear parameter varying (LPV) system and small nonlinear disturbances originated from the filtered response of the original system. Assuming this is a favorable time scale difference, the LPV system can be robustly stabilized using linear control theory with the attenuated NLPV responses treated as bounded disturbances using the small gain theorem. There are three issues raised from this control problem: time scale and nonlinearity. They will determine the applicability of the linear control design approach currently employed to the general control problem for the pressure recovery when the free-stream conditions are changing, the actuator dynamics is slower and the pressure recovery is to be achieved faster.

1. Time Scale

The system has inherently four different time scales: variation of free stream velocity, rate of change of synthetic jet frequency, synthetic jet frequency and actuator dynamics. Currently, the actuator dynamics is neglected, assuming the actuator responds fast. Regarding the free stream, it is considered to change slowly compared with the other factors. To obtain the quasi-linear output for u, there should exist the considerable difference between f_u and f_j. In this research, the frequency bands are determined as follows.

1. Rate of change of free stream velocity: ≈ 0 Hz
2. Rate of change of synthetic jet frequency, f_u: < 100 Hz
3. Synthetic jet frequency, f_j: > 400 Hz
4. Actuator dynamics: $\approx \infty$ Hz

All of these time scales are important in the design. However, the relationship between f_u and f_j in particular will affect the stability and performance of the whole system. The specification of a low pass filter is directly related to both of f_u and f_j. The filter pass frequency affects f_u and the filter stop frequency corresponds to the lower bound of f_j. If the upper bound of f_u increases and approaches the lower bound of f_j, the control performance will be improved but the assumptions about the quasi-linear responses may not hold any more. As shown in Fig. 89, the saturation of f_j has a negative effect on the bandwidth of the controller. Lowering the stop frequency below 400 Hz, i.e. decreasing the lower bound of f_j, will help improving the control performance while it will cost the low-pass filter the stricter filter specification.

In addition, the rate of change of free stream should be carefully examined. Even though its rate assumed to be relatively slow, it will affect the stability of the model and entire control system whatsoever.

2. Validation of a Linear Controller

According to the control objective, the controller produces the jet frequency command around the peak of the maximum pressure. As shown in Fig. 84, there exist multiple frequency points for the single value of pressure. Furthermore, although the characteristic curve is fairly linear considering left and right sides of the maximum pressure peak respectively, the overall characteristics are clearly nonlinear. This issue should be carefully treated with for the controller design.

Furthermore, interestingly, the plant gain ranges from some value $k > 0$ to 0 and approaches zero as the target pressure for the controller approaches the maximum pressure. Hence, maximum pressure recovery is not theoretically possible in finite time, i.e. only asymptotically. Furthermore, the system will respond faster, due to the high plant gain, when the synthetic jet frequency is farthermost from the optimal value.

CHAPTER VII

CONCLUSIONS AND FUTURE WORK

In conclusion, this research was dedicated to develop a feedback control approach for flow separation control using synthetic jets. The achievements in the aspect of experiments and simulations are stated as follows.

The Wind tunnel experiments using the synthetic jet actuator showed that synthetic jet actuation can be a good tool for flow separation control and the jet frequency is a key parameter for control. The maximum lift coefficient improves monotonically as the jet actuation frequency increases. It implies that synthetic jets have the potential to control the degree of flow separation beyond delaying the separation. Furthermore, the dynamic pitching experiments showed synthetic jets can control the dynamic stall as well. The limitation of synthetic jets is it has little effect on aerodynamic coefficients at low angles of attack where the flow is attached even without the jet actuation. Synthetic jets are effective only for the condition of flow separation.

From the CFD simulation on a flat plate, the key concepts for synthetic jet simulation and modeling were verified. The approximate velocity profiles were developed for the inlet boundary condition to guarantee the establishment of the Blasius boundary layer in the absence of actuation, because all the effects of synthetic jets stem from the interaction of the jets with the crossing shear layer. The oscillating velocity boundary condition to approximate the synthetic jet actuator was validated based upon the simulation in the quiescent flow, where the assumed jet model creates a series of vortices that advance to an external flow. Subsequently, the NARMAX model was developed to relate the synthetic jet velocity to a wall pressure fluctuation downstream from the jet slot. The simulation and identification were repeated for different free stream velocities. The results show that if the variation of the free stream velocities are within a small range, the effects of the free stream

can be represented by a set of model coefficients with an invariant regressor structure of the model. A set of model coefficients can be interpreted as uncertainties of the flow model, if the controller is to deal with the varying free stream velocity.

The simulation on a backward-facing step with rounded edges presented the relationship between synthetic jet frequency and flow separation. According to the range of a reduced jet frequency F^+, the vortices created by jet actuation show different behaviors. At the low frequency $F^+ \simeq 0.1$, the minor separation bubbles immediately follow the primary bubble. As the frequency increases, the minor bubbles disappear and a single separation bubble is created periodically and convected downstream. Previous research proposed that $0.5 \leq F^+ \leq 1.5$ would be the optimal range to achieve the maximum pressure recovery that is represented by the mean pressure. For this CFD configuration, the maximum pressure is recovered at $F^+ \simeq 0.8$. The narrow-frequency-band receptivity of the separating shear layer implies that the effective flow separation control could be accomplished by operating the synthetic jets around $F^+ \simeq 0.8$. Moreover, the variation of free stream velocity shifts the relationship between the mean pressure and the jet frequency. However, the characteristics of the relationship are consistent regardless of the free stream.

The feedback control system was synthesized based upon the simulation results for the rounded backward facing step in order to achieve the maximum pressure recovery by varying a synthetic jet frequency. The pressure acquisition point was chosen to be as close to the jet exit slot as possible to minimize the time delay between the jet excitation and the measured pressure, while the sensitivity of the pressure to the jet frequency was to be large enough to represent the effects of the jet frequency on the wall pressure distribution. The uniqueness of this control problem is due to the fact that an input variable is a frequency of the physical variable, i.e. jet velocity. In other words, the profile of the jet velocity is restricted as a sinusoid and the controller can vary only the jet frequency. It causes inherently the strong nonlinearity of the fluidic system that consists of the actuator model

and the NARMAX flow equation.

Low-pass filtering, which was introduced to acquire the pressure recovery instead of averaging, of the pressure response facilitates quasi-linear approximation of the system in the frequency domain. The describing function method was applied for this frequency domain analysis. The filter specification to satisfy the low-pass filter hypothesis, which is a fundamental assumption of the describing function, is that the filter stop frequency is to be lower than or equal to a lower bound of the synthetic jet frequency. The frequency components of the pressure beyond the filter stop frequency should be attenuated to the sufficiently small magnitude compared with the magnitude of the frequency components below the filter pass frequency. The low-pass filter separates the frequency response of the overall system into two frequency bands. The low frequency band below the filter pass frequency includes a quasi-linear response targeted by the feedback controller and the high frequency band over the filter stop frequency contains the attenuated higher harmonic components, which can be treated as internal disturbances.

Based upon low-pass filtering, a PI feedback controller was designed. To ensure the one-to-one correspondence of the jet frequency and the filtered pressure response, the upper bound of the jet frequency was set at the optimal frequency Ω_{max} at which the maximum pressure is recovered. As a result, the jet frequency is bounded. The lower bound of the jet frequency was already set at the filter stop frequency. Using the PI controller with a P gain 3.2 and an I gain 0.8, the system response followed the desired pressure command successfully and the transient system response was improved.

In this research, several assumptions were made to simplify the problem. As for future work, the issues related to those assumptions should be considered to improve the performance of the feedback controller as follows:

- Several assumptions for CFD simulation can be altered for the better. The laminar

flow was assumed for the CFD simulation. As regards to the free stream velocity, the turbulent boundary layer condition would be closer to the real-world condition. Furthermore, the jet magnitude can be considered a function of jet frequency as shown in (6.3).

- From the standpoint of feedback control design, the NARMAX model captures the key characteristics of a fluidic system with synthetic jet actuation, i.e. frequency modulation-demodulation behavior, qualitatively. However, its accuracy for the input frequency band needs to be improved. The system identification including the actuator model and low-pass filter could upgrade the accuracy of the NARMAX model.

- The jet frequency was assumed to have both lower and upper bounds as shown in the characteristic curve of Fig 84. The low frequency bound is necessary to guarantee the frequency band separation. The upper frequency bound was set at the frequency Ω_{max} to ensure the existence of a single jet frequency corresponding to the given pressure. Consequently, the current controller covers only the left slope of the curve. In order to cover the nonlinear region of the curve including the pressure peak, the gain scheduling is worth investigating. localized controllers can be designed for left (positive gradient) and right (negative gradient) sides of the curve respectively. A supervisory controller can schedule the controller according to the sign of pressure gradient [69].

- A controller using a lookup table for the desired pressure was proposed to consider the variation of free stream velocity, but was not implemented. This method would be valid only if the rate of change of free stream velocity is much slower than the rate of change of other variables [68]. If the rate of change of free stream is comparable to other variables, the lookup table scheme may not be valid any more. The nonlinear fluid model should be revised to incorporate the free stream velocity directly into

the model structure and the combination of adaptive and robust controller could be considered to deal with both continuous variations and “jump” in plant uncertainty [70].

- The feedback controller was verified under the NARMAX simulation. The research is needed to extend the verification to the direct CFD simulation. The controller routine can be inserted between the velocity boundary condition and the pressure data capture routine. It helps improve the confidence of the currently proposed control scheme.

REFERENCES

[1] R. M. Wood, “Aerodynamic drag and drag reduction,” *AIAA Paper*, no. 2003-209, pp. 1–20, 2003.

[2] O. M. Aamo and M. Krstic, *Flow control by feedback: stabilization and mixing*. New York: Springer-Verlag, 2003.

[3] M. GadelHak, “The fluid mechanics of microdevices- the Freeman Scholar Lecture,” *Journal of Fluids Engineering*, vol. 121, pp. 5–33, Mar 1999.

[4] ——, “Flow control: the future,” *Journal of Aircraft*, vol. 38, no. 3, pp. 402–418, 2001.

[5] R. Rathnasingham and K. S. Breuer, “Coupled fluid-structural characteristics of actuator for flow control,” *AIAA Journal*, vol. 35, no. 5, pp. 832–837, 1997.

[6] A. Glezer and M. Amitay, “Synthetic jets,” *Annual Review of Fluid Mechanics*, vol. 34, pp. 503–529, 2002.

[7] B. Smith and A. Glezer, “The formation and evolution of synthetic jets,” *Physics of Fluids*, vol. 10, no. 9, pp. 2281–2297, Sep 1998.

[8] M. Amitay and A. Glezer, “Role of actuation frequency in controlled flow reattachment over a stalled airfoil,” *AIAA Journal*, vol. 40, pp. 209–216, 2002.

[9] J. Gilarranz, L. Traub, and O. Rediniotis, “Characterization of a compact, high-power synthetic jet actuator for flow separation control,” *AIAA Paper*, no. 2002-0127, pp. 1–28, 2002.

[10] M. Amitay, D. Smith, V. Kibens, D. Parekh, and A. Glezer, "Aerodynamic flow control over an unconventional airfoil using synthetic jet actuators," *AIAA Journal*, vol. 39, pp. 361–370, 2001.

[11] M. Amitay, A. Honohan, M. Trautman, and A. Glezer, "Modification of the aerodynamic characteristics of bluff bodies using fluidic actuators," *AIAA Paper*, no. 97-2004, pp. 1–15, 1997.

[12] J. Donovan, L. Kral, and A. Cary, "Active flow control applied to an airfoil," *AIAA Paper*, no. 98-0210, pp. 1–17, 1998.

[13] L. Kral, J. Donovan, A. Cain, and A. Cary, "Numerical simulation of synthetic jet actuators," *AIAA Paper*, no. 97-1824, pp. 1–13, 1997.

[14] C. Lee and D. Goldstein, "Two-dimensional synthetic jet simulation," *AIAA Journal*, vol. 40, no. 3, pp. 510–516, 2002.

[15] R. Mittal, P. Rampunggoon, and H. Udaykumar, "Interaction of a synthetic jet with a flat plate boundary layer," *AIAA Paper*, no. 2001-2773, pp. 1–11, 2001.

[16] M. Amitay, M. Horvath, M. Michaux, and A. Glezer, "Virtual aerodynamic shape modification at low angles of attack using synthetic jet actuators," *AIAA Paper*, no. 2001-2975, pp. 1–11, 2001.

[17] R. Mittal and P. Rampunggoon, "On the virtual aeroshaping effect of synthetic jets," *Physics of Fluids*, vol. 14, no. 4, pp. 1533–1536, 2002.

[18] D. Guo, A. W. Cary, and R. K. Agarwal, "Numerical simulation of vectoring of a primary jet with a synthetic jet," *AIAA Journal*, vol. 41, no. 12, pp. 2364–2370, Dec 2003.

[19] B. Smith and A. Glezer, "Jet vectoring using synthetic jets," *Journal of Fluid Mechanics*, vol. 458, pp. 1–34, 2002.

[20] Y. Chen, S. Liang, K. Aung, A. Glezer, and J. Jagoda, "Enhanced mixing in a simulated combustor using synthetic jet actuators," *AIAA Paper*, no. 99-0449, pp. 1–12, 1999.

[21] R. Mahalingam, N. Rumigny, and A. Glezer, "Thermal management using synthetic jet ejectors," *IEEE Transactions on Components and Packaging Technologies*, vol. 27, no. 3, pp. pp.439–444, 2004.

[22] B. D. Ritchie and J. M. Seitzmanl, "Controlled fuel-air mixing using a synthetic jet array," *AIAA Paper*, no. 2000-3465, pp. 1–8, 2000.

[23] H. Wang and S. Menon, "Fuel-air mixing enhancement by synthetic microjets," *AIAA Journal*, vol. 39, no. 12, pp. 2308–2319, Dec 2001.

[24] A. Glezer, M. Amitay, and A. M. Honohan, "Aspects of low-and high-frequency aerodynamic flow control," *AIAA Paper*, no. 2003-0533, pp. 1–20, 2003.

[25] D. Greenblatt and I. Wygnaski, "Dynamic stall control by periodic excitation, part 1: NACA 0015 parametric study," *Journal of Aircraft*, vol. 38, no. 3, pp. 430–438, 2001.

[26] D. Greenblatt, B. Nishiri, A. Darabi, and I. Wygnaski, "Dynamic stall control by periodic excitation, part 2: Mechanisms," *Journal of Aircraft*, vol. 38, no. 3, pp. 439–447, 2001.

[27] Y. He, A. W. Cary, and D. A. Peters, "Parametric and dynamic modelling for synthetic jet control of a post-stall airfoil," *AIAA Paper*, no. 2001-0733, pp. 1–11, 2001.

[28] P. Lorber, D. McCormick, T. Anderson, M. Pollack, T. Corke, and K. Breuer, "Rotorcraft retreating blade stall control," *AIAA Paper*, no. 2000-2475, pp. 1–16, 2000.

[29] L. G. Pack and A. Seifert, “Dynamics of active separation control at high Reynolds number,” *AIAA Paper*, no. 2000-0409, pp. 1–14, 2000.

[30] A. Seifert and L. Pack, “Active control of separated flows on generic configurations at high Reynolds numbers,” *AIAA Paper*, no. 99–3403, pp. 1–19, 1999.

[31] J. Choi, W. pung Jeon, and H. Choi, “Control of flow around an airfoil using piezo-ceramic actuators,” *Transactions of Korean Society of Mechanical Engineers (B)*, vol. 24, no. 8, pp. 1112–1118, 2000.

[32] L. Traub, A. Miller, U. Ukpai, O. Rediniotis, K. Kim, and G. Jeong, “Reconfigurable synthetic jet actuation and closed-loop flow control,” *AIAA Paper*, no. 2003-217, pp. 1–45, Jan 2003.

[33] L. Traub, A. Miller, O. Rediniotis, K. Kim, G. Jeong, and S. Jayasuriya, “Effects of synthetic jets on large-amplitude sinusoidal pitch motions,” *Journal of Aircraft*, vol. 42, no. 1, pp. 282–285, 2005.

[34] K. Kim, G. Jeong, S. Jayasuriya, L. W. Traub, A. Miller, and O. Rediniotis, “Design of a control and data acquisition system for synthetic jet experiments,” in *3rd IFAC Symposium on Mechatronic Systems*, I. R. Petersen, Ed., Manly Beach, Sydney, Australia, Sep 2004, pp. 621–626.

[35] A. Seifert and L. Pack, “Oscillatory control of separation at high Reynolds numbers,” *AIAA Journal*, vol. 37, no. 9, pp. 1062–1071, 1999.

[36] B. Allan, J. Juang, D. Raney, A. Seifert, L. Pack, and D. Brown, “Closed-loop separation control using oscillatory flow excitation,” NASA Langley Research Center, Tech. Rep. NASA/CR-2000-210324, Aug 2000.

[37] P. Moin and T. Bewley, "Feedback control of turbulence," *Appl Mech Rev*, vol. 47, no. 6, pp. S3–S13, 1994.

[38] D. Lockerby and P. Carpenter, "Numerical simulation of the interaction of microactuators and boundary layers," *AIAA Journal*, vol. 40, no. 1, pp. 67–73, 2002.

[39] Q. Gallas, R. Holman, T. Nishida, B. Carroll, M. Shelpak, and L. Cattafesta, "Lumped element modeling of piezoelectric-driven synthetic jet actuators," *AIAA Journal*, vol. 41, no. 2, pp. 240–247, Feb 2003.

[40] U. I. Ukpai and O. Rediniotis, "Dynamic modeling of a synthetic jet actuator for hingeless flow control," in *Proceedings of the American Control Conference*, Jun 2003, pp. 1704–1709.

[41] J. Magill, M. Bachmann, G. Rixon, and K. McManus, "Dynamic stall control using a model-based observer," *Journal of Aircraft*, vol. 40, pp. 355–362, 2003.

[42] C. Rowley, D. Williams, T. Colonius, R. Murray, D. MacMartin, and D. Fabris, "Model-based control of cavity oscillations, part II: System identification and analysis," *AIAA Paper*, no. 2002–0972, pp. 1–11, 2002.

[43] E. Caraballo and M. Samimy, "Low dimensional modeling of flow for closed-loop flow control," *AIAA-Paper*, no. 2003-59, 2003.

[44] K. Kunisch and S. Volkwein, "Galerkin proper othogonal decomposition methods for a general equation in fluid dynamics," *SIAM J. Numer. Anal.*, vol. 40, no. 2, pp. 492–515, 2002.

[45] O. K. Rediniotis, J. Ko, and A. J. Kurdila, "Reduced order nonlinear Navier-Stokes models for synthetic jets," *Journal of Fluids Engineering*, vol. 124, pp. 433–443, Jun 2002.

[46] X. Yuan, E. Caraballo, H. Ozbay, A.Serrani, J. DeBonis, J. Myatt, and M. Samimy, "Reduced-order model-based feedback controller design for subsonic cavity flows," *AIAA Paper*, no. 2005–293, 2005.

[47] J. W. Glass and M. A. Franchek, "NARMAX modelling and robust control of internal combustion engines," *International Journal of Control*, vol. 72, no. 4, pp. 289–304, 1999.

[48] J. Glass, "Frequency based nonlinear controller design for regulating systems subject to time domain constraints," Ph.D. dissertation, Purdue University, Lafayette, IN, Dec 2000.

[49] S. Chen and S. Billings, "Representation of non-linear systems: the NARMAX model," *International Journal of Control*, vol. 49, no. 3, pp. pp. 1013–1032, 1989.

[50] S. Chen, S. Billings, and W. Luo, "Orthogonal least squares methods and their application to non-linear system identification," *International Journal of Control*, vol. 50, no. 5, pp. 1873–1896, 1989.

[51] O. Boaghe, S. Bilings, L. Li, P. fleming, and J. Liu, "Time and frequency domain identification and analysis of a gas turbine engine," *Control Engineering Practice*, vol. 10, pp. 1347–1356, 2002.

[52] N. Chiras, C. Evans, and D. Rees, "Nonlinear gas turbine modeling using NARMAX structures," *IEEE Transactions on Instrumentation and Measurement*, vol. 50, no. 4, pp. 893–898, Aug 2001.

[53] L. Piroddi and W. Spinelli, "Long-range nonlinear prediction: a case study," in *42nd IEEE Conference on Decision and Control*, Dec 2003, pp. 3984–3989.

[54] M. Thompson, S. Schooling, and M. Soufian, "The practical application of a nonlinear identification methodology," *Control Engineering Practice*, vol. 4, no. 3, pp. 295–306, 1996.

[55] S. Billings and K. Tsang, "Spectral analysis for non-linear systems, part 1:parametric non-linear spectral analysis," *Mechanical Systems and Signal Processing*, vol. 3, no. 4, pp. 319–339, 1989.

[56] O. Nelles, *Nonlinear sytem identification:from classical approaches to neural networks and fuzzy models*. New York: Springer-Verlag, 2001.

[57] J. Sjoberg, Q. Zhang, L. Ljung, A. Benveniste, B. Delyon, P. yves Glorennec, H. Hjalmarsson, and A. Juditsky, "Nonlinear black-box modeling in system identification: a unified overview," *Automatica*, vol. 31, no. 12, pp. 1691–1724, 1995.

[58] G. Karniadakis and S. Sherwin, *Spectral/hp element methods for computational fluid dynamics*, 2nd ed. New York; Oxford: Oxford University Press, Jun. 2005.

[59] S. J. Sherwin, "Triangular and tetrahedral spectral/h-p finite element methods for fluid dynamics," Ph.D. dissertation, Princeton University, Princeton, NJ, 1995.

[60] D. P. Rizzetta, M. R. Visbal, and M. J. Stanek, "Numerical investigation of synthetic-jet flowfields," *AIAA Journal*, vol. 37, no. 8, pp. 919–927, 1999.

[61] H. Schlichting and K. Gersten, *Boundary layer theory*, 8th ed. Berlin: Springer-Verlag, 2000.

[62] D. Smith, "Interaction of a synthetic jet with a crossflow boundary layer," *AIAA Journal*, vol. 40, no. 11, pp. 2277–2288, 2002.

[63] N. Schaeffler, "The interaction of a synthetic jet and a turbulent boundary layer," *AIAA Paper*, no. 2003-0643, pp. 1–16, 2003.

[64] L. Ljung, *System identification: theroy for the user*, 2nd ed. Upper Saddle River, NJ: Prentice Hall, 1999.

[65] S. McCabe, "Nonlinear digital system identification applied to vibrating structures," Ph.D. dissertation, Purdue University, Lafayette, IN, May 1998.

[66] J.-J. E. Slotine and W. Li, *Applied nonlinear control*. Englewood Cliffs, NJ: Prentice Hall, 1991.

[67] C. Schwartz and R. Gran, "Describing function analysis using MATLAB and Simulink," *IEEE Control Systems Magazine*, pp. 19–26, Aug. 2001.

[68] H. Khalil, *Nonlinear systems*, 3rd ed. Upper Saddle River, NJ: Prentice Hall, 2002.

[69] G. Goodwin, S. Graebe, and M. Salgado, *Control system design*. Upper Saddle River, NJ: Prentice Hall, 2001.

[70] P.-O. Gutman, "Robust and adaptive control: fidelity or an open relationship?" *System and Control Letters*, vol. 49, no. 3, pp. 9–19, 2003.

Supplemental Sources Consulted

- G. Addington, J. Hall, and J. Myatt, "Reduced order modelling applied to reactive flow control," *AIAA Paper*, no. 2002-4807, pp. 1–11, 2002.

- D. Atherton, *Nonlinear control engineering*. New York: Van Nostrand Reinhold, 1982.

- P. M. J. V. D. Hof and R. J. P. Schrama, "Identification and control–closed-loop issues," *Automatica*, vol. 31, no. 12, pp. 1751–1770, 1995.

- S. Kang and H. Choi, "Suboptimal feedback control of turbulent flow over a backward-facing step," *Journal of Fluid Mechanics*, vol. 463, pp. 201–227, 2002.

- J. Kim, "Control of turbulent boundary layers," *Physics of Fluids*, vol. 15, no. 5, pp. 1093–1105, 2003.

- K. Kim, A. Beskok, and S. Jayasuriya, "Nonlinear system identification for the interaction of synthetic jets with a boundary layer," in *2005 American Control Conference*, Jun 2005, pp. 1313–1318.

- L. Pack and A. Seifert, "Periodic excitation for jet vectoring and enhanced spreading," *AIAA Paper*, no. 99-0672, pp. 1–18, 1999.

- P. Rao, T. Strganac, and O. Rediniotis, "Control of aeroelastic response via synthetic jet actuators," *AIAA Paper*, no. 2000-25714, pp. 1–8, 2000.

- M. Schoberi, "The influence of curvature and pressure gradient on the flow and velocity distribution," *International Journal of Mechanical Sciences*, vol. 32, no. 10, pp. 851–861, 1990.

- A. Seifert and L. G. Pack, "Separation control at flight Reynolds numbers: lessons learned and future directions," *AIAA Paper*, no. A00-33876, pp. 1–16, 2000.

- A. Seifert, V.Theofilis, and R.D.Joslin, "Issues in active flow control: theory, simulation and experiment," *AIAA Paper*, no. 2002-3277, pp. 2–41, 2002.

- S. Skogestad and I. Postlethwaite, *Multivariable Feedback Control*. New York: John Wiley & Sons, 1996.

- B. Smith and G. Swift, "A comparision between synthetic jets and continuous jets," *Experiments in Fluids*, vol. 34, pp. 467–472, 2003.

- N. K. Yamaleev and M. H. Carpenter, “A reduced-order model for efficient simulation of synthetic jet actuators,” NASA, Hampton, VA, Tech. Rep. NASA/TM-2003-212664, Dec 2003.

- O. Yaniv, *Quantitative feedback design of linear and nonlinear control systems*. Boston: Kluwer Academic Publishers, 1999.

APPENDIX A

FIRST-ORDER HARMONIC BALANCE EQUATIONS FOR NARMAX

The input and truncated output for the NARMAX equation in (6.14) are assumed as follows.

$$v(k) = \frac{A}{2j}\left(e^{j\Omega Tk} - e^{-j\Omega Tk}\right), \tag{A.1}$$

$$\tilde{p}(k) = A_{DC}(A, j\Omega) + \frac{1}{2j}H_1(A, j\Omega)\, e^{j\Omega Tk} - \frac{1}{2j}H_1(A, -j\Omega)\, e^{-j\Omega Tk}. \tag{A.2}$$

Before developing the first-order harmonic balance equations, it is needed to formulate the relationships between the regressors and the input/output terms.

Linear input terms, $v(k-n_{10,i})$, in (6.14) are expressed as

$$\begin{aligned}
\hat{p}_{10,i}(k) &= c_{10,i}\, v(k-n_{10,i}), \\
&= c_{10,i}\left[\frac{A}{2j}\left(e^{j\Omega T\left(k-n_{10,i}\right)} - e^{-j\Omega T\left(k-n_{10,i}\right)}\right)\right], \\
&= C1_{10,i}e^{j\Omega Tk} + C1^{*}_{10,i}e^{-j\Omega Tk},
\end{aligned} \tag{A.3}$$

where $C1_{10,i} = c_{10,i}\frac{A}{2j}e^{-j\Omega Tn_{10,i}}$. The superscript * stands for the conjugate term.

Linear output terms, $p(k-n_{01,i})$, in (6.14) are expressed as

$$\begin{aligned}
\hat{p}_{01,i}(k) &= c_{01,i}\, p(k-n_{01,i}), \\
&= c_{01,i}\begin{bmatrix} A_{DC}(A, j\Omega) + \frac{1}{2j}H_1(A, j\Omega)\, e^{j\Omega T\left(k-n_{01,i}\right)} \\ -\frac{1}{2j}H_1(A, -j\Omega)\, e^{-j\Omega T\left(k-n_{01,i}\right)} \end{bmatrix}, \\
&= DC_{01,i}A_{DC}(A, j\Omega) + C1_{01,i}H_1(A, j\Omega)\, e^{j\Omega Tk} + C1^{*}_{01,i}H_1(A, -j\Omega)\, e^{-j\Omega Tk},
\end{aligned} \tag{A.4}$$

where $DC_{01,i} = c_{01,i}$, $C1_{01,i} = \frac{c_{01,i}}{2j}e^{-j\Omega Tn_{01,i}}$.

Quadratic input terms, $v(k-n_{20,i_1})v(k-n_{20,i_2})$, in (6.14) are expressed as

$$\begin{aligned}\hat{p}_{20,i}(k) &= c_{20,i}v(k-n_{20,i_1})\,v(k-n_{20,i_2}),\\ &= c_{20,i}\left[\frac{A}{2j}\left(e^{j\Omega T\left(k-n_{10,i_1}\right)}-e^{-j\Omega T\left(k-n_{10,i_1}\right)}\right)\right]\\ &\quad\times\left[\frac{A}{2j}\left(e^{j\Omega T\left(k-n_{10,i_2}\right)}-e^{-j\Omega T\left(k-n_{10,i_2}\right)}\right)\right],\\ &= DC_{20,i}+DC^{*}_{20,i}+C2_{20,i}e^{j\Omega T2k}+C2^{*}_{20,i}e^{-j\Omega T2k},\end{aligned} \tag{A.5}$$

where $DC_{20,i}=c_{20,i}\frac{A^2}{4}e^{j\Omega T\left(n_{20,i_1}-n_{20,i_2}\right)}$, $C2_{20,i}=-c_{20,i}\frac{A^2}{4}e^{-j\Omega T\left(n_{20,i_1}+n_{20,i_2}\right)}$.

Quadratic output terms, $\hat{p}(k-n_{02,i_1})\hat{p}(k-n_{02,i_2})$, in (6.14) are expressed as

$$\begin{aligned}\hat{p}_{02,i}(k) =& c_{02,i}\hat{p}\,(k-n_{02,i_1})\,\hat{p}\,(k-n_{02,i_2}),\\ =& c_{02,i}\begin{bmatrix} A_{DC}(A,j\Omega)+\frac{1}{2j}H_1(A,j\Omega)\,e^{j\Omega T\left(k-n_{01,i_1}\right)}\\ -\frac{1}{2j}H_1(A,-j\Omega)\,e^{-j\Omega T\left(k-n_{01,i_1}\right)}\end{bmatrix}\\ &\times\begin{bmatrix} A_{DC}(A,j\Omega)+\frac{1}{2j}H_1(A,j\Omega)\,e^{j\Omega T\left(k-n_{01,i_2}\right)}\\ -\frac{1}{2j}H_1(A,-j\Omega)\,e^{-j\Omega T\left(k-n_{01,i_2}\right)}\end{bmatrix},\\ =& DC1_{02,i}A^2_{DC}(A,j\Omega)+DC2_{02,i}H_1(A,j\Omega)\,H_1(A,-j\Omega)\\ &+C1_{02,i}H_1(A,j\Omega)\,A_{DC}(A,j\Omega)\,e^{j\Omega Tk}\\ &+C1^{*}_{02,i}H_1(A,-j\Omega)\,A_{DC}(A,j\Omega)\,e^{-j\Omega Tk}\\ &+C2_{02,i}H^2_1(A,j\Omega)\,e^{j\Omega T2k}+C2^{*}_{02,i}H^2_1(A,-j\Omega)\,e^{-j\Omega T2k},\end{aligned} \tag{A.6}$$

where the coefficients are

$$\begin{aligned}DC1_{02,i} &= c_{02,i},\\ DC2_{02,i} &= \frac{c_{02,i}}{4}\left(e^{-j\Omega T\left(n_{02,i_1}-n_{02,i_2}\right)}+e^{j\Omega T\left(n_{02,i_1}-n_{02,i_2}\right)}\right),\\ C1_{02,i} &= \frac{c_{02,i}}{2j}\left(e^{-j\Omega Tn_{02,i_1}}+e^{-j\Omega Tn_{02,i_2}}\right),\\ C2_{02,i} &= -\frac{c_{02,i}}{4}e^{-j\Omega T\left(n_{02,i_1}+n_{02,i_2}\right)}.\end{aligned}$$

Crossed terms, $v(k-n_{11,i_1})\hat{p}(k-n_1 1,i_2)$, in (6.14) are expressed as

$$\begin{aligned}
\hat{p}_{11,i}(k) =& c_{11,i} v(k-n_{11,i_1})\,\hat{p}(k-n_{11,i_2}),\\
=& c_{11,i}\left[\frac{A}{2j}\left(e^{j\Omega T\left(k-n_{10,i_1}\right)}-e^{-j\Omega T\left(k-n_{10,i_1}\right)}\right)\right]\\
&\times\left[\begin{array}{l} A_{DC}(A,j\Omega)+\frac{1}{2j}H_1(A,j\Omega)\,e^{j\Omega T\left(k-n_{01,i_2}\right)}\\ -\frac{1}{2j}H_1(A,-j\Omega)\,e^{-j\Omega T\left(k-n_{01,i_2}\right)}\end{array}\right],\\
=& DC_{11,i}H_1(A,j\Omega)+DC^*_{11,i}H_1(A,-j\Omega)\\
&+C1_{11,i}A_{DC}(A,j\Omega)\,e^{j\Omega Tk}+C1^*_{11,i}A_{DC}(A,j\Omega)\,e^{-j\Omega Tk}\\
&+C2_{11,i}H_1(A,j\Omega)\,e^{j\Omega T2k}+C2^*_{11,i}H_1(A,-j\Omega)\,e^{-j\Omega T2k},
\end{aligned} \tag{A.7}$$

where the coefficients are

$$\begin{aligned}
DC_{11,i} &= c_{11,i}\frac{A}{4}e^{j\Omega T\left(n_{11,i_1}-n_{11,i_2}\right)},\\
C1_{11,i_1} &= c_{11,i}\frac{A}{2j}e^{-j\Omega T n_{11,i_1}},\\
C2_{11,i} &= -c_{11,i}\frac{A}{4}e^{-j\Omega T\left(n_{11,i_1}+n_{11,i_2}\right)}.
\end{aligned}$$

Introducing (A.2) and (A.3)$\sim$(A.7) into (6.14), the NARMAX equation is rewritten as

$$\begin{aligned}
&A_{DC}(A,j\Omega)+\frac{1}{2j}H_1(A,j\Omega)\,e^{j\Omega kT}-\frac{1}{2j}H_1(A,-j\Omega)\,e^{-j\Omega kT}=\\
&\sum_{i=1}^{m_{10}}\hat{p}_{10,i}(k)+\sum_{i=1}^{m_{01}}\hat{p}_{01,i}(k)+\sum_{i=1}^{m_{20}}\hat{p}_{20,i}(k)+\sum_{i=1}^{m_{02}}\hat{p}_{02,i}(k)+\sum_{i=1}^{m_{11}}\hat{p}_{11,i}(k).
\end{aligned} \tag{A.8}$$

Comparing the left and right side of (A.8), the coefficients of the DC and first harmonic terms should be "balanced" respectively. Therefore, the first-order harmonic balance equa-

tions are constructed as

$$\begin{aligned} A_{DC}(A,j\Omega) = &\left[\sum_{i=1}^{m_{01}} DC_{01,i}\right] A_{DC}(A,j\Omega) + \sum_{i=1}^{m_{20}} \left[DC_{20,i} + DC_{20,i}^{*}\right] \\ &+ \left[\sum_{i=1}^{m_{02}} DC1_{02,i}\right] A_{DC}^{2}(A,j\Omega) + \left[\sum_{i=1}^{m_{02}} DC2_{02,i}\right] H_1(A,j\Omega) H_1(A,-j\Omega) \\ &+ \left[\sum_{i=1}^{m_{11}} DC_{11,i}\right] H_1(A,j\Omega) + \left[\sum_{i=1}^{m_{11}} DC_{11,i}^{*}\right] H_1(A,-j\Omega), \end{aligned} \tag{A.9}$$

$$\begin{aligned} \frac{1}{2j} H_1(A,j\Omega) = &\sum_{i=1}^{m_{10}} C1_{10,i} + \left[\sum_{i=1}^{m_{01}} C1_{01,i}\right] H_1(A,j\Omega) \\ &+ \left[\sum_{i=1}^{m_{02}} C1_{02,i}\right] H_1(A,j\Omega) A_{DC}(A,j\Omega) + \left[\sum_{i=1}^{m_{11}} C1_{11,i}\right] A_{DC}(A,j\Omega). \end{aligned} \tag{A.10}$$

Defining $X = A_{DC}(A,j\Omega)$,$Y + jZ = H_1(A,j\Omega)$ and $[X,Y,Z] \in R$, the equations in (A.9) and (A.10) are reformulated in real domain as

$$C_3X^2 + (C_1 - 1)X + C_4Y^2 + 2C_5Y + C_4Z^2 - 2C_6Z + C_2 = 0, \tag{A.11}$$

$$(C_{11}X + C_9)Y - \left(C_{12}X + C_{10} + \frac{1}{2}\right)Z + C_{13}X + C_7 = 0, \tag{A.12}$$

$$\left(C_{12}X + C_{10} + \frac{1}{2}\right)Y + (C_{11}X + C_9)Z + C_{14}X + C_8 = 0, \tag{A.13}$$

where the real coefficients C's are defined as

$$C_1 = \sum_{i=1}^{m_{01}} DC_{01,i}, \qquad C_2 = \sum_{i=1}^{m_{20}} \left[DC_{20,i} + DC_{20,i}^{*}\right], \qquad C_3 = \sum_{i=1}^{m_{02}} DC1_{02,i},$$

$$C_4 = \sum_{i=1}^{m_{02}} DC2_{02,i}, \qquad C_5 + jC_6 = \sum_{i=1}^{m_{11}} DC_{11,i}, \qquad C_7 + jC_8 = \sum_{i=1}^{m_{10}} C1_{10,i},$$

$$C_9 + jC_{10} = \sum_{i=1}^{m_{01}} C1_{01,i}, \qquad C_{11} + jC_{12} = \sum_{i=1}^{m_{02}} C1_{02,i}, \qquad C_{13} + jC_{14} = \sum_{i=1}^{m_{11}} C1_{11,i}.$$

APPENDIX B

SECOND-ORDER HARMONIC BALANCE EQUATIONS FOR NARMAX

Suppose that the second harmonic term is considered in the truncated output as follows.

$$\begin{aligned}\hat{p}(t) &= A_{DC}(A, j\Omega) + F_1 \sin(\Omega t + \phi_1) + F_2 \sin(2\Omega t + \phi_2) \\ &= A_{DC}(A, j\Omega) + F_1 \cdot \frac{e^{j\phi_1} e^{j\Omega t} - e^{-j\phi_1} e^{-j\Omega t}}{2j} + F_2 \cdot \frac{e^{j\phi_2} e^{j2\Omega t} - e^{-j\phi_2} e^{-j2\Omega t}}{2j} \\ &= A_{DC}(A, j\Omega) + \frac{1}{2j} H_1(A, j\Omega) e^{j\Omega t} - \frac{1}{2j} H_1(A, -j\Omega) e^{-j\Omega t} \\ &+ \frac{1}{2j} H_2(A, j2\Omega) e^{j2\Omega t} - \frac{1}{2j} H_2(A, -j2\Omega) e^{-j2\Omega t},\end{aligned} \tag{B.1}$$

where $H_1(A, j\Omega) = F_1 \cdot e^{j\phi_1}$, $H_1(A, j\Omega) = F_1 \cdot e^{j\phi_1}$.

Applying the same procedure in Appendix A, the coefficients of each regressor are computed. The coefficients for the input linear terms are

$$C1_{10,i} = c_{10,i} \frac{A}{2j} e^{-j\Omega T n_{10,i}}.$$

The coefficients for the output linear terms are

$$DC_{01,i} = c_{01,i},\ C1_{01,i} = \frac{c_{01,i}}{2j} e^{-j\Omega T n_{01,i}},\ C2_{01,i} = \frac{c_{01,i}}{2j} e^{-j2\Omega T n_{01,i}}.$$

The coefficients for the quadratic input terms are

$$DC_{20,i} = c_{20,i} \frac{A^2}{4} e^{j\Omega T\left(n_{20,i_1} - n_{20,i_2}\right)},\ C2_{20,i} = -c_{20,i} \frac{A^2}{4} e^{-j\Omega T\left(n_{20,i_1} + n_{20,i_2}\right)}.$$

The coefficients for the quadratic output terms are

$$
\begin{aligned}
DC1_{02,i} &= c_{02,i}, \\
DC2_{02,i} &= \frac{c_{02,i}}{4}\left(e^{-j\Omega T\left(n_{02,i_1}-n_{02,i_2}\right)}+e^{j\Omega T\left(n_{02,i_1}-n_{02,i_2}\right)}\right), \\
DC3_{02,i} &= \frac{c_{02,i}}{4}e^{-j\Omega T\left(2n_{02,i_1}-2n_{02,i_2}\right)}, \\
C11_{02,i} &= \frac{c_{02,i}}{2j}\left(e^{-j\Omega T n_{02,i_1}}+e^{-j\Omega T n_{02,i_2}}\right), \\
C12_{02,i} &= \frac{c_{02,i}}{4}\left(e^{-j\Omega T\left(-n_{02,i_1}+2n_{02,i_2}\right)}+e^{-j\Omega T\left(2n_{02,i_1}-n_{02,i_2}\right)}\right), \\
C21_{02,i} &= -\frac{c_{02,i}}{4}e^{-j\Omega T\left(n_{02,i_1}+n_{02,i_2}\right)}, \\
C22_{02,i} &= \frac{c_{02,i}}{2j}\left(e^{-j2\Omega T n_{02,i_1}}+e^{-j2\Omega T n_{02,i_2}}\right).
\end{aligned}
$$

The coefficients for the crossed terms are

$$
\begin{aligned}
DC_{11,i} &= c_{11,i}\frac{A}{4}e^{j\Omega T\left(n_{11,i_1}-n_{11,i_2}\right)}, \\
C11_{11,i_1} &= c_{11,i}\frac{A}{2j}e^{-j\Omega T n_{11,i_1}}, \\
C12_{11,i_1} &= c_{11,i}\frac{A}{4}e^{-j\Omega T\left(-n_{11,i_1}+2n_{11,i_2}\right)}, \\
C2_{11,i} &= -c_{11,i}\frac{A}{4}e^{-j\Omega T\left(n_{11,i_1}+n_{11,i_2}\right)}.
\end{aligned}
$$

Finally, the second-order harmonic balance equations in real domain are formulated as

$$
C_3X^2+(C_1-1)X+C_4Y^2+2C_5Y+C_4Z^2-2C_6Z+C_2+C_{15}S^2+C_{15}T^2=0, \tag{B.2}
$$

$$
\begin{aligned}
&(C_{11}X+C_9)Y-\left(C_{12}X+C_{10}+\frac{1}{2}\right)Z+C_{13}X+C_7+C_{18}S-C_{19}T \\
&+C_{16}(YS+ZT)-C_{17}(YT-SZ)=0,
\end{aligned} \tag{B.3}
$$

$$
\begin{aligned}
&\left(C_{12}X+C_{10}+\frac{1}{2}\right)Y+(C_{11}X+C_9)Z+C_{14}X+C_8+C_{19}S+C_{18}T \\
&+C_{17}(YS+ZT)+C_{16}(YT-SZ)=0,
\end{aligned} \tag{B.4}
$$

$$-\frac{1}{2}T + C_{20}S - C_{21}T + C_{22} + C_{24}\left(Y^2 - Z^2\right) - 2C_{25}YZ + C_{26}XS$$
$$-C_{27}XT + C_{28}Y - C_{29}Z = 0, \tag{B.5}$$

$$\frac{1}{2}S + C_{20}T + C_{21}S + C_{23} + C_{25}\left(Y^2 - Z^2\right) + 2C_{24}YZ$$
$$+C_{27}XS + C_{26}XT + C_{29}Y + C_{28}Z = 0, \tag{B.6}$$

where $X = A_{DC}(A, j\Omega)$, $Y + jZ = H_1(A, j\Omega)$, $S + jT = H_2(A, j2\Omega)$ and $[X, Y, Z, S, T] \in R$. The real coefficients C's are defined as

$$C_1 = \sum_{i=1}^{m_{01}} DC_{01,i}, \qquad C_2 = \sum_{i=1}^{m_{20}} \left[DC_{20,i} + DC^*_{20,i}\right],$$
$$C_3 = \sum_{i=1}^{m_{02}} DC1_{02,i}, \qquad C_4 = \sum_{i=1}^{m_{02}} DC2_{02,i},$$
$$C_5 + jC_6 = \sum_{i=1}^{m_{11}} DC_{11,i}, \qquad C_7 + jC_8 = \sum_{i=1}^{m_{10}} C1_{10,i},$$
$$C_9 + jC_{10} = \sum_{i=1}^{m_{01}} C1_{01,i}, \qquad C_{11} + jC_{12} = \sum_{i=1}^{m_{02}} C1_{02,i},$$
$$C_{13} + jC_{14} = \sum_{i=1}^{m_{11}} C1_{11,i}, \qquad C_{15} = \sum_{i=1}^{m_{02}} \left(DC3_{02,i} + DC3^*_{02,i}\right),$$
$$C_{16} + jC_{17} = \sum_{i=1}^{m_{02}} C12_{02,i}, \qquad C_{18} + jC_{19} = \sum_{i=1}^{m_{11}} C12_{11,i},$$
$$C_{20} + jC_{21} = \sum_{i=1}^{m_{01}} C2_{01,i}, \qquad C_{22} + jC_{23} = \sum_{i=1}^{m_{20}} C2_{20,i},$$
$$C_{24} + jC_{25} = \sum_{i=1}^{m_{02}} C21_{02,i}, \qquad C_{26} + jC_{27} = \sum_{i=1}^{m_{02}} C22_{02,i},$$
$$C_{28} + jC_{29} = \sum_{i=1}^{m_{11}} C2_{11,i}.$$

APPENDIX C

MATLAB® CODES FOR THE NARMAX SYSTEM IDENTIFICATION

preprocess2 Preprocessing function to prepare the regression matrix

NARX_mgs2 Main function to calculate the NARMAX coefficients

postprocess2 Postprocessing function to express the identification results by a string that can be used by MATLAB

getcoeff Function to cluster the regressors and corresponding coefficients.

simulateNARX Funtion to simulate the identified NARMAX model

Example Code executing the NARMAX identification

```
load chirphis;                          %load input-output data
Pst=0.003949;

% coordinate
ANG=1.4924174129;
R=[cos(pi/2-ANG) -sin(pi/2-ANG);
    sin(pi/2-ANG) cos(pi/2-ANG)];
VEL=(R*[u(:,3)';v(:,3)'])';

skip=10;
i=skip:skip:length(t);                  % time step - delt=1.0
u=[0;VEL(i,2)];                         % input
yy=[0;p(i,7)-Pst];                      % measured output
t=[0;t(i)];                             % sampled time step

% prepare the configuration of the identification
SIDParam.ymaxlag=2;                     % max. lag for y
SIDParam.umaxlag=5;                     % max. lag for y
SIDParam.delay=9;                       % input delay
SIDParam.yinitial=yy(1:14);             % initial value for y
SIDParam.nlorder=2;                     % order of nonlinearity
SIDParam.constant=0;                    % disregard(0) or regard(1)
                                        % of contant term
SIDParam.errmargin=0.00025;             % eRR margin
```

```
% execute the identification
[Y,Po, label]=preprocess2(u,yy,SIDParam);
[regressors, eRR, P, theta]=NARX_mgs2(Po,label,Y,SIDParam);
[f,terms]=postprocess2(regressors,theta,SIDParam);

% save the results into file
save SID regressors theta SIDParam;

% ye : NARMAX simulation
ye=simulateNARX(u,regressors,theta,SIDParam);

% yp : one-step ahead estimation
yp=P*theta;
yp=[SIDParam.yinitial;yp];

% calculate NMSE(Normalized Mean Square Error)
err1=sqrt(((yy-ye)'*(yy-ye))...
     /((yy-mean(yy))'*(yy-mean(yy))))*100;
err2=sqrt(((yy-yp)'*(yy-yp))...
     /((yy-mean(yy))'*(yy-mean(yy))))*100;

% diplay results
disp(' ');
disp(sprintf('NARX system identification for p at x=%f y=%f : '...
                                                    ,x(7,:)));
disp(sprintf('the max. number of the regressors: %d',...
                                                  size(label,1)));
disp(sprintf('the number of the selected regressors: %d',...
                                                  length(eRR)));
disp(sprintf('error margin: %f',SIDParam.errmargin));
disp(sprintf('max. lag of u: %d',SIDParam.umaxlag));
disp(sprintf('time delay   : %d',SIDParam.delay));
disp(sprintf('max. lag of y: %d',SIDParam.ymaxlag));
disp(sprintf('NMSE(%%): %f (NARMAX sim.) %f (NARMAX est.)',...
                                                  err1,err2));
disp(' ');
disp('       term              parameter       eRR');
for i=1:length(eRR)
disp(sprintf('(%2d)  %15s %11.5f %12.3e', ...
                          i, terms(i,:),theta(i),eRR(i)));
end
```

NARX_mgs2

```
function [terms,eRR,Ps,theta]=NARX_mgs2(P,label,Y,SIDParam)
% [terms, eRR, P, theta]=NARX(P,label,y,errmr)
%                          errmr : error margin for err
%                          theta : coefficients of P
%                          y     : output
%%%%%%%%%%%%%%%%%%%%%%%%%%%%%%%%%%%%%%%%%%%%%%%%%%%%%%%%%%%%%%%%%%%%%%%%%%%%%%%%
% problem P*(TH)=Y
% with : A*(TH)=G, P=WA
% such that P*inv(A)*A*(TH)=Y
%           W*G=Y
```

```
ERRMARGIN=SIDParam.errmargin;
% check if a constant term is considered
if SIDParam.constant == 0   %the constant term excluded
    [ro,col]=size(label);
    P(:,ro)=[];
    label=label(1:ro-1,1:col-1);
end

%preparation
[N,M]=size(P);
A=speye(M);

%%%%%% compute W, A and G %%%%%%%%%%
%initialize
Ps=P;
W=P;
Z=Y;
Yprod=Y'*Y;

for k=1:M

    %search for the maximum value
    eRR_max=0.;
    j=k;
    for i=k:M
        g_cand=(W(:,i)'*Z)/(W(:,i)'*W(:,i));
        eRR_cand(i)=g_cand^2*(W(:,i)'*W(:,i))/Yprod;
        if eRR_cand(i)>=eRR_max
            j=i;
            eRR_max=eRR_cand(i);
        end
    end
    eRR(k)=eRR_max;

    %search done

    %swapping
    W(:,[k j])=W(:,[j k]);
    Ps(:,[k j])=Ps(:,[j k]);
    label([k j],:)=label([j k],:);
    if(k>=2)
        A(1:(k-1),[k j])=A(1:(k-1),[j k]);
    end
    %done

    % the kth stage
    Wk=W(:,k);
    mag2=Wk'*Wk;
    G(k)=(Wk'*Z)/mag2;

    %% update the vectors(Z,A,W) for the next step
    Z=Z-G(k).*Wk;
    for i=k+1:M
        A(k,i)=(Wk'*W(:,i))/mag2;
        W(:,i)=W(:,i)-A(k,i).*Wk;
    end
```

```
    if 1-sum(eRR)<=ERRMARGIN
        Ms=k;
        break;
    else %1-sum(eRR)>ERRMARGIN
        if k==M
        Ms=M;
        disp('Warning: the estimation does not satisfy ...
        the eRR margin criterion');
        end
    end
end

%back substitution
%A*(TH)=G
theta=zeros(Ms,1);
theta(Ms)=G(Ms);
for k=Ms-1:-1:1
    theta(k)=G(k)-A(k,k+1:Ms)*theta(k+1:Ms);
end

Ps=Ps(:,1:Ms);
terms=label(1:Ms,:);

%%% clustering
if SIDParam.nlorder==2
[c_10, n_10, dumm,   ind_10]=getcoeff(1,0,terms, ...
SIDParam, theta); %linear input term
[c_01, n_01, dumm,   ind_01]=getcoeff(0,1,terms, ...
SIDParam, theta); %linear output term
[c_20, n1_20, n2_20, ind_20]=getcoeff(2,0,terms, ...
SIDParam, theta); %quadratic input term
[c_02, n1_02, n2_02, ind_02]=getcoeff(0,2,terms, ...
SIDParam, theta); %quadratic output term
[c_11, n1_11, n2_11, ind_11]=getcoeff(1,1,terms, ...
SIDParam, theta); %cross input-output term
ind=[ind_10 ind_01 ind_20 ind_02 ind_11];
terms=terms(ind,:);
theta=theta(ind);
Ps=Ps(:, ind);
eRR=eRR(ind);
end
```

preprocess2

```
function [Y, P, label]=preprocess2(u,y, SIDparam)
%%%%%%%%%%%%%%%%%%%%%%%%%%%%%%%%%%%%%%%%%%%%%%%%%%%%%%%%%%%%%%%%%%%%%%%%%%%%
% columns of label
% y(k-1) y(k-2)...y(k-Ny) u(k-(1+Nd)) u(k-(2+Nd))...
% u(k-(Nu+Nd)) const.
%
% *if const == 1, the constant term is inlcuded into
%  the model.
% if D=max([Nu+Nd Ny])
% y(D+1)|y(D+1-1)...y(D+1-Ny) u(D+1-(1+Nd))...u(D+1-(Nu+Nd))
% ......|...
```

```
% y(N)   |y(N-1)   ... y(N-Ny)     u(N-(1+Nd))   ... u(N-(Nu+Nd))
%%%%%%%%%%%%%%%%%%%%%%%%%%%%%%%%%%%%%%%%%%%%%%%%%%%%%%%%%%%%%%%%%%%%%%%%%%%%%%%

Nu=SIDparam.umaxlag;
Ny=SIDparam.ymaxlag;
ord=SIDparam.nlorder;
opt=SIDparam.constant;
Nd=SIDparam.delay;

N=length(u);
if N ~= length(y)
    return;
end
D=max([Nu+Nd Ny]);

Y=y(D+1:N);

yu1=zeros(N-D,Ny);
yu2=zeros(N-D,Nu);
for i=1:Ny
    yu1(:,i)=y(D+1-i:N-i);
end
for i=1:Nu
    yu2(:,i)=u(D+1-(i+Nd):N-(i+Nd));
end
cyu=[yu1 yu2];

P=[];
label=[];
for k=1:ord
    ch=multichoose(Nu+Ny,k);
    [mch,nch]=size(ch);
    for i=1:mch
        tmpP=ones(N-D,1);
        for j=1:nch
            if ch(i,j) == 1
                tmpP=tmpP.*cyu(:,j);
            elseif ch(i,j) > 1
                tmpP=tmpP.*cyu(:,j).^ch(i,j);
            else
                %skip
            end
        end
        P=[P tmpP];
    end
    label=[label;ch];
end

%the lase column is reserved for the constant term
if opt==1               % the element for the constant is 1
    [mlabel,nlabel]=size(label);
    label=[label zeros(mlabel,1);
        zeros(1,nlabel) 1];
    P=[P ones(N-D,1)];
                % the last column for the constant is 1
else %opt==0            % the element for the constant is 0
```

```
    [mlabel,nlabel]=size(label);
    label=[label zeros(mlabel,1);
           zeros(1,nlabel) 0];
    P=[P zeros(N-D,1)];
              % the last column for the constant is 0
end

function mch=multichoose(nodes, jobs)
ch = nchoosek(1:(nodes+jobs-1),nodes-1);
rows = size(ch,1);
mch_tmp = [zeros(rows,1), ch, (nodes+jobs)*ones(rows,1)];
% mch = (diff(mch_tmp')-1)'; % diff operates on rows
% or
mch = diff(mch_tmp,1,2) - 1;
```

postprocess2

```
function [f,termsstr]=postprocess2(terms, theta, SIDParam)
% [f,termsstr]=postprocess2(terms,theta,SIDParam);
%  f: assemble the regressors to make the string
%  termsstr: string for the regressor
%  terms: matrix expression for the regressor, y first
%         and u follows.
%  theta: NARMAX coefficients
%  SIDParam: system information

Nu=SIDParam.umaxlag;
Ny=SIDParam.ymaxlag;
Nd=SIDParam.delay;
Cflag=SIDParam.constant;

%%%%%%%%%%%%%%%%%%%%%%%%%%%%%%%%%%%%%%%%%%%%%%%%
[ro,col]=size(terms);
k=1;
for i=1:Ny
    basiclabel(k,:)       =sprintf('y(k-%2d)',i);
    k=k+1;
end
for i=1+Nd:Nu+Nd
    basiclabel(k,:)    =sprintf('u(k-%2d)',i);
    k=k+1;
end
if Cflag==1
    basiclabel(k,:)=sprintf('_const_',i);
end
%%%%%%%%%%%%%%%%%%%%%%%%%%%%%%%%%%%%%%%%%%%%%%%%

%swap the terms to make the string for u advance.
terms(:,1:Ny+Nu)=terms(:,[Ny+1:Ny+Nu 1:Ny]);
basiclabel(1:Ny+Nu,:)=basiclabel([Ny+1:Ny+Nu 1:Ny],:);

termsstr=[];
f='y(k)=...';
for i=1:ro
    tmpterm=[];
```

```
    for j=1:col
        if terms(i,j) ~=0
            if terms(i,j)==1
                tmpterm=[tmpterm basiclabel(j,:) '*'];
            else
                tmpterm=[tmpterm basiclabel(j,:) ...
                        sprintf('^%d',terms(i,j)) '*'];
            end
        end
    end
    tmpterm(length(tmpterm))=[];
    termsstr=char(termsstr,tmpterm);
    f=char(f,sprintf('+(%.17e)*%s ...',theta(i),tmpterm));
end
termsstr(1,:)=[];
f=char(f(1:ro,:), strrep(f(ro+1,:),'...',';'));
[n,m]=size(f);
for i=1:n
    k=strfind(f(i,:),'*_const_');
    if ~isempty(k)
        f(i,:)=strrep(f(i,:),'*_const_','         ');
    end
end
```

getcoeff

```
function [c, n1, n2, ind]=getcoeff(ui,yj,reg, SIDInfo, theta)
% [c, n1, n2, ind]=getcoeff(ui,yj,reg, SIDInfo, theta)
% group the regressor terms and corresponding coefficients
% according to the clustering property.
% In the case of the cross input-out terms , ni for u, n2 for y
% there exist five gorups.
% c u(k-n1) for ui=1, yj=0
% c y(k-n1) for ui=0, yj=1
% c u(k-n1)u(k-n2) for ui=2, yj=0
% c y(k-n1)y(k-n2) for ui=0, yj=2
% c u(k-n1)y(k-n2) for ui=1, yj=1

c=[];
n1=[];
n2=[];
ind=[];

if SIDInfo.nlorder ~=2
    disp('This routine runs only for the 2nd order nonlinearity');
    return;
end

k=1;
Nd=SIDInfo.delay;
Ny=SIDInfo.ymaxlag;
Nu=SIDInfo.umaxlag;

for i=1:length(theta)
    yterms=reg(i,1:Ny);
```

```
    uterms=reg(i,1+Ny:(Ny+Nu));
    if ui==sum(uterms) && yj==sum(yterms)
        u_nz=[];
        for j=1:length(uterms)
            if uterms(j) ==1
                u_nz=[u_nz j+Nd];
            elseif uterms(j) ==2
                u_nz=[u_nz j+Nd j+Nd];
            end
        end
        y_nz=[];
        for j=1:length(yterms)
            if yterms(j)==1
                y_nz=[y_nz j];
            elseif yterms(j)==2
                y_nz=[y_nz j j];
            end
        end
        len_u_nz=length(u_nz);
        len_y_nz=length(y_nz);

        ind(k)=i;
        c(k)=theta(i);
        if len_u_nz==2 && len_y_nz==0
            n1(k)=u_nz(1);
            n2(k)=u_nz(2);
        elseif len_u_nz==0 && len_y_nz==2
            n1(k)=y_nz(1);
            n2(k)=y_nz(2);
        elseif len_u_nz==1 && len_y_nz==0
            n1(k)=u_nz(1);
            n2=[];
        elseif len_u_nz==0 && len_y_nz==1
            n1(k)=y_nz(1);
            n2=[];
        elseif len_u_nz==1 && len_y_nz==1
            n1(k)=u_nz(1);
            n2(k)=y_nz(1);
        else
            disp('Error');
        end
        k=k+1;
    end
end

tempsrc=[n1' n2'];
[b idx]=sortrows(tempsrc);
c=c(idx);
n1=n1(idx);
if ~isempty(n2)
    n2=n2(idx);
end
ind=ind(idx);
```

simulateNARX

```
function ys=simulateNARX(u,regs, coeff, SIDParam)
Nu=SIDParam.umaxlag;
Nd=SIDParam.delay;
Ny=SIDParam.ymaxlag;
yini=SIDParam.yinitial;

N=length(u);
D=max([Nu+Nd Ny]);
[row,col]=size(regs);

%initialize
ys=zeros(N,1);
ys(1:D)=yini;

for k=D+1:N
    ys(k)=0;

    %%%%%%%%%%%%%%%%%%%%%%%%%%%
    % i : regressor term
    % j : construction of the regressor from y and u
    %%%%%%%%%%%%%%%%%%%%%%%%%%%
    for i=1:row
        tmpv=1.;
        for j=1:Ny
            if regs(i,j) ~= 0
                tmpv=tmpv*ys(k-j)^regs(i,j);
            end
        end
        for j=1+Nd:Nu+Nd
            if regs(i,j-Nd+Ny) ~= 0
                tmpv=tmpv*u(k-j)^regs(i,j-Nd+Ny);
            end
        end
        tmpv=tmpv*coeff(i);
        ys(k)=ys(k)+tmpv;
    end
    if abs(ys(k)) > 1e10;
        ys(k)=inf;
        return
    end
end
```

APPENDIX D

MATLAB® CODE FOR COMPUTING THE DESCRIBING FUNCTION

```
% compute the the describing function
pos=7;
skip=10;
delay=14;
Pst=0.003949;
Ts=1;
A=0.1;

N=20000;
t=(0:Ts:Ts*(N-1))';

f=logspace(0,3)';
H=zeros(length(f),1);
for ind=1:length(f)
    disp(sprintf('[%d]',ind));

    % run the simulation
    % desing the input u
    fc=cal_omega(f(ind))/2/pi;
    fo=cal_omega(410)/2/pi;
    df=cal_omega(10)/2/pi;
    u=fo+df.*sin(2.*pi.*fc.*t);

    % actuator+NARMAX+lowpass-filter
    th=zeros(N,1);
    for i=2:N
        th(i)=th(i-1)+2*pi*Ts*u(i-1);
    end
    v=0.1.*sin(th);
    y=srcfn(v,delay)+Pst;
        load lpfilter1;
    ylp= filter(Num,Den,y);

    % extract the 1st Fourier coefficients
    Tc=1/fc;
    ylpR=ylp.*sin(2.*pi.*fc.*t);
    ylpI=ylp.*cos(2.*pi.*fc.*t);

    % interpolation and integration
    Nc=ceil(Tc/Ts);
    K=zeros(Nc,1);
    for i=N:-1:N-Nc+1
        intR = fnint(csapi(t(i-Nc+1:i),ylpR(i-Nc+1:i)));
        valueR=fnval(intR,[t(i)-Tc t(i)])*[-1;1] ;
        intI = fnint(csapi(t(i-Nc+1:i),ylpI(i-Nc+1:i)));
        valueI=fnval(intI,[t(i)-Tc t(i)])*[-1;1] ;
       K(i)=(valueR+sqrt(-1)*valueI);
    end
```

```
    % averaging
    H(ind)=mean(K)*2/(Tc*dw);

    % compute the magnitude and phase
    Kmag(ind)=abs(H(ind));
    Kphase(ind)=phase(H(ind))*180/pi;
    disp(sprintf('fc:%f Kmag:%f Kphase:%f',...
                 fc,Kmag(ind),Kphase(ind)));
end

%save the results
ww=cal_omega(f);
save DFresult ww H;

%%%%%%%%%%%%%%%%%%%%%%%%%%%%%%%%%%%%%%%%%%%%%%%%%%%%%%%%%%%%%%%%%%%%%%%%%%%%
% NARMAX model used for the describing fuction analysis

function y=srcfn(u,delay)
y=zeros(length(u),1);
y(1:delay)=zeros(delay,1);
for k=delay+1:length(y)
y(k)=...
+(-4.8240485587e+000)*u(k-10) ...
+(1.8234265578e+001)*u(k-11) ...
+(-2.6483052726e+001)*u(k-12) ...
+(1.7734745353e+001)*u(k-13) ...
+(-4.7058541884e+000)*u(k-14) ...
+(1.4030277941e+000)*y(k- 1) ...
+(-5.3417184228e-001)*y(k- 2) ...
+(-8.4599794090e+001)*u(k-10)^2 ...
+(3.6172957795e+002)*u(k-10)*u(k-11) ...
+(-3.1845313962e+002)*u(k-10)*u(k-12) ...
+(1.9498384440e+002)*u(k-10)*u(k-13) ...
+(-3.2711290827e+001)*u(k-10)*u(k-14) ...
+(-2.1676920600e+002)*u(k-11)^2 ...
+(-6.9285371838e+001)*u(k-11)*u(k-14) ...
+(2.5991454786e+002)*u(k-12)^2 ...
+(-3.0928765991e+002)*u(k-13)^2 ...
+(3.0153712315e+002)*u(k-13)*u(k-14) ...
+(-8.7000642739e+001)*u(k-14)^2 ...
+(-8.2788359004e+000)*y(k- 1)^2 ...
+(8.8467105437e+000)*y(k- 1)*y(k- 2) ...
+(-9.1634472993e-001)*y(k- 2)^2 ...
+(2.0950636760e+002)*u(k-10)*y(k- 1) ...
+(-2.1778114224e+002)*u(k-10)*y(k- 2) ...
+(-9.0225086856e+002)*u(k-11)*y(k- 1) ...
+(9.3475351483e+002)*u(k-11)*y(k- 2) ...
+(1.4843876326e+003)*u(k-12)*y(k- 1) ...
+(-1.5454845120e+003)*u(k-12)*y(k- 2) ...
+(-1.1000521434e+003)*u(k-13)*y(k- 1) ...
+(1.1626552255e+003)*u(k-13)*y(k- 2) ...
+(3.1093594904e+002)*u(k-14)*y(k- 1) ...
+(-3.3681430139e+002)*u(k-14)*y(k- 2) ;
end
```

VITA

Name	Kihwan Kim
Address	Department of Mechanical Engineering, Texas A&M University, College Station, TX, 77843-3123
Email	hwan@tamu.edu
Education	B.S., Mechanical Design and Production Engineering Seoul National University, Seoul, Korea, 1993 M.S., Mechanical Design and Production Engineering Seoul National University, Seoul, Korea, 1995
Experince	Research Engineer, Samsung Heavy Ind., Korea, 1995-2000 Research Scientist, Korea Institute of Science & Technology, Korea, 2000-2001